

---

---

ALMA MATER STUDIORUM  
UNIVERSITÀ DEGLI STUDI DI BOLOGNA

---

---

DIPARTIMENTO DI FISICA E ASTRONOMIA  
Dottorato di Ricerca in Astronomia  
CICLO XXVIII

GRAVITATIONAL LENSING AS A TOOL  
ON GALACTIC AND COSMOLOGICAL SCALES

Dottorando  
NICOLAS TESSORE

Relatore  
Prof. LAURO MOSCARDINI

Correlatori  
Dott. ROBERT BENTON METCALF  
Dott. FABIO BELLAGAMBA

Coordinatore  
Prof. LAURO MOSCARDINI

Esame finale anno 2015

---

Settore Concorsuale: 02/C1 – Astronomia, Astrofisica, Fisica della Terra e dei Pianeti  
Settore Scientifico-Disciplinare: FIS/05 – Astronomia e Astrofisica

## Abstract

This work considers the reconstruction of strong gravitational lenses from their observed effects on the light distribution of background sources. After reviewing the formalism of gravitational lensing and the most common and relevant lens models, new analytical results on the elliptical power law lens are presented, including new expressions for the deflection, potential, shear and magnification, which naturally lead to a fast numerical scheme for practical calculation.

The main part of the thesis investigates lens reconstruction with extended sources by means of the forward reconstruction method, in which the lenses and sources are given by parametric models. The numerical realities of the problem make it necessary to find targeted optimisations for the forward method, in order to make it feasible for general applications to modern, high resolution images. The result of these optimisations is presented in the `LENSED` algorithm. Subsequently, a number of tests for general forward reconstruction methods are created to decouple the influence of sourced from lens reconstructions, in order to objectively demonstrate the constraining power of the reconstruction.

The final chapters on lens reconstruction contain two sample applications of the forward method. One is the analysis of images from a strong lensing survey. Such surveys today contain  $\sim 100$  strong lenses, and much larger sample sizes are expected in the future, making it necessary to quickly and reliably analyse catalogues of lenses with a fixed model. The second application deals with the opposite situation of a single observation that is to be confronted with different lens models, where the forward method allows for natural model-building. This is demonstrated using an example reconstruction of the “Cosmic Horseshoe”.

An appendix presents an independent work on the use of weak gravitational lensing to investigate theories of modified gravity which exhibit screening in the non-linear regime of structure formation.

# Table of contents

|  |            |
|--|------------|
| <b>Abstract</b> . . . . .                                | <b>i</b>   |
| <b>Table of contents</b> . . . . .                       | <b>ii</b>  |
| <b>List of figures</b> . . . . .                         | <b>v</b>   |
| <b>List of tables</b> . . . . .                          | <b>vi</b>  |
| <b>List of symbols</b> . . . . .                         | <b>vii</b> |
| <b>1 Introduction</b> . . . . .                          | <b>3</b>   |
| <b>2 Gravitational lensing</b> . . . . .                 | <b>6</b>   |
| 2.1 The deflection of light by matter . . . . .          | 6          |
| 2.2 The lens equation . . . . .                          | 7          |
| 2.3 Deflection potential and Poisson equation . . . . .  | 10         |
| 2.4 Convergence, shear and magnification . . . . .       | 11         |
| 2.5 Multiple images and strong lensing . . . . .         | 13         |
| <b>3 Lens models</b> . . . . .                           | <b>14</b>  |
| 3.1 The building blocks of lenses . . . . .              | 14         |
| 3.2 The point mass . . . . .                             | 14         |
| 3.3 Isothermal profiles . . . . .                        | 16         |
| 3.4 Navarro, Frenk and White profiles . . . . .          | 18         |
| 3.5 Mass sheets . . . . .                                | 19         |
| 3.6 External shear . . . . .                             | 19         |
| <b>4 The elliptical power law profile lens</b> . . . . . | <b>21</b>  |
| 4.1 Elliptical lenses . . . . .                          | 21         |
| 4.2 Lens properties . . . . .                            | 24         |
| 4.3 Special cases . . . . .                              | 27         |
| 4.4 Numerical evaluation . . . . .                       | 29         |

|           |   |            |
|-----------|---|------------|
| <b>5</b>  | <b>Forward lens reconstruction</b>  | <b>33</b>  |
| 5.1       | Reconstruction with extended images                                       | 33         |
| 5.2       | Definition of a model   | 35         |
| 5.3       | Source models   | 37         |
| 5.4       | Simulation of the lens system   | 40         |
| 5.5       | Model evaluation  | 42         |
| 5.6       | Parameter estimation  | 44         |
| 5.7       | Relation to the inverse method  | 45         |
| <b>6</b>  | <b>The LENSED algorithm</b>   | <b>47</b>  |
| 6.1       | Rationale of the implementation   | 47         |
| 6.2       | Numerical simulation  | 49         |
| 6.3       | Variance estimation   | 51         |
| 6.4       | Sampling the parameter space  | 52         |
| 6.5       | Parallel computation  | 53         |
| <b>7</b>  | <b>Testing the forward method</b>   | <b>56</b>  |
| 7.1       | Testing reconstructions with mock data                                    | 56         |
| 7.2       | The influence of lensed sources   | 58         |
| 7.3       | Reconstruction of lenses  | 59         |
| 7.4       | Reconstruction of lensed sources  | 63         |
| 7.5       | Choice of integration rule  | 66         |
| <b>8</b>  | <b>Application: Strong lensing surveys</b>                                | <b>68</b>  |
| 8.1       | Analysis of lens surveys  | 68         |
| 8.2       | Comparative reconstruction  | 68         |
| 8.3       | Reconstruction results  | 70         |
| <b>9</b>  | <b>Application: Flexible lens modelling</b>                               | <b>76</b>  |
| 9.1       | Modelling individual lenses   | 76         |
| 9.2       | Singular isothermal models  | 81         |
| 9.3       | Power law models  | 85         |
| 9.4       | Summary of the results  | 89         |
| <b>10</b> | <b>Conclusion</b>   | <b>92</b>  |
|           | <b>References</b>   | <b>95</b>  |
|           | <b>Appendix: Weak lensing and cosmology</b>                               | <b>104</b> |
| <b>A</b>  | <b>Weak lensing of large scale structure in the presence of screening</b> | <b>105</b> |
| A.1       | Introduction  | 105        |

|                             |            |
|-----------------------------|------------|
| <b>Table of contents</b>    | iv         |
| A.2 Theory . . . . .        | 106        |
| A.3 Simulations . . . . .   | 112        |
| A.4 Results . . . . .       | 117        |
| A.5 Discussion . . . . .    | 127        |
| <b>References</b> . . . . . | <b>129</b> |

## List of figures

|     |  |     |
|-----|--|-----|
| 2.1 | Geometry of a two-plane gravitational lens . . . . .                     | 8   |
| 4.1 | Potential and density of the elliptical power law profile lens . . . . . | 26  |
| 4.2 | Critical structure of the elliptical power law profile lens . . . . .    | 28  |
| 4.3 | Series coefficients of the elliptical power law profile lens . . . . .   | 30  |
| 5.1 | Strong lensing observations with resolved sources . . . . .              | 34  |
| 5.2 | Isophotes of elliptical source profiles . . . . .                        | 38  |
| 5.3 | Image creation with a subsampled PSF . . . . .                           | 42  |
| 7.1 | Sample mock observations for testing . . . . .                           | 57  |
| 7.2 | Distribution of sources in observation ensembles . . . . .               | 59  |
| 7.3 | Constraining power on lens parameters . . . . .                          | 61  |
| 7.4 | Constraining power on source parameters . . . . .                        | 65  |
| 7.5 | Comparison of integration rules . . . . .                                | 67  |
| 8.1 | Reconstructions of SLACS observations . . . . .                          | 73  |
| 8.2 | Lens parameter constraints for a SLACS lens . . . . .                    | 75  |
| 9.1 | The “Cosmic Horseshoe” CSWA 1 . . . . .                                  | 77  |
| 9.2 | HST observation of CSWA 1 in the F475W band . . . . .                    | 80  |
| 9.3 | Singular isothermal ellipsoid models of CSWA 1 . . . . .                 | 82  |
| 9.4 | Elliptical power law models of CSWA 1 . . . . .                          | 86  |
| 9.5 | Final reconstruction of CSWA 1 . . . . .                                 | 91  |
| A.1 | Convergence maps in $\Lambda$ CDM and modified gravity models . . . . .  | 115 |
| A.2 | Light cone construction from simulation snapshots . . . . .              | 116 |
| A.3 | Fractional difference in the matter power spectrum . . . . .             | 118 |
| A.4 | Dimensionless convergence power spectra . . . . .                        | 121 |
| A.5 | Relative contribution to the convergence power spectrum . . . . .        | 122 |
| A.6 | Convergence power spectrum for $\Lambda$ CDM . . . . .                   | 123 |
| A.7 | Fractional convergence power spectra . . . . .                           | 124 |

## List of tables

|     |  |     |
|-----|--|-----|
| 7.1 | Constraining power on lens parameters . . . . .      | 61  |
| 7.2 | Constraining power on source parameters . . . . .    | 65  |
| 8.1 | Estimated parameters for some SLACS lenses . . . . . | 72  |
| 9.1 | Existing reconstructions of CSWA 1 . . . . .         | 79  |
| 9.2 | New reconstructions of CSWA 1 . . . . .              | 90  |
| A.1 | Parameters of modified gravity models . . . . .      | 113 |

# List of symbols

## Lensing quantities

|                      |   |
|----------------------|---|
| $\alpha$             | scaled deflection angle                                 |
| $\gamma$             | shear   |
| $\kappa$             | dimensionless surface mass density, convergence         |
| $\lambda$            | physical deflection angle                               |
| $\mu$                | magnification   |
| $\Sigma$             | physical surface mass density                           |
| $\Sigma_{\text{cr}}$ | critical surface mass density                           |
| $\psi$               | deflection potential                                    |
| $D_L$                | angular diameter distance to lens plane                 |
| $D_S$                | angular diameter distance to source plane               |
| $D_{LS}$             | angular diameter distance between lens and source plane |
| $R_E$                | Einstein radius in physical coordinates                 |
| $r_E$                | Einstein radius in angular coordinates                  |

## Physical symbols

|        |                          |
|--------|--------------------------|
| $\rho$ | mass density             |
| $c$    | speed of light in vacuum |
| $G$    | gravitational constant   |

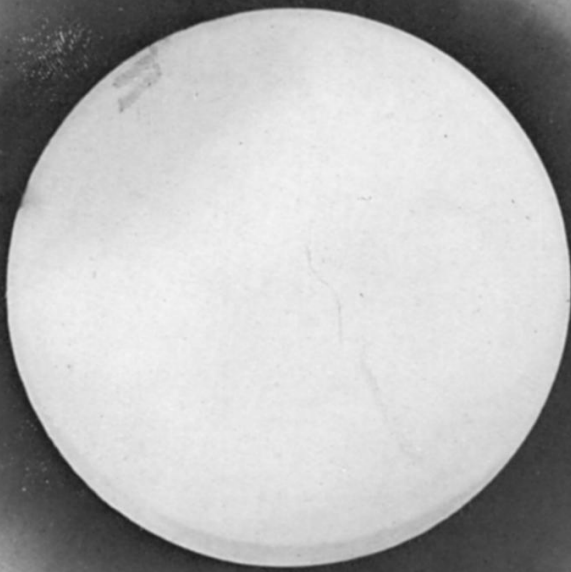
## Mathematical symbols

|                            |   |
|----------------------------|---|
| $\delta(x)$                | Dirac delta function  |
| $\arctan(x, y)$            | two-argument inverse tangent  |
| $\nabla f$                 | gradient operator $\nabla f = (\partial_x f, \partial_y f)$                     |
| $\nabla \cdot \mathbf{A}$  | divergence operator $\nabla \cdot \mathbf{A} = \partial_x A_x + \partial_y A_y$ |
| $\nabla \times \mathbf{A}$ | rotation operator $\nabla \times \mathbf{A} = \partial_x A_y - \partial_y A_x$  |
| $E[x]$                     | expectation value of $x$  |
| $\text{Var}[x]$            | variance of $x$   |
| $P(x)$                     | probability of $x$  |
| $P(x   y)$                 | conditional probability of $x$ given $y$  |
| $\mathbf{A}^T$             | transpose of matrix or vector   |

## Abbreviations

|            |                                    |
|------------|------------------------------------|
| CPU        | central processing unit            |
| EPL        | elliptical power law [profile]     |
| GPU        | graphics processing unit           |
| <i>HST</i> | Hubble Space Telescope             |
| <i>INT</i> | Isaac Newton Telescope             |
| NFW        | Navarro, Frenk and White [profile] |
| NSIE       | non-singular isothermal ellipsoid  |
| NSIS       | non-singular isothermal sphere     |
| PSF        | point-spread function              |
| SDSS       | Sloan Digital Sky Survey           |
| SLACS      | Sloan Lens ACS [survey]            |
| SIE        | singular isothermal ellipsoid      |
| SIS        | singular isothermal sphere         |

# Forward reconstruction of strong lensing observations



Eddington's seminal observation of the deflection of light rays by the sun during the May 29, 1919 solar eclipse. Faintly visible are markers indicating star positions. This picture shows the first successful test of the at the time newly proposed theory of general relativity, and the first use of gravitational lensing as an observational tool. From F. W. Dyson, A. S. Eddington and C. Davidson, *A Determination of the Deflection of Light by the Sun's Gravitational Field, from Observations Made at the Total Eclipse of May 29, 1919*, *Phil. Trans. R. Soc. Lond. Ser. A* 220 (1920) 291.

# 1 Introduction

The notion that gravity should act on light as well as matter is an old one, and goes as far back as Newton's *Opticks*. The Newtonian deflection of light rays passing close by or emanating from a massive body was calculated privately by Cavendish as early as 1784, and published by von Soldner in 1804 [115, 117]. It was Einstein himself who in 1915, upon completion of his theory of general relativity, realised that the Newtonian value of the deflection of a light ray near the sun is only half the value predicted by general relativity. When the twice-as-large deflection of light rays grazing the sun was indeed observed a short time afterwards by Eddington during the May 29, 1919 solar eclipse [31, 116], it was a spectacular verification of the newborn theory and made worldwide headlines. This observation was not only the first of many subsequent successful confirmations of general relativity, but at the same time the first observational use of the tool that would eventually become known as *gravitational lensing*.

A century later, gravitational lensing is a tried and true method of astronomy and astrophysics. The general subject of lensing theory and applications is today broadly categorised into three parts [87]. *Strong lensing* acts mainly on the scale of galaxies and galaxy clusters, and its distinctive feature is the non-linear deflection of the background distribution of light, leading to the signature multiple images, arcs and rings. *Weak lensing* is observed on cluster and cosmological scales. It is a small effect in the linear regime that subtly aligns background galaxies with intervening matter, and the distribution of the latter can be extracted statistically from the observed distribution of light. Finally, *microlensing* involves the dynamic variation of flux when compact objects pass in front of background sources on scales too small to be resolved.

The focus of this thesis is mainly strong gravitational lensing, specifically the reconstruction of lens systems from observations of galaxy-galaxy lensing events. The details of the matter distribution in these systems lead to implications for a wide range of fundamental topics such as dark matter-dark matter and dark matter-baryon interactions, the mass of the dark matter particle, constraints on possible modifications of the theory of gravity, as well as astrophysical questions such as how baryons segregate from dark matter and how the efficiency of star formation depends on the dark matter distribution. Furthermore, strong lenses now allow astronomers to detect some of the most distant objects ever observed

and study galaxy formation at the cosmic dawn.

In addition to the scientific challenges of finding and observing lenses, the reconstruction of strong lenses has increasingly become a numerical problem. While the targets of previous lensing observations were often point-like QSOs or galaxies with low resolution, there is an ever-growing availability of observations with resolved features. Such observations contain a large amount of information about the invisible distribution of matter within the lens, and may soon lead to the systematic direct detection of dark matter substructure in galaxies [111]. Future surveys such as the Dark Energy Survey (DES), Large Synoptic Survey Telescope (LSST), and Euclid are expected to increase the population of known strong lenses by  $\sim 1000$ ,  $\sim 100.000$  and  $\sim 150.000$ , respectively [28]. Investigating such enormous numbers of systems requires a dramatically changed approach to reconstructions, which today often involve manual modelling of the individual observations [11], a process that is already quickly becoming infeasible. Moreover, reconstruction methods currently in use require considerable computational efforts, especially when the detail in the observation is high. This is perhaps most evident in the abundance of reconstructions of low resolution data, but conspicuous absence of the same for publicly available, high resolution, space-based observations from the *Hubble Space Telescope (HST)*.

The outline of the thesis is as follows. Chapter 2 introduces the formalism of gravitational lensing that is used throughout the text. Chapter 3 presents the standard lens models that are used in the following work. Chapter 4 contains the detailed derivation of an elliptical lens model following a power law profile. Chapter 5 then develops the method of forward lens reconstruction from the ground up. Chapter 6 demonstrates the necessary techniques used in a fast and accurate implementation of the forward method, which is provided in the LENSED algorithm. In Chapter 7, this implementation and the forward method in general are rigorously tested and their usefulness for practical applications demonstrated. Finally, in Chapter 8 and Chapter 9, the LENSED algorithm is used in two real-world settings, first to reconstruct a set of observations from a lens survey with a common model, and secondly to analyse a single high resolution observation with competing lens models. The results of the thesis are summarised in Chapter 10, and a brief outlook on possible next steps is given.

In addition to the effort in the reconstruction of strong lenses, this thesis also contains in an appendix a small contribution to cosmological investigations with weak lensing. This cosmological probe has been embraced as a powerful test of gravitational physics on large scales. It supplies complementary information to probes of the matter density field through spectroscopic and photometric galaxy redshift surveys and, in principle, should be insensitive to galaxy bias. Current measurements of weak lensing on large scales are not yet competitive with other cosmological probes, but the future looks promising with upcoming surveys such as Euclid [85], LSST [45], WFIRST [97] and SKA [22].

As in the case of strong lensing, new computational solutions will be needed to extract the wealth of information contained in the eventually available data. The

specific problem demonstrated here is an investigation of *screening*, which is a common feature in a number of proposed theories of modified gravity [51]. These theories offer a possible approach to explaining the observational evidence for cosmic acceleration by introducing modifications to general relativity in regions of low density, low acceleration, or on large scales. A number of models have been proposed [26], and the idea that there may be a *gravitational* solution to the dark energy problem has led to a renewed scrutiny of the fundamental properties of gravity. This thesis describes the algorithms that can be used to produce lensed maps in cosmologies with screening and are the starting point for developing a concerted and comprehensive search for signatures of screening in observations of weak lensing.

## 2 Gravitational lensing

### 2.1 The deflection of light by matter

The formalism of gravitational lensing treats the propagation of light in the limit of geometrical optics, meaning that light rays travel in straight lines until they are eventually deflected by a gravitational lens. This is a simplification of the full framework of general relativity, in which light follows the curvature of spacetime on null geodesics of the metric. The approximation is valid where gravitation is weak enough to be linearised. Then it is possible to separate the equations into a smooth background metric, in the following always assumed to be a flat  $\Lambda$ CDM cosmology, and any number of perturbations which act as deflectors or lenses. The simplest such deflector is a point mass  $M$ ; its deflection is given by the classical deflection formula of general relativity,

$$\lambda = \frac{4GM}{c^2 R} \quad (2.1)$$

for a light ray passing at a distance  $R$ . Due to the linearity of the equations, this fundamental result is all that is necessary to calculate the deflection even for an arbitrary distribution of matter.

**Notation.** Two-dimensional vectors denoting positions or displacements on a flat sky are set in bold, e.g.  $\mathbf{x} = (x_1, x_2)$  and  $\Sigma(\mathbf{x}) = \Sigma(x_1, x_2)$ . Three-dimensional positional vectors have their third component along the line of sight explicitly appended, e.g.  $(\mathbf{x}, z) = (x_1, x_2, z)$  and  $\rho(\mathbf{x}, z) = \rho(x_1, x_2, z)$ . General matrices are set in upright letters,  $A = Q \Lambda Q^{-1}$ . Matrices acting on positional vectors are bold and upright,  $\mathbf{y} = \mathbf{A} \mathbf{x}$ . Lengths are written in upper case for physical coordinates, e.g.  $R = 10$  kpc, and in lower case for angular coordinates, e.g.  $r = 10$  arcsec.

**The deflection of light by a mass distribution.** Assuming that gravity is linear, the deflection of light rays due to an extended mass distribution  $\rho(\mathbf{X}, Z)$  can be partitioned into deflections from infinitesimal masses  $dM = \rho(\mathbf{X}, Z) dV$  located at the three-dimensional positions  $(\mathbf{X}, Z) = (X_1, X_2, Z)$ . When a ray travelling parallel to the  $Z$ -axis at  $(\mathbf{X}, Z)$  passes the mass  $dM$  located at  $(\mathbf{X}', Z)$ , the resulting

deflection (2.1) is

$$d\lambda = \frac{4G \rho(\mathbf{X}', Z) dV}{c^2} \frac{\mathbf{X} - \mathbf{X}'}{|\mathbf{X} - \mathbf{X}'|^2}. \quad (2.2)$$

However, after this infinitesimal deflection, the light ray is no longer travelling parallel to the  $Z$ -axis. In order to make the following calculations possible, the *Born approximation* is used, in which this effect is neglected due to the smallness of the deflections in the linear regime of gravity. The total deflection due to the mass distribution can then be calculated by first integrating, for a fixed position  $\mathbf{X}$  of the light ray, over the location  $\mathbf{X}'$  of masses in a single plane of constant  $Z$ , and subsequently over all such planes from the origin of the ray to the observer.<sup>1</sup> The result is given by the integral

$$\lambda(\mathbf{X}) = \frac{4G}{c^2} \iint d^2 X' dZ' \rho(\mathbf{X}', Z) \frac{\mathbf{X} - \mathbf{X}'}{|\mathbf{X} - \mathbf{X}'|^2}. \quad (2.3)$$

The integration of the mass density  $\rho(\mathbf{X}, Z)$  along the line of sight  $Z$  can be carried out independently and contained in the definition of a *surface mass density*

$$\Sigma(\mathbf{X}) = \int dZ \rho(\mathbf{X}, Z). \quad (2.4)$$

The *deflection angle*<sup>2</sup> can therefore be written entirely in terms of two-dimensional quantities

$$\lambda(\mathbf{X}) = \frac{4G}{c^2} \int d^2 X' \Sigma(\mathbf{X}') \frac{\mathbf{X} - \mathbf{X}'}{|\mathbf{X} - \mathbf{X}'|^2}, \quad (2.5)$$

and the three-dimensional details of the matter distribution have been absorbed completely. It is noted that two approximations were used in the derivation of this result, first the linearity of gravity, and secondly the *thin lens approximation* that light continues to travel in the original direction while being deflected. There are situations in which these approximations break down and which must be handled differently [86]. When the formalism of gravitational lensing is applied to the reconstruction of strong lenses, as is done in this work, these assumptions are very well fulfilled.

## 2.2 The lens equation

The thin lens approximation requires the matter distribution to be localised within a line-of-sight region that is small with respect to the total light travel distance.

<sup>1</sup>For the Born approximation to be valid, all planes outside of a small region should be empty.

<sup>2</sup>This deflection angle is the *physical* deflection angle, denoted here and in the following by  $\lambda$ . Other common notation is  $\hat{\alpha}$  with a hat [86, 87]. This can however lead to confusion with the *scaled* deflection angle  $\alpha$ , which will be introduced shortly.

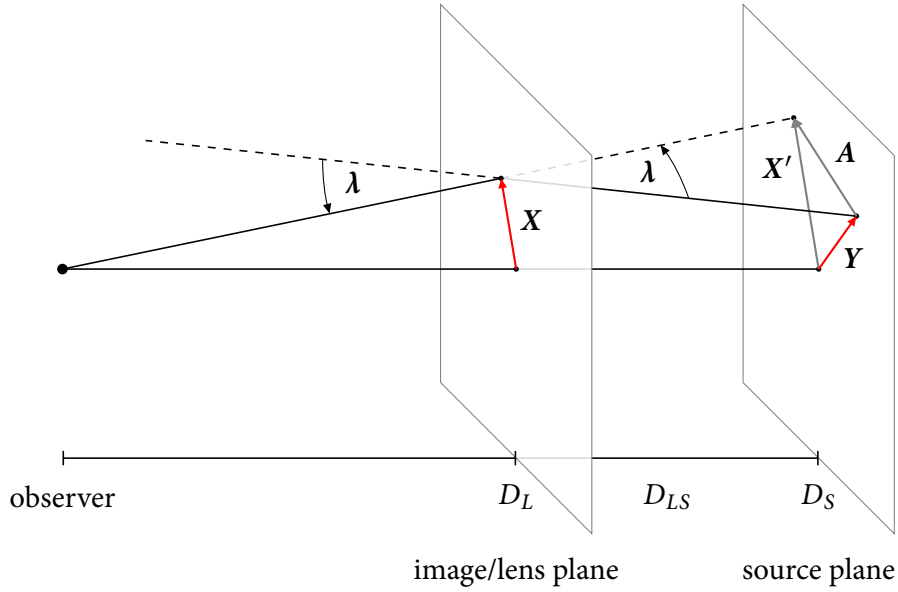


Figure 2.1: Geometry of a two-plane gravitational lens. Light rays from origin  $Y$  on the source plane arrive at observed position  $X$  on the image plane, where they are deflected by an angle  $\lambda$  towards the observer.

Since the deflection properties are determined by the projected two-dimensional surface mass density (2.4), a deflector is described as a *lens plane* perpendicular to the line of sight. Any number of lens planes can be employed in the description of a physical system [78], but for lens reconstruction, generally only the *two-plane system* is of practical interest. It consists of a *source plane*, which contains the surface brightness distribution of the background sources before lensing, and a single lens plane, called the *image plane*, as it describes the flat sky which is actually observed.

Figure 2.1 shows the geometry of such a two-plane lens system. In the thin lens approximation, a light ray travels from its origin  $Y$  on the source plane to  $X$  on the image plane. There, the gravitational pull of the lens changes the direction of the ray by the deflection angle  $\lambda$  towards the observer, so that  $X$  becomes the apparent origin of the ray on the image plane. The angular diameter distances to the lens plane, source plane, and between the planes are  $D_L$ ,  $D_S$ , and  $D_{LS}$ , respectively.

**Lens equation.** Given a two-plane lens system as shown, it is possible to find the origin  $Y$  of a light ray from its observed position  $X$  and the deflection angle  $\lambda$ . The projection of  $X$  from image plane to source plane is

$$\mathbf{X}' = \frac{D_S}{D_L} \mathbf{X}. \quad (2.6)$$

For a sufficiently small deflection angle  $\lambda$ , the projection onto the source plane is

$$\mathbf{A} = D_{LS} \boldsymbol{\lambda} . \quad (2.7)$$

The simple relation  $\mathbf{Y} + \mathbf{A} = \mathbf{X}'$  can therefore be rearranged into the *lens equation*

$$\mathbf{Y} = \frac{D_S}{D_L} \mathbf{X} - D_{LS} \boldsymbol{\lambda}(\mathbf{X}) , \quad (2.8)$$

where the dependency of the deflection angle  $\lambda$  on  $\mathbf{X}$  has been made explicit. The source plane position  $\mathbf{Y}$  is therefore a function of the observed position  $\mathbf{X}$  on the image plane, and can be calculated if  $\lambda(\mathbf{X})$  is known.

**The scaled deflection angle.** There is a remaining dependency on the angular diameter distances  $D_L$ ,  $D_S$  and  $D_{LS}$  in the lens equation, which can be removed in order to make the problem purely geometrical. Introducing angular positions  $\mathbf{x}$  and  $\mathbf{y}$  on the image and source plane defined by

$$D_L \mathbf{x} = \mathbf{X} , \quad D_S \mathbf{y} = \mathbf{Y} \quad (2.9)$$

into the lens equation and dividing both sides by  $D_S$  yields

$$\mathbf{y} = \mathbf{x} - \frac{D_{LS}}{D_S} \boldsymbol{\lambda}(D_L \mathbf{x}) , \quad (2.10)$$

where the scaling of the image plane position has cancelled out. This suggests the definition of the *scaled deflection angle*

$$\boldsymbol{\alpha}(\mathbf{x}) = \frac{D_{LS}}{D_S} \boldsymbol{\lambda}(D_L \mathbf{x}) \quad (2.11)$$

to contain the remaining dependency on  $D_{LS}$  and  $D_S$ . The lens equation can hence be written entirely in angular coordinates as

$$\mathbf{y} = \mathbf{x} - \boldsymbol{\alpha}(\mathbf{x}) , \quad (2.12)$$

where the dependency on  $D_{LS}$  and  $D_S$  has apparently been removed.

**Dimensionless quantities.** Of course, the dependency on the angular diameter distances is so far only hidden inside the scaled deflection angle. Inserting the integral form (2.5) of the physical deflection angle  $\lambda$  into definition (2.11) reveals the physical relation between the scaled deflection angle  $\boldsymbol{\alpha}$  and the surface mass density  $\Sigma$  as

$$\boldsymbol{\alpha}(\mathbf{x}) = \frac{D_{LS}}{D_S} \frac{4G}{c^2} \int d^2 X' \Sigma(\mathbf{X}') \frac{D_L \mathbf{x} - \mathbf{X}'}{|D_L \mathbf{x} - \mathbf{X}'|^2} . \quad (2.13)$$

### 2.3 Deflection potential and Poisson equation

10

By transforming the integral to angular coordinates  $D_L \mathbf{x}' = \mathbf{X}'$ , this can further be simplified to

$$\boldsymbol{\alpha}(\mathbf{x}) = \frac{1}{\pi} \int d^2x' \kappa(\mathbf{x}') \frac{\mathbf{x} - \mathbf{x}'}{|\mathbf{x} - \mathbf{x}'|^2}, \quad (2.14)$$

where the *dimensionless surface mass density* or *convergence* was introduced as

$$\kappa(\mathbf{x}) = \frac{4\pi G}{c^2} \frac{D_L D_{LS}}{D_S} \Sigma(D_L \mathbf{x}). \quad (2.15)$$

The additional factor of  $\pi$  is a natural choice: this will be seen shortly from the Poisson equation for lensing, as well as later in the calculation of  $\kappa$  for circularly symmetric lenses. The definition of  $\kappa$  is often written as the ratio

$$\kappa(\mathbf{x}) = \frac{\Sigma(D_L \mathbf{x})}{\Sigma_{\text{cr}}} \quad (2.16)$$

of surface mass density  $\Sigma$  and the *critical surface mass density*

$$\Sigma_{\text{cr}} = \frac{c^2}{4\pi G} \frac{D_S}{D_L D_{LS}}, \quad (2.17)$$

which emphasises the fact that  $\kappa$  is dimensionless. Lenses with  $\Sigma > \Sigma_{\text{cr}}$ ,  $\kappa > 1$  are “strong” and can produce multiple images and other phenomena, which will be listed shortly.

The quantities  $\boldsymbol{\alpha}$  and  $\kappa$  are generally preferable in lens reconstruction due to their dimensionless nature. With these definitions, is possible to build a model of the lens that is independent of the angular diameter distances  $D_L$ ,  $D_S$  and  $D_{LS}$ , which might not be available for a given observation. If physical quantities such as the mass of a lens are required, they can be calculated from the dimensionless results through the appropriate equations, e.g. (2.16). Therefore, unless explicitly stated otherwise, “deflection angle” and “surface mass density” in the following will always refer to  $\boldsymbol{\alpha}$  and  $\kappa$ , respectively.

### 2.3 Deflection potential and Poisson equation

The integral (2.14) for the deflection angle  $\boldsymbol{\alpha}$  is that of a classical two-dimensional force field, where the surface mass density  $\kappa$  plays the role of a charge density. Since the rotation of the deflection field vanishes identically,

$$\nabla \times \boldsymbol{\alpha} \equiv 0, \quad (2.18)$$

it follows that there exists a function  $\psi$ , called the potential, so that the deflection angle is the gradient

$$\boldsymbol{\alpha}(\mathbf{x}) = \nabla \psi(\mathbf{x}). \quad (2.19)$$

A suitable potential function can be constructed directly by inserting identity

$$\frac{\mathbf{x} - \mathbf{x}'}{|\mathbf{x} - \mathbf{x}'|^2} = \nabla \log |\mathbf{x} - \mathbf{x}'| \quad (2.20)$$

into integral (2.14), where the gradient operator  $\nabla$  acts on  $\mathbf{x}$  alone, and changing the order of integration and differentiation, resulting in

$$\boldsymbol{\alpha}(\mathbf{x}) = \frac{1}{\pi} \nabla \int d^2x' \kappa(\mathbf{x}') \log |\mathbf{x} - \mathbf{x}'|. \quad (2.21)$$

This implies that the *deflection potential* is given by

$$\psi(\mathbf{x}) = \frac{1}{\pi} \int d^2x' \kappa(\mathbf{x}') \log |\mathbf{x} - \mathbf{x}'|, \quad (2.22)$$

and the relation  $\boldsymbol{\alpha} = \nabla\psi$  is fulfilled by construction.

**Poisson equation.** In keeping with the field theory analogy, the potential  $\psi$  can further be related directly to the surface mass density  $\kappa$  (i.e. the charge) through a differential equation. Applying the two-dimensional Laplacian  $\nabla^2 = \partial_1^2 + \partial_2^2$  to both sides of equation (2.22) for the potential  $\psi$ , and changing again the order of differentiation and integration, results in

$$\nabla^2 \psi(\mathbf{x}) = \frac{1}{\pi} \int d^2x' \kappa(\mathbf{x}') \nabla^2 \log |\mathbf{x} - \mathbf{x}'|. \quad (2.23)$$

Because  $(2\pi)^{-1} \log |\mathbf{x}|$  is the Green's function of the two-dimensional Laplacian, the Dirac delta function

$$\nabla^2 \log |\mathbf{x} - \mathbf{x}'| = 2\pi \delta(\mathbf{x} - \mathbf{x}') \quad (2.24)$$

can be used to resolve the integral. The result is the *Poisson equation*

$$\nabla^2 \psi(\mathbf{x}) = 2\kappa(\mathbf{x}) \quad (2.25)$$

of gravitational lensing.

## 2.4 Convergence, shear and magnification

In order to understand the local transformation of images of lensed sources, it is possible to linearise lens equation (2.12) at a given point  $\mathbf{y}_0 = \boldsymbol{\gamma}(\mathbf{x}_0)$ . The result can be written as

$$\mathbf{y} = \mathbf{y}_0 + \mathbf{A}(\mathbf{x} - \mathbf{x}_0), \quad (2.26)$$

where the *magnification matrix*  $\mathbf{A}$  is the Jacobian of the transformation  $\boldsymbol{\gamma}(\mathbf{x})$

$$\mathbf{A} = \begin{pmatrix} 1 - \psi_{,11} & -\psi_{,12} \\ -\psi_{,12} & 1 - \psi_{,22} \end{pmatrix} \quad (2.27)$$

given in terms of derivatives of the deflection potential  $\nabla\psi = \boldsymbol{\alpha}$ .

**Convergence and shear.** The magnification matrix  $\mathbf{A}$  is more commonly written in the form

$$\mathbf{A} = \begin{pmatrix} 1 - \kappa - \gamma_1 & -\gamma_2 \\ -\gamma_2 & 1 - \kappa + \gamma_1 \end{pmatrix}, \quad (2.28)$$

which uses the traditional lensing quantities of *convergence*

$$\kappa(\mathbf{x}) = \frac{1}{2} (\psi_{,11}(\mathbf{x}) + \psi_{,22}(\mathbf{x})) \quad (2.29)$$

and the two components of the *shear*

$$\begin{aligned} \gamma_1(\mathbf{x}) &= \frac{1}{2} (\psi_{,11}(\mathbf{x}) - \psi_{,22}(\mathbf{x})), \\ \gamma_2(\mathbf{x}) &= \psi_{,12}(\mathbf{x}). \end{aligned} \quad (2.30)$$

The convergence  $\kappa$  is identical to the surface mass density, and definition (2.29) is merely a reformulation of Poisson equation (2.25).

**Complex shear.** Due to the peculiar transformation of the shear under rotations of the coordinate system, it is often advantageous to use the *complex shear*

$$\gamma = \gamma_1 + i\gamma_2 = |\gamma| e^{i2\theta_\gamma} \quad (2.31)$$

with magnitude  $|\gamma|$  and orientation  $\theta_\gamma$  instead of the two components  $\gamma_1$  and  $\gamma_2$  to characterise a lens. This form makes it clear that the shear is not a two-dimensional vector but a *polar*, which changes its angle twice as fast as a vector under rotations of the coordinate system. Relations

$$|\gamma|^2 = \gamma_1^2 + \gamma_2^2, \quad \theta_\gamma = \frac{1}{2} \arctan(\gamma_1, \gamma_2) \quad (2.32)$$

for the individual components follow directly from the definition.

**Magnification.** From the linearised lens equation (2.26), it follows that a source subtending a small area  $dA$  in the image plane subtends an area  $dA' = |\det \mathbf{A}| dA$  in the source plane. This leads to the definition of the *magnification*

$$\mu = \det \mathbf{A}^{-1} \quad (2.33)$$

as the inverse of the determinant of the magnification matrix. Explicit calculation of the determinant shows that the magnification is given by the combination

$$\mu = \frac{1}{(1 - \kappa)^2 - |\gamma|^2} \quad (2.34)$$

of convergence  $\kappa$  and shear  $\gamma$ . The magnification is one of the most important lensing quantities: Not only does it describe the increased luminosity of a lensed source with finite size, it also governs many of the phenomena associated with strong lensing, which will now be investigated.

## 2.5 Multiple images and strong lensing

The interesting regime for lens reconstruction is that of *strong lensing*. When a source plane position  $\mathbf{y}$  admits more than one solution  $\mathbf{x}$  for lens equation (2.12), there will be *multiple images* of the same source plane regions on the image plane. The appearance and distribution of multiple images is governed by the *critical structure* of the lens, which treats the emergence and disappearance of solutions of the lens equation over the image plane. Many properties of gravitational lenses can be understood from the study of their critical structure [79], which is a fascinating subject in itself, even though only a few basic results will be used here. Particular examples of critical structures can be found in the lens models of Chapter 3.

**Critical lines.** On the image plane, a lens can produce smooth *critical lines* on which the Jacobian  $\det \mathbf{A}$  of the magnification matrix and therefore the inverse magnification (2.33) vanishes,

$$\mu^{-1} = (1 - \kappa)^2 - |\gamma|^2 = 0 . \quad (2.35)$$

This leads to a nominally infinite magnification of images on the critical line in theory, although the approximations of gravitational lensing break down and the physical magnification remains finite. Nevertheless, very high magnifications can occur near the critical lines of real lenses, as observed in phenomena such as bright arcs and Einstein rings.

**Caustics.** The critical lines correspond to *caustics* on the source plane, which can be found by mapping the smooth lines through lens equation (2.12). The resulting lines are not necessarily smooth, but can develop *cusps* and *folds*. The number of images a source produces depends on its position relative to the caustics of the lens; sources outside of the caustic structure are singly-imaged, and every time a caustic is crossed, the number of images increases or decreases by two.<sup>3</sup>

---

<sup>3</sup>Exceptions are situations of high symmetry such as circular sources, where two of the images can be degenerate.

## 3 Lens models

### 3.1 The building blocks of lenses

The reconstruction method introduced shortly requires a parametric model of the lens. A number of commonly used models for galaxy-scale lenses are described here, giving a brief summary of their lensing properties. The present selection of lenses closely mirrors the LENSED software for lens reconstruction [102, 103], which is developed in the coming chapters. This list is by no means exhaustive, and many other models are readily found in the literature [49, 86, 87]. Most of the lens models follow a given profile with circular or elliptical symmetry, for which the deflection, shear, magnification and critical structure can often be worked out analytically. The existence of closed-form expressions for at least the deflection is an immense advantage for the intended application in lens reconstruction, as any other form of numerical calculation is likely too slow to be practically useful. An exception to this rule are lenses for which quickly converging series have been developed, such as the elliptical power law profile lens examined in Chapter 4.

**Coordinate transformation.** Without loss of generality, the following models assume a coordinate system where the lens is located at the origin. Similarly, for the elliptical models, the coordinate system is rotated so that the major axis of the profile coincides with the  $x_1$ -axis of the coordinate system. This can always be achieved by a suitable coordinate transformation

$$\boldsymbol{x} \mapsto \boldsymbol{x}' = \mathbf{R}_{(-\theta_L)} (\boldsymbol{x} - \boldsymbol{x}_L) , \quad (3.1)$$

where  $\mathbf{R}_{(-\theta_L)}$  is the inverse rotation matrix for the position angle  $\theta_L$ , and  $\boldsymbol{x}_L$  is the lens position. When using the lens models in a practical application, the world coordinates can be quickly transformed to “lens coordinates” before calculating the desired lensing quantity.

### 3.2 The point mass

The dimensionless surface mass density (2.15) of the *point mass* can be written as

$$\kappa(\boldsymbol{x}) = \pi r_{\text{E}}^2 \delta(\boldsymbol{x}) , \quad (3.2)$$

where  $\delta(\mathbf{x})$  is the Dirac delta function, and  $r_E$  is the *Einstein radius* of the lens, which is related to its mass  $m$  by

$$r_E = \sqrt{\frac{4Gm}{c^2} \frac{D_{LS}}{D_L D_S}}. \quad (3.3)$$

This radius — which here is given in angular coordinates, i.e. the *Einstein angle* — corresponds to a length

$$R_E = D_L r_E = \sqrt{\frac{4Gm}{c^2} \frac{D_L D_{LS}}{D_S}} \quad (3.4)$$

in physical coordinates.

**Deflection.** Inserting the surface mass density (3.2) into integral (2.14) for the scaled deflection angle yields

$$\boldsymbol{\alpha}(\mathbf{x}) = r_E^2 \frac{\mathbf{x}}{|\mathbf{x}|^2}. \quad (3.5)$$

as the deflection angle of the point mass.

**Potential.** The potential (2.22) of the point mass can either be integrated directly,

$$\psi(\mathbf{x}) = r_E^2 \log |\mathbf{x}|, \quad (3.6)$$

or alternatively be found by inserting  $\mathbf{x}/|\mathbf{x}|^2 = \nabla \log |\mathbf{x}|$  into  $\boldsymbol{\alpha}$  as has been done when the deflection potential was first derived.

**Shear.** The two components of the shear (2.30) for the point mass lens are

$$\gamma_1(\mathbf{x}) = -r_E^2 \frac{x_1^2 - x_2^2}{|\mathbf{x}|^4}, \quad \gamma_2(\mathbf{x}) = -r_E^2 \frac{2x_1 x_2}{|\mathbf{x}|^4}, \quad (3.7)$$

and the associated complex shear (2.31) is

$$\gamma(r, \theta) = -\frac{r_E^2}{r^2} e^{i2\theta}, \quad (3.8)$$

where  $r$  and  $\theta$  are polar coordinates.

**Magnification, critical structure.** With the convergence (3.2) and shear (3.8) known, the magnification (2.34) of the point mass is

$$\mu^{-1}(\mathbf{x}) = 1 - \frac{r_E^4}{|\mathbf{x}|^4}, \quad (3.9)$$

For the magnification of the point mass lens, condition (2.35) for a critical line is

$$\mu^{-1}(\mathbf{x}_{\text{cr}}) = 0 \iff |\mathbf{x}_{\text{cr}}| = r_E . \quad (3.10)$$

The critical line is therefore a circle around the centre of the lens with (angular) radius  $r_E$  as expected. The caustic structure of the lens can be determined by using lens equation (2.12), i.e.

$$\mathbf{y} = \mathbf{x} - \boldsymbol{\alpha}(\mathbf{x}) = \mathbf{x} - r_E^2 \frac{\mathbf{x}}{|\mathbf{x}|^2} , \quad (3.11)$$

to map the critical line  $|\mathbf{x}_{\text{cr}}| = r_E$  to the corresponding caustic  $\mathbf{y}_{\text{cr}}$  on the source plane. The result is, for any choice of  $\mathbf{x}_{\text{cr}}$ ,

$$\mathbf{y}_{\text{cr}} = \mathbf{y}(\mathbf{x}_{\text{cr}}) = \mathbf{0} , \quad (3.12)$$

and hence the caustic collapses to a point at the origin.

### 3.3 Isothermal profiles

One of the most commonly encountered and physically motivated parametric lens models are those of the family of *isothermal* profiles. The three-dimensional mass density of such lenses follows an inverse-square law  $\rho \propto r^{-2}$ , and the simplest such form results in the surface mass density profile

$$\kappa(r) = \frac{1}{2} \frac{b}{r} , \quad (3.13)$$

where  $r$  is the radius and  $b$  is the scale length of the isothermal profile. Since the density has circular symmetry and formally diverges for  $r \rightarrow 0$ , the profile (3.13) is called a *singular isothermal sphere* (SIS). The singularity at the origin can be fixed by introducing a softening scale or core radius  $s$  as

$$\kappa(r) = \frac{1}{2} \frac{b}{\sqrt{r^2 + s^2}} , \quad (3.14)$$

and the resulting profile, still circularly symmetric but no longer diverging, is called a *non-singular isothermal sphere* (NSIS). For more realistic models, density profiles can be made elliptical by stretching the  $x_1$ -coordinate by a factor of  $1/q$ , so that the isodensity contours are ellipses with an axis ratio of  $q$ . The results are the *singular isothermal ellipsoid* (SIE) with density profile

$$\kappa(\mathbf{x}) = \frac{1}{2} \frac{b}{\sqrt{q^2 x_1^2 + x_2^2}} , \quad (3.15)$$

which diverges near the origin, and the *non-singular isothermal ellipsoid* (NSIE)

$$\kappa(\mathbf{x}) = \frac{1}{2} \frac{b}{\sqrt{q^2 (x_1^2 + s^2) + x_2^2}} . \quad (3.16)$$

The lensing properties of elliptical lenses are investigated in detail in Chapter 4.

**Deflection.** It is noted that all other members of the isothermal family are special cases of the NSIE, obtained as the limits  $s \rightarrow 0$  to go from non-singular to singular, and  $q \rightarrow 0$  to go from ellipsoid to sphere. Hence, it suffices to find the deflection of the NSIE, which is [48, 50, 54]

$$\begin{aligned}\alpha_1(\mathbf{x}) &= \frac{b}{\sqrt{1-q^2}} \arctan\left(\frac{x_1 \sqrt{1-q^2}}{\xi+s}\right), \\ \alpha_2(\mathbf{x}) &= \frac{b}{\sqrt{1-q^2}} \operatorname{arctanh}\left(\frac{x_2 \sqrt{1-q^2}}{\xi+q^2 s}\right).\end{aligned}\tag{3.17}$$

where  $\xi = \sqrt{q^2(x_1^2 + s^2) + x_2^2}$ . The SIE deflection follows by simply setting  $s = 0$  in the above expressions. For the NSIS, the limit  $q \rightarrow 0$  yields a deflection

$$\alpha(\mathbf{x}) = \frac{b \mathbf{x}}{\sqrt{|\mathbf{x}|^2 + s^2 + s}},\tag{3.18}$$

and the SIS follows once more by setting  $s = 0$ .

**Potential.** The deflection potential (2.22) for the NSIE profile is given by

$$\psi = x_1 \alpha_1 + x_2 \alpha_2 - b s \log\left\{(\xi+s)^2 + (1-q^2)x_1^2\right\},\tag{3.19}$$

from which the special cases SIE, NSIS and SIS follow as before. In particular, the potential of the SIE is

$$\psi = x_1 \alpha_1 + x_2 \alpha_2,\tag{3.20}$$

which will prove useful for the case of a general power law.

**Magnification, critical structure.** The magnification of the NSIE is given by

$$\mu^{-1} = 1 - \frac{b}{\xi} - \frac{b}{\xi} \frac{b s}{(\xi+s)^2 + (1-q^2)x_1^2}.\tag{3.21}$$

For the SIE, this simplifies to

$$\mu^{-1} = 1 - \frac{b}{\xi} = 1 - 2\kappa.\tag{3.22}$$

It is clear that the isocontours of the SIE are at the same time contours of constant magnification. The critical line (2.35) is given by the  $\kappa = 1/2$  isodensity contour, which makes it the ellipse with semi-minor axis  $b$ . The scale length  $b$  can therefore reasonably be considered the Einstein radius of the SIE (and of course SIS) model.

**Fixed mass parameterisation.** Instead of using the scale length  $b$  (which is the Einstein radius of the lens), the SIE can be parameterised by the scale length  $b_{\text{SIS}}$  of a SIS containing the same mass within the critical line. The relationship is the following. The dimensionless mass enclosed in the critical line of the SIE is

$$m = \frac{2\pi}{q} \int_0^b dR R \kappa(R) = \frac{\pi b^2}{q}. \quad (3.23)$$

The dependency of the mass on  $b$  and  $q$  implies that in order to keep the mass of the model fixed under changes of the ellipticity, the length  $b$  has to scale as  $q^{1/2}$ . By introducing the parameter

$$b_{\text{SIS}} = \frac{b}{\sqrt{q}} \quad (3.24)$$

the dependency of the mass on  $q$  is eliminated. The parameter  $b_{\text{SIS}}$  is, as the name implies, the Einstein radius of a SIS ( $q = 1$ ) with the same mass  $m$ . This definition has a simple geometrical interpretation: instead of the semi-minor axis  $b$  of the critical line, the new parameter uses the geometric mean  $b/\sqrt{q}$  of the semi-minor axis  $b$  and semi-major axis  $b/q$ . This parameterisation is widely used in practice, for example in the applications of Chapter 8 and 9.

### 3.4 Navarro, Frenk and White profiles

Based on numerical simulations, Navarro, Frenk and White found a “universal” density profile [69]

$$\rho(r) = \frac{\rho_s}{(r/r_s)(1+r/r_s)^2} \quad (3.25)$$

for dark matter halos, where  $\rho_s$  is the density normalisation and  $r_s$  is a scale radius. The corresponding surface mass density of this model is [7]

$$\kappa(r) = 2\kappa_s \frac{1 - \mathcal{F}(r/r_s)}{(r/r_s)^2 - 1}, \quad (3.26)$$

where  $\kappa_s = \rho_s r_s / \Sigma_{\text{cr}}$  is a normalising constant and the function  $\mathcal{F}$  is defined as

$$\mathcal{F}(x) = \begin{cases} \frac{1}{\sqrt{x^2-1}} \arctan \sqrt{x^2-1}, & x > 1, \\ \frac{1}{\sqrt{1-x^2}} \operatorname{arctanh} \sqrt{1-x^2}, & x < 1, \\ 1, & x = 1. \end{cases} \quad (3.27)$$

The Navarro, Frenk and White (NFW) lens is frequently used to model the dark matter halo of galaxies. Similar to SIE and NSIE, the NFW profile is sometimes made elliptical using transform  $r \mapsto \sqrt{q^2 x_2^2 + x_1^2}$ . However, the resulting elliptical lens is difficult to treat analytically, and usually used in combination with fully numerical methods.

### 3.5 Mass sheets

Lenses with constant surface mass densities  $\kappa(\mathbf{x}) = \kappa_0$ , so-called *mass sheets*, play an important role in the theory of gravitational lenses. They feature the simple deflection and potential

$$\boldsymbol{\alpha}(\mathbf{x}) = \kappa_0 \mathbf{x}, \quad \psi(\mathbf{x}) = \frac{\kappa_0}{2} |\mathbf{x}|^2, \quad (3.28)$$

and this seemingly innocent mass model would be entirely uninteresting were it not for the *mass sheet transform* [33, 41], which has far-reaching consequences for lens modelling as a whole.

**The mass sheet transform.** Assuming that a good reconstruction  $\kappa$  of the mass distribution of a lens system has been found, a mass sheet  $\kappa_0 = 1 - t$  is added to it, and the original  $\kappa$  is scaled by  $t$ , so that

$$\kappa_t(\mathbf{x}) = t \kappa(\mathbf{x}) + (1 - t). \quad (3.29)$$

is a family of mass models related to  $\kappa$ . One might ask how well the observation is reconstructed by any of the mass models  $\kappa_t$ . The deflection of the new model is

$$\boldsymbol{\alpha}_t(\mathbf{x}) = t \boldsymbol{\alpha}(\mathbf{x}) + (1 - t) \mathbf{x}, \quad (3.30)$$

and inserting this into lens equation (2.12), one finds

$$\mathbf{y} = \mathbf{x} - \boldsymbol{\alpha}_t(\mathbf{x}) = t(\mathbf{x} - \boldsymbol{\alpha}(\mathbf{x})) \iff \mathbf{y}/t = \mathbf{x} - \boldsymbol{\alpha}(\mathbf{x}). \quad (3.31)$$

It follows that the deflection of the whole family of mass models  $\kappa_t$  is equivalent modulo an overall scaling of the source plane by a factor of  $t$ . Because such a scaling is unobservable, there is no way to distinguish any two members of the family of mass models.

**The mass sheet transform and parametric models.** The mass sheet transform represents a severe limitation to the possibility of ever reconstructing general mass distributions in a well-constrained way. However, the problem is somewhat alleviated when parametric models are used for the reconstruction. If the mass distribution  $\kappa$  follows a given profile, e.g. the SIE profile, the mass sheet transform  $\kappa + \kappa_0$  generally no longer follows that profile, e.g.  $\kappa + \kappa_0$  is no longer a SIE. Hence, by restricting the reconstruction to parametric lenses, the mass sheet transform no longer applies [30], since the family of equivalent lens models  $\kappa_t$  is generally restricted to the single member following the chosen profile.

### 3.6 External shear

In reconstructions, it is often necessary to consider the immediate environment of the lens system, as objects are rarely isolated enough to not feel the influence of

a nearby deflector. As long as the mass distributions do not physically overlap, a nearby object cannot contribute convergence  $\kappa$  to the deflection of light. However, it can contribute an *external shear*  $\gamma$ . Using the magnification matrix (2.28), the deflection of a lens component with  $\kappa = 0$ ,  $\gamma \neq 0$  is given to first order by the matrix product

$$\boldsymbol{\alpha}(\mathbf{x}) = \begin{pmatrix} \gamma_1 & \gamma_2 \\ \gamma_2 & -\gamma_1 \end{pmatrix} \mathbf{x} = \gamma \begin{pmatrix} \cos(2\theta_\gamma) & \sin(2\theta_\gamma) \\ \sin(2\theta_\gamma) & -\cos(2\theta_\gamma) \end{pmatrix} \mathbf{x}. \quad (3.32)$$

Lens components of external shear are frequently used in the reconstruction of observations, and can be found e.g. in Chapter 9.

## 4 The elliptical power law profile lens

The contents of this chapter have been published as N. Tessore and R. B. Metcalf, *The elliptical power law profile lens*, *A&A* 580 (Aug. 2015) A79, arXiv: [1507.01819](https://arxiv.org/abs/1507.01819).

### 4.1 Elliptical lenses

The strong lensing reconstructions presented here require an approximation of the lens system by a parametric model. The initial model for a lens system is often a spherically symmetric mass distribution  $\rho(\mathbf{x}, z)$  in three dimensions, which leads to a circularly symmetric surface mass density  $\kappa(\mathbf{x}) = \kappa(r)$  on the lens plane. Many of the classical lenses fall into this category, such as isothermal spheres or the Navarro, Frenk and White profile [7, 69]. Because of the high level of symmetry, the lensing properties of circularly symmetric lenses can usually be worked out analytically. On the other hand, these lenses can hardly be believed to offer a realistic description of the real mass distributions, even when external shear is considered in order to break some level of symmetry.

The next step in approximating real lens systems is therefore to turn the known lenses with spherical symmetry into ellipsoids by rescaling an arbitrary axis of either the surface mass density or the deflection potential, fixing the other through the Poisson equation [48]. Choice of an elliptical potential — often called a pseudo-elliptical model — simplifies the problem, because other lensing quantities such as shear, deflection, and convergence can all be expressed in terms of derivatives of the potential, thus eliminating the need to solve complicated integrals. However, this approach can lead to unrealistic and unphysical surface mass densities with peanut-shaped isodensity contours or negative values. These problems become more acute as the ellipticity increases, and the approach is generally unsuited for axis ratios below  $q \approx 0.5$  [48].

More realistic lens models might therefore be created from elliptical surface mass densities. The properties of elliptical lenses were first described by Bourassa, Kantowski and Norton [15] and Bourassa and Kantowski [14], who introduced a complex formalism of gravitational lensing to simplify the necessary calculations. The expressions for the two-dimensional real deflection angle were later derived by Schramm [89]. However, due to the loss of symmetry, it is often no longer possible to find the properties of elliptical lenses analytically. Notable exceptions are the singular and nonsingular isothermal ellipsoids described by Kassiola and Kovner [48] and then fully analysed by Kormann, Schneider and Bartelmann [54]

using the complex formalism. The results, which are beautiful, simple closed-form solutions, are widely applicable and the workhorse of lens reconstruction today. Despite the success of this model, current high resolution observations can often benefit from additional flexibility in the assumed lens profile, and no equally well-established elliptical lens with a simple mathematical form and numerical implementation is available.

**Elliptical profiles.** In order to turn a circularly symmetric  $\kappa(r)$  into an elliptical surface mass density, the  $x_1$ -axis is stretched by a factor of  $1/q$ , where  $0 < q \leq 1$  is a constant parameter of the elliptical profile. It is clear that after this operation, the formerly circular isodensity contours  $r = \text{const}$  have indeed become ellipses with semi-major axis  $r/q$ , semi-minor axis  $r$ , and axis ratio  $q$ . Hence the elliptical surface mass density  $\kappa(R)$  results from the simple substitution

$$\kappa(r) \mapsto \kappa(R), \quad (4.1)$$

where  $R$  is the *elliptical radius* defined by

$$R = \sqrt{q^2 x_1^2 + x_2^2}, \quad (4.2)$$

i.e. the semi-minor axis of the ellipse passing through  $x_1, x_2$ . The corresponding *elliptical angle* defined by<sup>1</sup>

$$\varphi = \arctan(qx_1, x_2) \quad (4.3)$$

is the polar angle of position  $x_1, x_2$  in the original circular symmetry. The inverse coordinate transformation from elliptical coordinates  $(R, \varphi)$  back to the physical coordinates  $(x_1, x_2)$  is

$$\begin{aligned} x_1 &= R/q \cos(\varphi), \\ x_2 &= R \sin(\varphi), \end{aligned} \quad (4.4)$$

where  $R$  and  $\varphi$  are limited to  $R > 0$  and  $\varphi \in [0, 2\pi)$ , respectively. The elliptical symmetry of the surface mass density  $\kappa(R)$  is contained entirely in the choice of coordinates, and the form of the distribution remains unchanged.

**The complex formulation of lensing.** When working with elliptical surface mass distributions, it is most natural to work in the complex formulation of lensing for spheroidal mass distributions [14, 15, 17, 48, 54, 89]. Lens equation (2.12) in complex notation is

$$z' = z - \alpha(z), \quad (4.5)$$

---

<sup>1</sup>This definition uses the two-argument inverse tangent  $\arctan(x_1, x_2)$ , which respects the quadrant of  $x_1, x_2$  to return the correct angle.

where the two-dimensional vector quantities are replaced by the corresponding complex coordinate  $z = x_1 + i x_2$  and the complex deflection angle  $\alpha = \alpha_1 + i \alpha_2$ . The complex deflection angle  $\alpha$  follows from its two-dimensional definition (2.14) via the substitution  $\mathbf{x} \mapsto z, |\mathbf{x}|^2 \mapsto z z^*$  as

$$\alpha^*(z) = \frac{1}{\pi} \int dz' \frac{\kappa(z')}{z - z'}, \quad (4.6)$$

where the asterisk in  $\alpha^*$  denotes complex conjugation of the overall expression. The usual deflection potential becomes the real part of a complex potential  $\psi(z)$ , which is related to the complex deflection angle  $\alpha(z)$  through the use of Wirtinger derivatives [54, 89]

$$\alpha^*(z) = 2 \frac{\partial}{\partial z} \psi(z). \quad (4.7)$$

Similar relations can also be found for the second derivatives of the potential, namely the complex shear  $\gamma = \gamma_1 + i \gamma_2$ , given by

$$\gamma^*(z) = \frac{\partial}{\partial z} \alpha^*(z), \quad (4.8)$$

and the convergence  $\kappa$ , given by

$$\kappa(z) = \frac{\partial}{\partial z^*} \alpha^*(z). \quad (4.9)$$

Since the latter expression must recover the surface mass density identically, it serves as a direct check for the correctness of calculations.

**Deflection of an elliptical lens.** The complex deflection angle for an elliptical, homoeoidal mass distribution was given by Bourassa, Kantowski and Norton [15] and Bourassa and Kantowski [14]. Using the elliptical radius  $R$  defined in (4.2), the deflection angle of an elliptical surface mass density  $\kappa(R)$  is

$$\alpha^*(z) = 2 \frac{\sqrt{z^2}}{z} \int_0^{R(z)} dR' \frac{\kappa(R') R'}{\sqrt{q^2 z^2 - (1 - q^2) R'^2}}, \quad (4.10)$$

where  $R(z)$  is the semi-minor axis of the ellipse passing through point  $z$ . The factor in front of the integral is due to Bray [17]; it ensures the correct sign of the deflection in all quadrants of the complex plane. From the complex deflection angle (4.10) and the set of equations (4.7)–(4.9), all lens properties of an elliptical lens can now be derived.

## 4.2 Lens properties

The dimensionless surface mass density  $\kappa$  (i.e. the convergence) of a lens following a power law profile with circular symmetry is [32, 87]

$$\kappa(r) = \frac{2-t}{2} \left( \frac{b}{r} \right)^t, \quad (4.11)$$

where  $0 < t < 2$  is the slope of the profile,  $b > 0$  is the scale length and  $r > 0$  is the distance from the centre of the mass distribution. Such a profile arises from a spherically symmetric three-dimensional mass distribution  $\rho(r) \propto (b/r)^{t+1}$ . The power law profile lens is a versatile model; it contains as special cases the singular isothermal sphere for  $t = 1$ , the point mass for  $t = 2$ , and approximations of the central region of the Navarro, Frenk and White [69] and Moore et al. [65] profiles for  $t = 0$  and  $t = 1/2$ , respectively. Applying the transformation (4.1) to the circular profile (4.11) yields the elliptical surface mass density

$$\kappa(R) = \frac{2-t}{2} \left( \frac{b}{R} \right)^t \quad (4.12)$$

of the elliptical power law profile lens. Numerical recipes exist for the nonsingular variant of this model [6, 23, 88], but a more general analysis leads to a number of new results [104], which are presented here.

**Deflection.** Inserting the elliptical power law profile (4.12) into integral (4.10), the complex deflection angle can be calculated explicitly as

$$\begin{aligned} \alpha^*(z) &= \frac{2-t}{q} \frac{b^t}{z} \int_0^{R(z)} dR' R'^{1-t} \left( 1 - \frac{1-q^2}{q^2} \frac{R'^2}{z^2} \right)^{-1/2} \\ &= \frac{2-t}{2q} \frac{b^2}{z} \left( \frac{b}{R(z)} \right)^{t-2} \int_0^1 d\xi \xi^{-t/2} \left( 1 - \frac{1-q^2}{q^2} \frac{R(z)^2}{z^2} \xi \right)^{-1/2} \\ &= \frac{1}{q} \frac{b^2}{z} \left( \frac{b}{R(z)} \right)^{t-2} {}_2F_1 \left( \frac{1}{2}, 1 - \frac{t}{2}; 2 - \frac{t}{2}; \frac{1-q^2}{q^2} \frac{R(z)^2}{z^2} \right), \end{aligned} \quad (4.13)$$

where the change of variable  $R' \rightarrow \xi = R'^2/R(z)^2$  was used in the first step, and the integral representation of the Gaussian hypergeometric function  ${}_2F_1(a, b; c; z)$  was used in the second step. Because its parameters are related as  $c = a + b + 1/2$ , there is a quadratic transformation of the hypergeometric function [68, 72], and the complex deflection angle can further be simplified to

$$\alpha^*(R, \varphi) = \frac{2b}{1+q} \left( \frac{b}{R} \right)^{t-1} e^{-i\varphi} {}_2F_1 \left( 1, \frac{t}{2}; 2 - \frac{t}{2}; -\frac{1-q}{1+q} e^{-i2\varphi} \right), \quad (4.14)$$

where transformation (4.4) was applied to the complex coordinate  $z = x_1 + i x_2$ . For reference, the complex deflection angle before complex conjugation is

$$\alpha(R, \varphi) = \frac{2b}{1+q} \left(\frac{b}{R}\right)^{t-1} e^{i\varphi} {}_2F_1\left(1, \frac{t}{2}; 2 - \frac{t}{2}; -\frac{1-q}{1+q} e^{i2\varphi}\right). \quad (4.15)$$

This result is a beautiful factorisation of deflection  $\alpha$  into its (elliptical) radial and angular parts; a fact that will be exploited shortly for quick numerical calculations, despite the fact that the deflection contains a hypergeometric function.

**Deflection potential.** Taking inspiration from the deflection potential (3.20) of the singular isothermal ellipsoid, one finds that a potential solving equation (4.7) for complex deflection (4.14) is given by

$$\psi(z) = \frac{1}{2-t} \frac{z \alpha^*(z) + z^* \alpha(z)}{2}. \quad (4.16)$$

The familiarity is more obvious in real coordinates, where the potential becomes

$$\psi = \frac{x_1 \alpha_1 + x_2 \alpha_2}{2-t}. \quad (4.17)$$

It is clear that this potential can be calculated at very low cost if the deflection angle  $\alpha$  has already been found. Checking the result is tedious; one possibility is first substituting  $e^{-i\varphi} = (qx_1 - ix_2)/R$  and  $e^{-i2\varphi} = (qx_1 - ix_2)/(qx_1 + ix_2)$  in deflection (4.14) and subsequently expressing the Wirtinger derivative in (4.7) as  $\partial/\partial z = (\partial/\partial x_1 - i \partial/\partial x_2)/2$  in terms of real coordinates.

The complex potential (4.16) has no imaginary component, since the second factor  $z \alpha^* + z^* \alpha = 2 \operatorname{Re}(z \alpha^*)$  is evidently real. In its coordinate form (4.17), the potential can therefore be taken to be the real deflection potential (2.22) for which relation  $\alpha = \nabla \psi$  holds [89]. Figure 4.1 shows the potential for various settings of the power law slope  $t$  and axis ratio  $q$ . It has been noted that the potential is always “rounder” (i.e. less eccentric) than the surface mass density, and this effect is clearly visible.

**Shear.** Calculating the shear from the deflection as the Wirtinger derivative (4.8) is straightforward, and results in

$$\gamma^*(z) = -\kappa(z) \frac{z^*}{z} + (1-t) \frac{\alpha^*(z)}{z}. \quad (4.18)$$

For use in computations, the shear is more easily expressed in terms of elliptical coordinates  $R$  and  $\varphi$  as

$$\gamma(R, \varphi) = -e^{i2\varphi} \kappa(R) + (1-t) e^{i\varphi} \frac{\alpha(R, \varphi)}{R}, \quad (4.19)$$

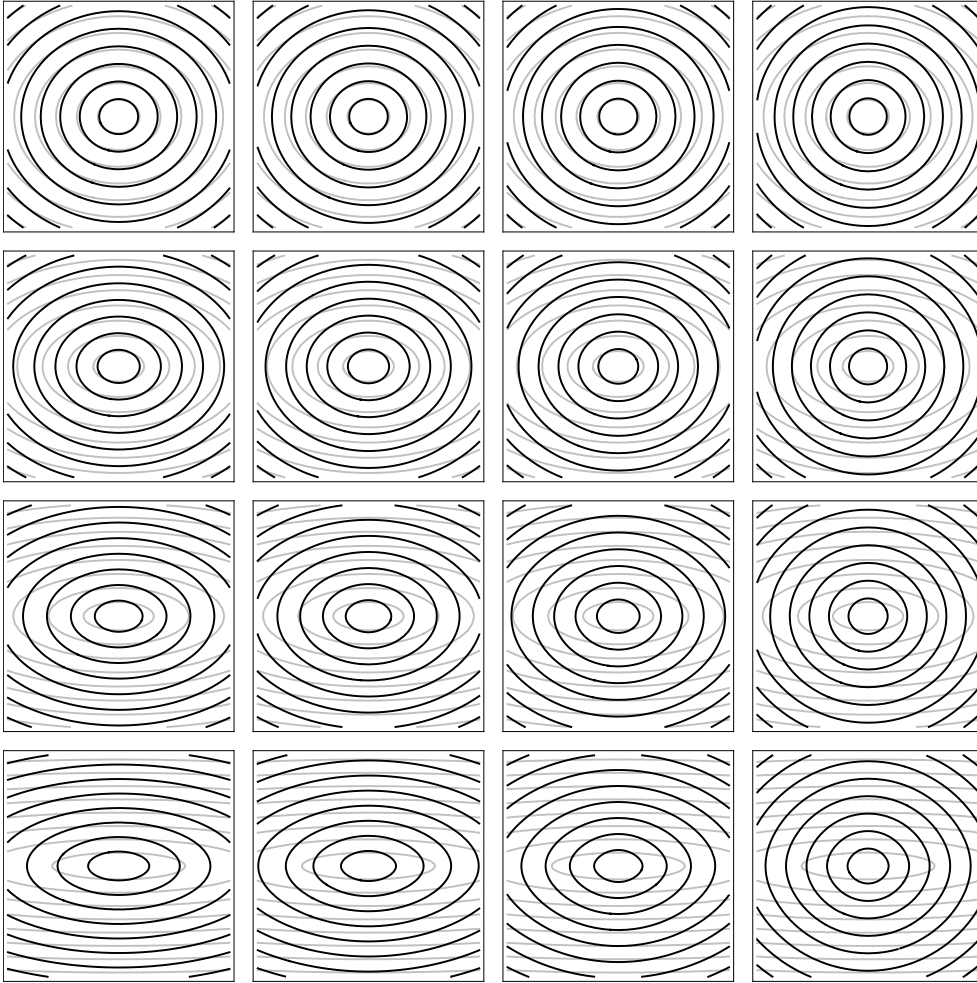


Figure 4.1: Isocontours of the potential  $\psi$  (*black*) and surface mass density  $\kappa$  (*grey*) for an elliptical power law profile lens in physical coordinates  $x_{1,2}$ . For illustration purposes, the contour levels are equally spaced along the diagonals. The slope of the power law profile varies from  $t = 0.25$  (*left*) to  $t = 1.75$  (*right*) in steps of 0.5. The axis ratio varies from  $q = 0.8$  (*top*) to  $q = 0.2$  (*bottom*) in steps of 0.2.

once again recalling the singular isothermal ellipsoid ( $t = 1$ ). Because the complex deflection angle  $\alpha$  from expression (4.15) contains itself a factor of  $e^{i\varphi}$ , it follows that the shear is — as expected — not a vector but instead a polar for the elliptical angle  $\varphi$ . Similar to the potential, the shear is readily calculated once the surface mass density  $\kappa$  and complex deflection angle  $\alpha$  are known.

**Magnification and critical structure.** With shear  $\gamma$  and convergence  $\kappa$  known, it is now possible to find the (inverse) magnification  $\mu^{-1} = (1 - \kappa)^2 - |\gamma|^2$  of the elliptical power law profile lens, which is

$$\mu^{-1} = 1 - 2\kappa + (1 - t) 2\kappa \frac{x_1 \alpha_1 + x_2 \alpha_2}{r^2} - (1 - t)^2 \frac{|\alpha|^2}{r^2}. \quad (4.20)$$

Here  $r$  denotes the physical radius  $r^2 = x_1^2 + x_2^2$ . Using expression (4.20), it is possible to determine the critical lines  $\mu^{-1} = 0$  and corresponding caustics of the lens. Because the resulting equations contain the hypergeometric function, their solutions are found numerically. The critical lines and caustics for a number of settings of the power law slope  $t$  and axis ratio  $q$  are shown in Figure 4.2.

### 4.3 Special cases

In order to check the presented solutions for the deflection (4.15), potential (4.16), shear (4.18), and magnification (4.20), it is useful to compare the expressions to known special cases of the power law slope  $t$ .

**Singular isothermal ellipsoid.** The singular isothermal ellipsoid is a power law profile lens with slope  $t = 1$ . The hypergeometric function can be simplified in this case, yielding the complex deflection angle in physical coordinates

$$\alpha(\mathbf{x}) = \frac{2b}{\sqrt{1 - q^2}} \arctan \left( \frac{\sqrt{1 - q} \sqrt{qx_1 + ix_2}}{\sqrt{1 + q} \sqrt{qx_1 - ix_2}} \right). \quad (4.21)$$

Taking the real and imaginary part and using the sum formula for the inverse tangent reduces the expression to the commonly used form shown in Chapter 3.3. Equivalence of the results for potential  $\psi = x_1 \alpha_1 + x_2 \alpha_2$ , shear  $\gamma = -\kappa z^*/z$ , and magnification  $\mu^{-1} = 1 - 2\kappa$  is trivially checked by setting  $t = 1$  in the respective expressions.

**Point mass.** The limit  $t \rightarrow 2$  takes the power law profile into a point mass lens. The hypergeometric function of the deflection exists in the limit, resulting in the complex deflection angle

$$\alpha(\mathbf{x}) = \frac{b^2 (x_1 + ix_2)}{q r^2}. \quad (4.22)$$

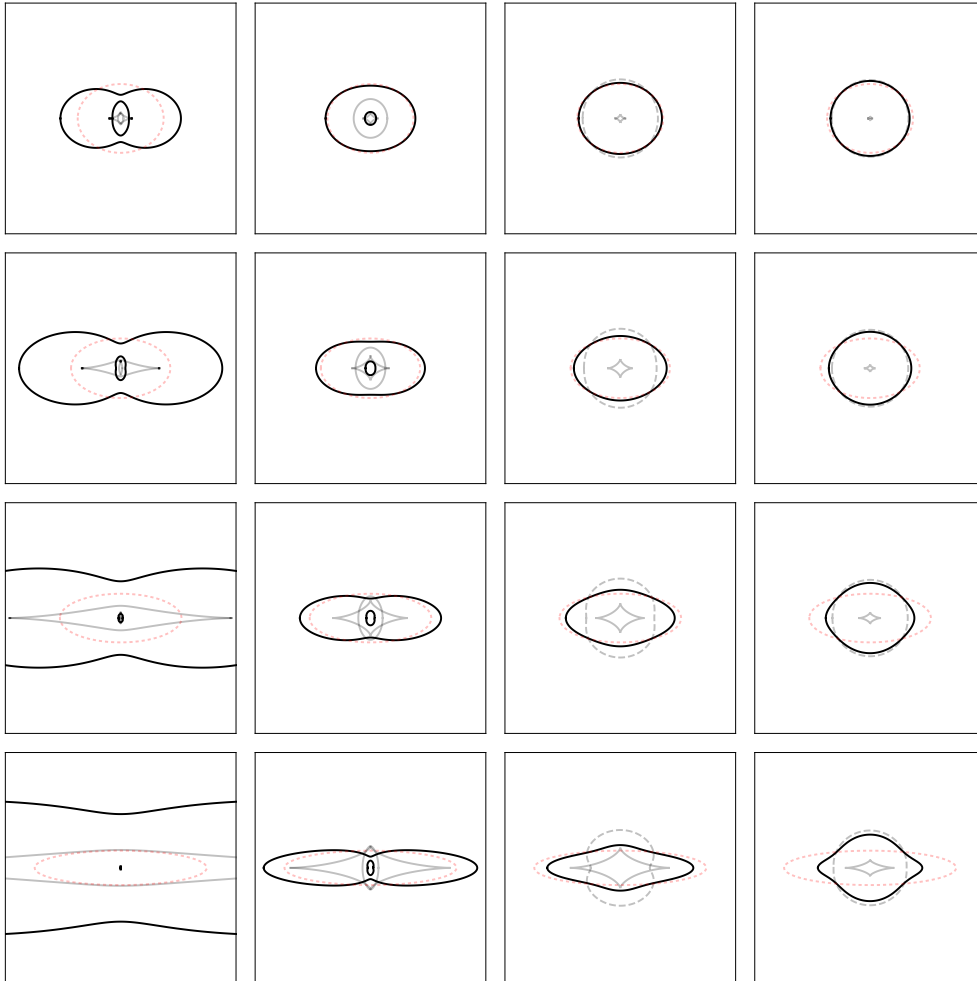


Figure 4.2: The critical lines (*black*) and caustics (*grey*) of the elliptical power law profile lens. In the case of a slope  $t > 1$ , the second pseudo-caustic (*dashed*) is the cut separating regions of single and multiple images. Also shown is an ellipse with semi-minor axis equal to the scale length  $b$  and axis ratio  $q$  (*red, dotted*). For the purpose of illustration,  $b$  decreases as  $\sqrt{q}$ . The slope of the power law profile varies from  $t = 0.25$  (*left*) to  $t = 1.75$  (*right*) in steps of 0.5. The axis ratio varies from  $q = 0.8$  (*top*) to  $q = 0.2$  (*bottom*) in steps of 0.2.

As expected for a point mass, the deflection is always circularly symmetric (note  $r$  instead of  $R$ ), although the axis ratio  $q$  appears in the form of a normalising constant, making the Einstein radius of the lens  $r_E = b q^{-1/2}$ . The potential (4.16) cannot be evaluated in the limit  $t \rightarrow 2$ , but both the shear  $\gamma = -b^2/(qr^2) e^{i2\theta}$  and the magnification  $\mu^{-1} = 1 - b^4/(q^2 r^4)$  are readily calculated and agree with the expressions of Chapter 3.2 for a point mass with the modified Einstein radius.

**Uniform critical mass sheet.** The final case of interest is the uniform critical mass sheet  $\kappa \equiv 1$  in the limit  $t \rightarrow 0$ . In this case, the deflection becomes

$$\alpha(R, \varphi) = \frac{2}{1+q} R e^{i\varphi}, \quad (4.23)$$

which has a clearly unphysical dependency on  $\varphi$ , as the surface mass density  $\kappa$  has circular symmetry. However, the same result (4.23) is obtained if  $\kappa \equiv 1$  is inserted into deflection (4.10) directly. The problematic result is hence a limitation of the formalism for elliptical mass distributions [14], and not of the elliptical power law profile lens.

#### 4.4 Numerical evaluation

The deflection angle (4.15) is at the heart of the elliptical power law profile lens, as the potential (4.16) and shear (4.18) can all be expressed in terms of it. It is thus necessary to find a fast method for evaluating the contained hypergeometric function to make this a useful model for the purposes of numerical simulation and modeling. For this, it is useful to separate the radial and angular parts of the complex deflection angle (4.15), which becomes

$$\alpha(R, \varphi) = \frac{2b}{1+q} \left(\frac{b}{R}\right)^{t-1} \omega(\varphi). \quad (4.24)$$

The angular dependency of  $\alpha$  is contained in the function

$$\omega(\varphi) = e^{i\varphi} {}_2F_1\left(1, \frac{t}{2}; 2 - \frac{t}{2}; -f e^{i2\varphi}\right), \quad (4.25)$$

where  $f = \frac{1-q}{1+q}$  is the second flattening of an ellipse with axis ratio  $q$ . Because the axis ratio is limited to values  $0 < q \leq 1$ , the range of  $f$  is  $0 \leq f < 1$ , and it follows that the hypergeometric function in expression (4.25) has a convergent series representation

$$\omega(\varphi) = \sum_{n=0}^{\infty} \frac{\Gamma(2 - \frac{t}{2}) \Gamma(n + \frac{t}{2})}{\Gamma(\frac{t}{2}) \Gamma(n + 2 - \frac{t}{2})} (-f)^n e^{i(2n+1)\varphi}. \quad (4.26)$$

This, on the other hand, is nothing but a Fourier-type series

$$\omega(\varphi) = \sum_{n=0}^{\infty} a_n e^{i(2n+1)\varphi} \quad (4.27)$$

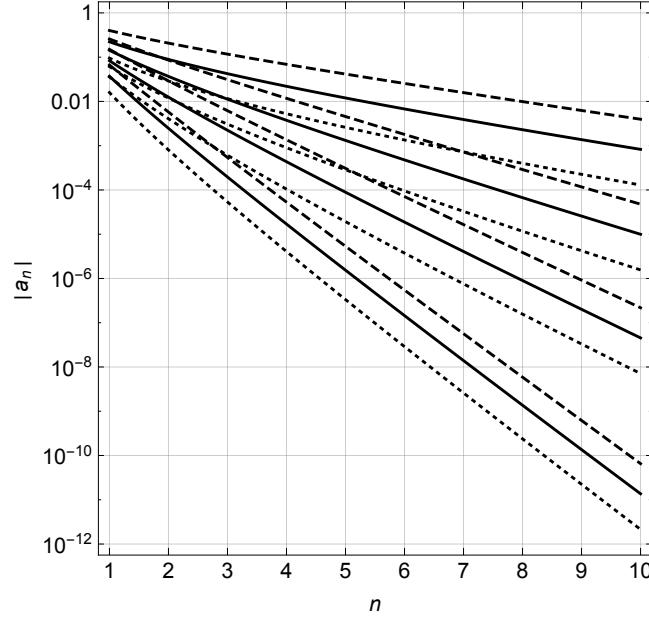


Figure 4.3: Absolute value of the series coefficients  $a_n$  for the elliptical power law profile lens. Shown are graphs for different values  $t = 0.5$  (*dotted*),  $t = 1.0$  (*solid*), and  $t = 1.5$  (*dashed*) of the power law slope and axis ratios from  $q = 0.8$  (*bottom*) to  $q = 0.2$  (*top*) in steps of 0.2.

containing only positive and odd terms  $2n + 1$ , with coefficients given by

$$a_n = \frac{\Gamma(2 - \frac{t}{2}) \Gamma(n + \frac{t}{2})}{\Gamma(\frac{t}{2}) \Gamma(n + 2 - \frac{t}{2})} (-f)^n. \quad (4.28)$$

Since this is a hypergeometric series, the ratio of two subsequent series coefficients is simple,

$$\frac{a_n}{a_{n-1}} = -f \frac{2n - (2 - t)}{2n + (2 - t)}. \quad (4.29)$$

It is clear that the magnitude of the series terms drops off almost geometrically, with an asymptotic rate of  $f$ . This behaviour is shown in Figure 4.3 for various settings of the power law slope  $t$  and axis ratio  $q$ .

**Iterative calculation.** The ratio (4.29) can be used to iteratively calculate the terms of series (4.27). Introducing symbols for the summands as

$$\omega = \sum_{n=0}^{\infty} \Omega_n, \quad (4.30)$$

the  $n$ 'th term  $\Omega_n$  is related to the previous one as

$$\Omega_n = -f \frac{2n - (2 - t)}{2n + (2 - t)} e^{i2\varphi} \Omega_{n-1} . \quad (4.31)$$

This expression reduces the calculation of the deflection to (complex) addition and multiplication. Because the computation is iterative, it can be continued easily until the desired precision or accuracy in the deflection is reached.

Instead of the numerical scheme given by equations (4.30) and (4.31), it can be advantageous to forego the use of complex numbers, particularly in computer implementations. Just as the two-dimensional deflection angle  $\alpha$  is given by the real and imaginary components of the complex deflection angle  $\alpha$ , the complex angular dependency  $\omega$  can be expressed as a two-dimensional vector  $\omega$  in the real formulation. Expanding the exponential in Fourier series (4.27) into its real and imaginary parts, the components of  $\omega$  can be written as the individual series

$$\begin{aligned} \omega_1(\varphi) &= \sum_{n=0}^{\infty} a_n \cos((2n + 1)\varphi) , \\ \omega_2(\varphi) &= \sum_{n=0}^{\infty} a_n \sin((2n + 1)\varphi) . \end{aligned} \quad (4.32)$$

Just as in the complex case, the real components of the deflection angle can be calculated iteratively. Writing

$$\begin{aligned} \omega_1 &= \sum_{n=0}^{\infty} \Omega_{n,1} , \\ \omega_2 &= \sum_{n=0}^{\infty} \Omega_{n,2} , \end{aligned} \quad (4.33)$$

relations for the respective  $n$ 'th terms can be found by understanding the complex product  $e^{i2\varphi} \Omega_{n-1}$  in expression (4.31) as the matrix multiplication

$$\Omega_n = -f \frac{2n - (2 - t)}{2n + (2 - t)} \mathbf{R}_{2\varphi} \Omega_{n-1} \quad (4.34)$$

in two dimensions, where  $\mathbf{R}_{2\varphi}$  is the rotation matrix. In components, this is

$$\begin{aligned} \Omega_{n,1} &= -f \frac{2n - (2 - t)}{2n + (2 - t)} (\cos(2\varphi) \Omega_{n-1,1} - \sin(2\varphi) \Omega_{n-1,2}) , \\ \Omega_{n,2} &= -f \frac{2n - (2 - t)}{2n + (2 - t)} (\sin(2\varphi) \Omega_{n-1,1} + \cos(2\varphi) \Omega_{n-1,2}) . \end{aligned} \quad (4.35)$$

This prescription can make evaluation of the deflection suitably fast to use the elliptical power law profile lens for ray tracing in lens reconstruction algorithms such as the one presented in the following, where a large number of calculations is performed.

**Practical parameterisation.** As in the analogous case of the singular isothermal ellipsoid (Chapter 3.3), practical use of the elliptical power law lens benefits from a slightly different definition of the scale length. By construction, the dimensionless mass contained in the region bounded by the elliptical radius  $R = b$  is the same as (3.23) for the singular isothermal ellipsoid,<sup>2</sup>

$$m = \frac{2\pi}{q} \int_0^b dR R \kappa(R) = \frac{\pi b^2}{q}. \quad (4.36)$$

As before, the scale length  $b$  can be transformed to a different parameter

$$b \mapsto b_{\text{SIS}} = \frac{b}{\sqrt{q}} \quad (4.37)$$

for practical applications, so that the mass  $m$  depends on the parameter  $b_{\text{SIS}}$  alone. The change of parameterisation reduces possible correlations between parameters of the lens, as the new scale length  $b_{\text{SIS}}$  is only weakly dependent on axis ratio  $q$  and power law slope  $t$  in lens reconstructions. This is clearly visible in the results of Chapter 9.

---

<sup>2</sup>The scale length  $b$  is however *not the Einstein radius* of the elliptical power law profile lens, as Figure 4.2 clearly shows.

## 5 Forward lens reconstruction

### 5.1 Reconstruction with extended images

Any lens reconstruction constrains the deflecting mass distribution through the requirement that multiply-imaged points must trace back to the same source plane location, and through the relative magnifications of the individual images. When the observation contains multiple extended images of the background sources, the lens is not only constrained by data at discrete points, but over continuous regions. Observations of gravitational lensing with large, extended sources such as those shown in Figure 5.1 therefore contain a wealth of information that would not be accessible for unresolved sources. On the other hand, the increased precision with which the lens can be constrained also makes it necessary to find new tools for the reconstruction. It is clear from the beginning that the task is made more difficult by the abundance of information within a single image, but that there are great scientific rewards for any method that reliably reconstructs these observations.

**The forward and inverse problem.** The reconstruction of resolved gravitational lenses is commonly approached in one of two different but related ways [58]: as the *forward problem* of creating a model of the lens system — lenses and sources — that approximates the observed image, or as the *inverse problem* of finding a lens model which deconstructs the observation into a self-consistent and physically viable image of the source. Many successful applications have been published for both the forward [5, 11, 70, 77] and the inverse method [29, 52, 71, 100, 110, 113, 114]. In practice, the forward and inverse method are generally dissimilar, and each has its own particular set of strengths and weaknesses, which are summarised here. On the other hand, in the last section of this chapter it will be briefly shown how both methods are fundamentally related.

**Lens reconstruction as an inverse problem.** In lens reconstruction, the inverse problem refers to the process of “de-lensing” a given observation into a surface brightness distribution on the source plane. When lensed, this source must then reproduce once again the observed image. Such a *lens inversion* is generally made possible by the linear nature of the surface brightness mapping from source to image plane. If this process is combined with some sort of regularisation for the

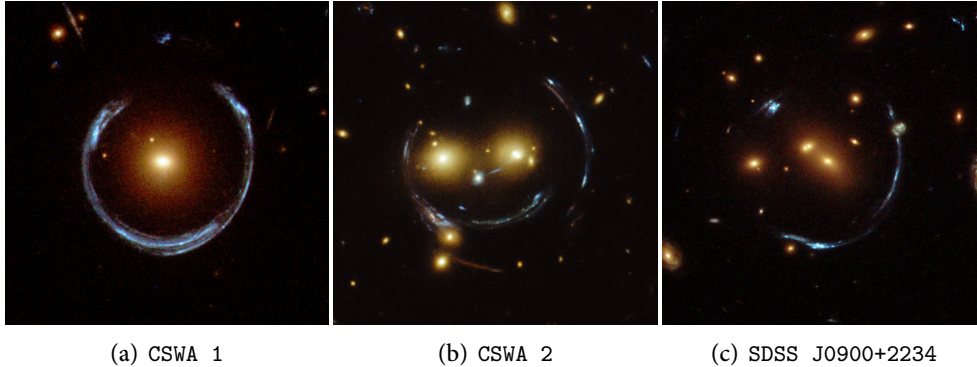


Figure 5.1: Examples of observations of strong gravitational lensing with resolved sources. The large arcs contain information to constrain the gravitational lenses producing these images. Objects with CSWA identifier are listed in the *Cambridge and Sloan Survey of Wide Arcs in the Sky* (CASSOWARY) catalogue of large strong lenses, which is available online [20] and contains many of these spectacular lenses.

Image credit: (a) ESA/Hubble & NASA, (b) NASA & ESA, (c) ESA/Hubble & NASA,

recovered source (i.e. requiring its values to adhere to certain physically motivated conditions), the inverse method can be used for lens reconstruction [52, 113]. The lens is constrained by optimisation of a merit function that weighs, for the given lens model, the quality of the reconstructed observation against the regularity of the source. Because the inversion is a linear operation, the procedure corresponds to the inversion of a matrix which maps the recovered source to the image pixels of the observation [114].

In practise, many different flavours of the inverse method exist, differentiated by their choice of source and regularisation. Examples include pixelated sources with a maximum entropy constraint [113] or linear regularisation [114], as well as adaptively refined source grids with implicit [29, 71] or explicit regularisation [71]. Other methods extend these approaches to a fully Bayesian analysis where the regularisation itself is a nuisance parameter [100, 110].

The large number of existing variants indicates that one of the biggest strengths of the inverse method — the great flexibility in the model — is at the same time one of its principal challenges. Just as there are no good universal source models that encompass all possible galaxy morphologies, it is similarly difficult to find a reasonable universal source regularisation. There is also a strong interdependence between the regularisation and the source representation, and possible systematic effects need to be carefully taken into account [101]. Similarly, in the Bayesian methods that marginalise over the parameters of the regularisation, it is necessary to find reasonable prior probabilities for these parameters, and make sure that the choice does not influence the results [100]. Furthermore, it can be difficult to

interpret the reconstructed sources, which might contain artefacts due to the noise in the observation. Sometimes, a final step of the analysis includes the fitting of an analytical source profile to the results. In this case, the desired results could have been found with the forward reconstruction straight away and in a more robust fashion.

**Lens reconstruction as a forward problem.** The *forward lens reconstruction* of observations attempts to create a model of a gravitational lens system, including lensed sources, that can reproduce an observation as well as possible. This implies that the method goes through the usual steps of a fitting procedure.

1. Define a model of the physical system, i.e. lenses and sources.
2. Simulate the model to obtain an expected image of the observation.
3. Compare the expectation to the data.
4. Change the model according to the result.

The strengths of the forward method are its simplicity and the great amount of control over the model. Because the individual lens and source components are usually described by parametric models with a physical basis, results are robust and relatively easy to interpret. A further advantage is the direct control over all aspects of the model, which makes forward reconstruction the method of choice whenever a specific model is to be tested against observations. Despite its basic simplicity, the forward method presents a number of challenges. A practical issue is that of computational complexity, as the reconstruction of a given lens system requires a large number of simulations for different parameter settings, each of which is a complex computational task. Fortunately, there are ways to mitigate the numerical burden, which are presented in Chapter 6. A more fundamental issue is that of insufficient source models. To date, there are no models that can realistically reproduce galaxies with complex visible substructure, and in light of the morphological variations that are observed in nature, it is doubtful that there will ever be sufficient parametric models. However, Chapter 7 will show that the forward method for lens reconstruction works well with simple parametric source components even if the observation is complex, and that it allows for a robust estimation of the parameters of these source models.

## 5.2 Definition of a model

The model of a gravitational lens is, at least for the purpose of reconstruction, entirely determined by its predicted surface brightness distribution

$$f(\mathbf{x}) = f_F(\mathbf{x}) + f_S(\mathbf{y}(\mathbf{x})), \quad (5.1)$$

where  $f_F(\mathbf{x})$  is the foreground surface brightness distribution on the image plane, which is undeflected, and  $f_S(\mathbf{y})$  is the background surface brightness distribution on the source plane, which is deflected according to the lens equation for  $\mathbf{y}(\mathbf{x})$ . It follows that there are three parts to the definition of a model for the lens system:

- the deflection angle  $\boldsymbol{\alpha}(\mathbf{x})$  necessary to find source plane position  $\mathbf{y}(\mathbf{x})$ ,
- the foreground surface brightness  $f_F(\mathbf{x})$ , and
- the background surface brightness  $f_S(\mathbf{y})$ .

These are the fundamental constituents of a model for any two-plane lens system.<sup>1</sup>

**Lens components.** The forward method is most successful in the simulation and reconstruction of galaxy-scale lenses that can be reasonably well described by a composite model of parametric lenses. Such a model consists of a number  $N_L$  of lens components, for example those presented in Chapter 3. Since gravitational lensing assumes linearity in the deflection from the start, the total deflection angle on the image plane is the sum

$$\boldsymbol{\alpha}(\mathbf{x}) = \sum_{i=1}^{N_L} \boldsymbol{\alpha}_i(\mathbf{x}) \quad (5.2)$$

of deflections  $\boldsymbol{\alpha}_i$  contributed by the individual components. In theory, there is no limit to the number of components that can be combined in this way, and most reconstruction use one or more lens components together with an external shear.

**Nonparametric lens models.** It is also possible to model the lens using the pixels of a discretised mass distribution  $\kappa$  or deflection potential  $\psi$ . Such *nonparametric* models<sup>2</sup> are well established in cluster reconstructions and lens inversion, but have not been widely adopted for the forward method. This might be in part due to the increased complexity of the reconstruction. It is often not feasible to reconstruct the large number of (non)parameters — pixels — of the lens, and at the same time the source model, in a full simulation. Furthermore, a nonparametric lens ideally requires a nonparametric source, in order to not limit the reconstruction by insufficient detail in the source model. However, it is shown in Section 5.7 that a discretised source model naturally leads to the inverse method, and is therefore rarely useful in a forward reconstruction scenario.

<sup>1</sup>When more lensing planes are to be modelled, the situation remains unchanged. Each of the planes  $i = 0, 1, \dots$  requires specification of its surface brightness  $f_i(\mathbf{x}_i)$  and deflection field  $\boldsymbol{\alpha}_i(\mathbf{x}_i)$ , where the deflection  $\boldsymbol{\alpha}_0$  is fixed to zero for the image plane.

<sup>2</sup>These models contain of course a large number of parameters in the form of pixels and would more realistically be called *ultraparametric* models.

**Surface brightness distributions.** A given source model contains a number  $N_F$  and  $N_S$  of foreground and background components, with the respective surface brightness distributions

$$f_F(\mathbf{x}) = \sum_{i=1}^{N_F} f_{Fi}(\mathbf{x}), \quad (5.3)$$

$$f_S(\mathbf{y}) = \sum_{i=1}^{N_S} f_{Si}(\mathbf{y}). \quad (5.4)$$

Each component  $f_{Fi}(\mathbf{x})$ ,  $f_{Si}(\mathbf{y})$  is given by a parametric source model such as those presented in Section 5.3. Just as in the case of galaxy reconstructions without lensing, sources usually require a moderate number of components [75, 76], and it will be shown in the applications of Chapter 9 how the number of sources might influence the lens reconstruction.

### 5.3 Source models

As mentioned before, the forward method usually works with parametric sources. The reason is that a nonparametric source model such as a discretised surface brightness function quickly turns the forward method into an inverse method, which in practice requires a very different technical treatment. This is explicitly shown in Section 5.7. Hence only parametric sources will be considered in what follows. Nevertheless, a great amount of freedom in the possible models can be achieved with expansions in basis sets, which are treated below.

**Parametric profiles.** The most common model for sources such as galaxies is a parametric profile  $S(R)$ , where  $R$  is some measure of distance from the centre of the object. Such models assume a unrealistically high degree of symmetry, but are on the other hand easy to define and implement. Profiles used in the components of galaxy images are normally assumed to have elliptical symmetry [75, 76], and hence  $R$  is the *elliptical radius* (cf. Chapter 4.1)

$$R(\mathbf{x}') = \sqrt{q^2 x_1'^2 + x_2'^2} \quad (5.5)$$

of a source with axis ratio  $q$ . The coordinate system  $(x_1', x_2')$  of the source can be rotated by the *position angle*  $\theta_S$  with respect to the coordinate system  $(x_1, x_2)$  of the observation. Assuming that its centre is located at  $\mathbf{x}_S$ , the surface brightness distribution of an elliptical source with profile  $S(R)$  is

$$f_S(\mathbf{x}) = S(R(\text{Rot}_{(-\theta_S)}(\mathbf{x} - \mathbf{x}_S))). \quad (5.6)$$

where  $\text{Rot}_{(-\theta_S)}$  is the rotation matrix performing the (opposite) coordinate system rotation for position angle  $\theta_S$ . The resulting isophotes of such a source, drawn schematically in Figure 5.2, are ellipses with semi-major axis  $R/q$ , semi-minor axis  $R$ , and orientation  $\theta_S$  with respect to the  $x_1$ -axis of the world coordinates.

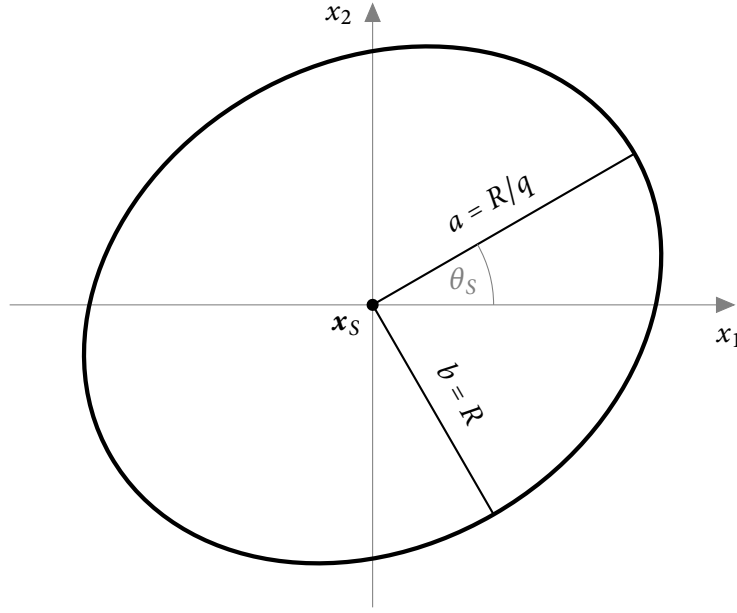


Figure 5.2: Example of an isophote of an elliptical source profile with axis ratio  $q$ . The ellipse is rotated by the position angle  $\theta_s$  with respect to the coordinate system. The elliptical radius  $R$  corresponds to the semi-minor axis  $b$  of the ellipse, while the semi-major axis  $a$  is scaled by the inverse of  $q$ .

**The Sérsic profile.** The Sérsic  $R^{1/n}$  law is the prototypical profile for parametric sources [42, 90, 91]. It is given by the exponential

$$S(R) = S_0 \exp \left\{ -b \left( \frac{R}{R_{\text{eff}}} \right)^{1/n} \right\} \quad (5.7)$$

with a  $R^{1/n}$  dependency, and the inverse power  $n > 0$  is called the Sérsic index of the profile. The scale length  $R_{\text{eff}}$  is chosen as the half-light radius of the profile, so that the luminosity

$$L_{\text{eff}} = \frac{2\pi}{q} \int_0^{R_{\text{eff}}} dR R S(R) = \frac{2\pi}{q} R_{\text{eff}}^2 S_0 \frac{n}{b^{2n}} (\Gamma(2n) - \Gamma(2n, b)) \quad (5.8)$$

within radius  $R_{\text{eff}}$  is half the total luminosity

$$L_{\infty} = \frac{2\pi}{q} \int_0^{\infty} dR R S(R) = \frac{2\pi}{q} R_{\text{eff}}^2 S_0 \frac{n}{b^{2n}} \Gamma(2n), \quad (5.9)$$

where  $\Gamma(z)$  and  $\Gamma(a, z)$  denote the gamma function and the incomplete gamma function, respectively, and the extra factor of  $q$  from the elliptical profile was taken into account. The constant  $b$  ensures the relation  $2L_{\text{eff}} = L_{\infty}$  and is therefore

implicitly defined by

$$\Gamma(2n, b) = \frac{1}{2} \Gamma(2n) . \quad (5.10)$$

Instead of solving this equation numerically for each value of  $n$  — which can be quite often if  $n$  is a parameter of the reconstruction — a suitable approximation can be used [21, 24, 25], for example

$$b \approx 1.9992n - 0.3271 \quad (5.11)$$

in the range  $0.5 \leq n \lesssim 8$ . Finally, the normalisation  $S_0$  of the profile is related to the total luminosity via

$$S_0 = \frac{L_\infty}{\pi R_{\text{eff}}^2/q} \frac{b^{2n}}{\Gamma(2n+1)} . \quad (5.12)$$

The total luminosity is usually a parameter of the source and given in terms of its magnitude

$$\text{mag}_S = \text{mag}_{\text{ref}} - 2.5 \log_{10}(L_\infty) \quad (5.13)$$

relative to some reference system. With this, the profile is now fully determined by the seven parameters for position  $x_1, x_2$ , effective radius  $R_{\text{eff}}$ , Sérsic index  $n$ , magnitude  $\text{mag}_S$ , axis ratio  $q$  and position angle  $\theta$ .

The Sérsic profile is a versatile model, and it contains many of the classical galaxy profiles as special cases, such as Gaussian profiles ( $n = 1/2$ ), exponential profiles ( $t = 1$ ) and de Vaucouleurs [118] profiles ( $n = 4$ ). For this reason, Sérsic profiles are the standard components in the parametric decomposition of galaxy images [75, 76], and have a long and successful history in lens reconstruction.

**Sources from sets of basis functions.** Surface brightness functions, are maps from the real plane  $\mathbb{R}^2$  to the real numbers  $\mathbb{R}$ , and as such, they can be decomposed into a suitable set of basis functions. These are families of functions  $U_n(\mathbf{x})$  for which any given function  $f(\mathbf{x})$  can be written as the linear combination

$$f(\mathbf{x}) = \sum_n a_n U_n(\mathbf{x}) , \quad (5.14)$$

where the numbers  $a_n$  are the coefficients of the expansion. These coefficients are found by projecting the function  $f$  onto the basis functions  $U_n$ ,

$$a_n = \int d^2x w(\mathbf{x}) f(\mathbf{x}) U_n^*(\mathbf{x}) , \quad (5.15)$$

where  $w$  is a weighting function and  $U_n^*$  is the complex conjugate.<sup>3</sup> If the basis is orthonormal, then the projection of  $U_m$  onto  $U_n$  vanishes unless  $m = n$ ,

$$\int d^2x w(\mathbf{x}) U_m(\mathbf{x}) U_n^*(\mathbf{x}) = \delta_{mn} , \quad (5.16)$$

<sup>3</sup>The basis functions can be complex even though the functions  $f$  are not.

in which case the individual coefficients  $a_n$  are said to be independent.

If the function  $f(\boldsymbol{x})$  is a surface brightness distribution, a limited number of terms from expansion (5.14) can be used as the approximation of an arbitrarily detailed  $f$  in lens reconstructions. In this case, the set of coefficients  $a_n$  can be understood as the parameters of a *semi-parametric* source model. The similarity of such a model to a realistic source depends highly on the set of basis functions. The particular task of reproducing galaxies from astronomical images resulted in the creation of *Shapelet* basis functions, which form a complete and orthonormal set of functions suitable for the extraction and manipulation of galaxy images [82, 83]. Shapelets allow the recreation of realistic sources with relatively few parameters [62], and computer codes are available for the extraction of Shapelet coefficients from existing observations [61].

**Sky components.** Observations often contain a diffuse overall distribution of light, the so-called *sky background*, which must be included in the reconstruction. The simplest model for a sky component is a flat surface brightness distribution, which is either a constant value or a fixed gradient with respect to the  $x_{1,2}$  axes. Adding such a sky component as a free component to the model is a good idea even when the diffuse background has been subtracted in a preprocessing step. The distinction between sky and signal is difficult, and over- or underestimation of the subtracted light can significantly influence the results of the reconstruction.

**Units of the surface brightness.** To prevent the explicit conversion of units, it will always be assumed that the surface brightness of a source is given in suitable units for a direct comparison with data, e.g. counts per second. This can be done by specifying the magnitude of simulated sources relative to the zeropoint of the instrument. By definition, a source with magnitude equal to the zeropoint  $\text{mag}_{\text{zp}}$  has a detection rate of one count per second. For the same instrument, a source with magnitude  $\text{mag}_S$  has an observed count rate of

$$\text{mag}_S = -2.5 \log_{10}(\text{total counts/second}) + \text{mag}_{\text{zp}}, \quad (5.17)$$

and the luminosity of a source in units of the instrument is

$$\text{total counts/second} = 10^{-0.4(\text{mag}_S - \text{mag}_{\text{zp}})}. \quad (5.18)$$

By specifying only the relative magnitude  $\Delta\text{mag} = \text{mag}_S - \text{mag}_{\text{zp}}$  of sources, the reconstruction can remain entirely ignorant of instrument details.

## 5.4 Simulation of the lens system

Once the surface brightness and deflection of the lens system are specified, it is possible to simulate the expected image under the given model. The predicted

flux  $m_i$  of the model registered at pixel  $i$  of the detector is given by the integral

$$m_i = \int_{A_i} d^2x f(\mathbf{x}) = \int_{A_i} d^2x \{f_F(\mathbf{x}) + f_S(\mathbf{y}(\mathbf{x}))\} \quad (5.19)$$

of the combined foreground and background surface brightness  $f_F(\mathbf{x})$  and  $f_S(\mathbf{y})$  over the pixel area  $A_i$ . The index  $i$  is a two-dimensional multi-index  $(i_1, i_2)$  of integers that identifies a location on the pixel grid, and can be manipulated as any integer vector. While the calculation of the expected pixel values for a model is easy to write down in the form (5.19), the evaluation of such an integral is not as easy to perform in practice, and overcoming the computational burden of this integration is one of the main points of Chapter 6.

**Point-spread function.** Image degradation due to the instrument and ambient conditions can be taken into account using a point-spread function (PSF). The PSF is a convolution kernel  $p$  that represents the observed image of a point-like source at the origin, so that the apparent surface brightness  $f^*(\mathbf{x})$  of a physical distribution  $f$  can be expressed as

$$f^*(\mathbf{x}) = \int d^2x' p(\mathbf{x} - \mathbf{x}') f(\mathbf{x}') = \int d^2r p(-\mathbf{r}) f(\mathbf{x} + \mathbf{r}). \quad (5.20)$$

The PSF of an observation is usually provided in one of two ways: Either as the parameters of an idealised analytical profile, e.g. a Gaussian, or in discretised form as a zero-centred  $(2w_1 + 1) \times (2w_2 + 1)$  array of values<sup>4</sup>

$$p_i = \begin{bmatrix} p_{w_1, -w_2} & \cdots & p_{w_1, 0} & \cdots & p_{w_1, w_2} \\ \vdots & & \vdots & & \vdots \\ p_{0, -w_2} & \cdots & p_{0, 0} & \cdots & p_{0, w_2} \\ \vdots & & \vdots & & \vdots \\ p_{-w_1, -w_2} & \cdots & p_{-w_1, 0} & \cdots & p_{-w_1, w_2} \end{bmatrix}.$$

Instead of using the convolved surface brightness (5.20) in the integration of the pixel flux (5.19), it is common (and in the second case necessary) to first calculate the pixel values  $m_i$  normally and then apply the PSF by discrete convolution

$$m_i^* = \sum_{j=-w}^w p_{-j} m_{i+j}, \quad (5.21)$$

where the summation is carried out independently for each component of the multi-index.

To prevent separate notation in calculations with and without PSF, the flux will in the following always be denoted  $m_i$ , even when the result was convolved with the PSF as in equation (5.21). This is possible because all further calculations only depend on the final model image  $m_i$ , and not on details of its calculation. It should be clear that  $m_i$  has to be replaced with  $m_i^*$  when the image degradation due to a PSF is to be considered.

<sup>4</sup>Here  $i = (i_1, i_2) \in \mathbb{N} \times \mathbb{N}$  is still a multi-index.

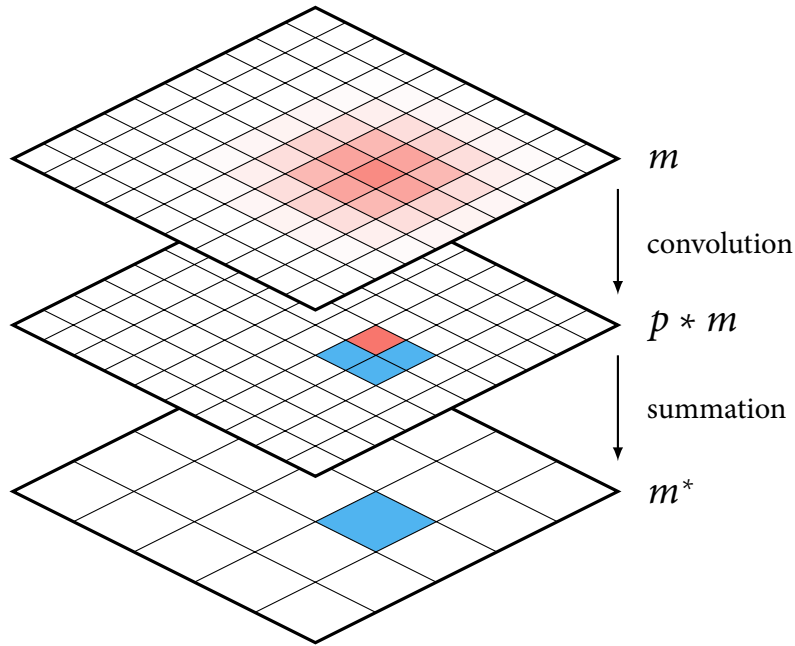


Figure 5.3: Image creation for a  $5 \times 5$  pixel image with a PSF at twice the resolution. The integrated flux is calculated for each subpixel and the PSF is applied by discrete convolution (*red*). The subpixels for an image pixel are then added (*blue*) to give the expected image at data resolution.

**Subsampled PSFs.** The PSF for an instrument can be more highly resolved than the observations, for example when discretising an analytical or empirical profile. In this case, non-degraded pixel fluxes  $m_i$  have to be calculated on a subpixel grid at PSF resolution, so that the discrete convolution can be executed. Assuming that the subpixel grid evenly divides the pixel grid, the flux in all subpixels of pixel  $i$  is added to give the flux  $m_i^*$  after image degradation. This process is illustrated in Figure 5.3 for a twice-subsampled PSF.

## 5.5 Model evaluation

In order to evaluate how closely the chosen model resembles the observed lens system, it is necessary to compare the simulated pixel values  $m_i$  and the actual data  $d_i$  of the observation. To perform such a comparison, a scale must be found with which the difference  $d_i - m_i$  can be weighed. Given that the observation, i.e. the detection of incoming photons by the instrument, in itself is a random process, such a scale is provided as the covariance matrix  $\Sigma$  of the pixel values, which intuitively expresses how much any single measurement of values can be trusted. Here it is assumed here that the covariance matrix  $\Sigma$  is provided with the observation. This is usually not the case, and Chapter 6.3 contains a recipe for

generating  $\Sigma$  from the data.

**Image likelihood.** The random nature of observations turns the comparison of model prediction and available data into a matter of probabilities. To see that the simulated values  $m_i$  are suitable for such a statistical comparison, one should recall that the theoretical flux is precisely defined as the expectation value

$$E[d_i] = m_i \quad (\text{assuming the given model is the true one}) \quad (5.22)$$

of the values  $d_i$  measured in an actual observation. Combining the two sets of model and data values  $m_i$  and  $d_i$  into the respective  $n$ -vectors  $m = (m_1, \dots, m_n)$  and  $d = (d_1, \dots, d_n)$ , the difference  $d - m$  and the  $n \times n$  covariance matrix  $\Sigma$  can be used to define the *image likelihood*

$$P(d | m) = (2\pi \det \Sigma)^{-n/2} \exp \left\{ -\frac{1}{2} (d - m)^T \Sigma^{-1} (d - m) \right\} \quad (5.23)$$

of observing data  $d$  assuming a model that predicts  $m$  as the mean pixel values. Using a Gaussian likelihood such as (5.23) implicitly assumes the central limit theorem, by which the real distribution of the data becomes approximately normal for large photon counts. In practice, this assumption should always hold in lens reconstruction due to the contribution of flux from foreground sources (including the sky) and long exposures, even if the signal of the lensed images itself is weak.

**Quality of the reconstruction.** In practical applications, it is often desirable to find a general indicator for quality of a reconstruction. This is usually achieved with the  $\chi^2$  summary statistic. Understanding the vector  $d$  of data values as a multivariate random variable with mean given by the vector  $m$  of model values, and using the covariance matrix  $\Sigma$ , the  $\chi^2$  value is defined as the vector–matrix–vector contraction

$$\chi^2 = (d - m)^T \Sigma^{-1} (d - m). \quad (5.24)$$

Intuitively, this uses the covariance matrix to weigh the difference of observation and model in each pixel. Where model and data agree, these differences should on average be equal to one standard deviation. Consequently, given that the image contains  $n$  pixels, a value  $\chi^2 \approx n$  indicates a successful reconstruction. This holds as long as the covariance matrix is non-degenerate. The number  $n$  is known as the *degrees of freedom* of the reconstruction. Realistically, every model parameter reduces the degrees of freedom, so that

$$(\text{degrees of freedom}) = n - (\text{number of parameters}). \quad (5.25)$$

However, because the number of pixels is usually vastly greater than the number of parameters, this distinction is of little practical significance. It should be noted that the image likelihood (5.23) can be written in terms of  $\chi^2$  as

$$P(d | m) = (2\pi \det \Sigma)^{-n/2} \exp \left\{ -\frac{1}{2} \chi^2 \right\}, \quad (5.26)$$

and the image quality is thus a natural byproduct of the likelihood evaluation.

## 5.6 Parameter estimation

Once image likelihood (5.23) is determined, it becomes possible to explore the parameter space of the assumed model. The set of parameters will be denoted collectively as  $\xi = \{\xi_1, \xi_2, \dots\}$ . Through integral (5.19), the predicted pixel values  $m$  of the model are implicitly functions  $m(\xi)$  of the parameter values, since both the surface brightness  $f$  and the deflection angle  $\alpha$  depend on them. It is therefore possible to identify image likelihood (5.23) with the likelihood

$$P(d | \xi) \equiv P(d | m(\xi)) \quad (5.27)$$

of observing data  $d$  for the given parameters  $\xi$  of the chosen model. Through Bayes' theorem, the parameter likelihood can be transformed into the *posterior probability*

$$P(\xi | d) = \frac{P(d | \xi) P(\xi)}{P(d)} \quad (5.28)$$

of the parameter values  $\xi$  after observation of the data  $d$ , where  $P(\xi)$  is the *prior probability* of the parameters values before the data was available. Such a prior could e.g. be a normal distribution for the lens position around the centroid of the observed foreground light distribution, or an empirical distribution for the profile given to background sources which was taken from the literature. It is generally important to pick *non-informative* priors that do not unduly influence the posterior distribution of the parameters, so that the results are determined largely by the information from the reconstruction.

**Evidence.** The remaining term  $P(d)$  in posterior (5.28) is called the *evidence* of the assumed model. It is the marginal distribution

$$P(d) = \int d\xi_1 d\xi_2 \dots P(d | \xi) P(\xi) \quad (5.29)$$

of likelihood and prior over the whole parameter space, giving the normalising constant in the definition of the posterior probability. For any given model of lenses and sources, the evidence is a global, parameter-independent value that quantifies, as the name suggests, the confidence in the model to be responsible for the observed data. It can be used to objectively compare different models that reconstruct the same observation [47]. Because the evidence is a constant, many algorithms that sample posterior (5.28) do not require its knowledge. This is true in particular for the class of Markov chain Monte Carlo (MCMC) samplers, which today are the prevalent method of exploring posterior distributions.

**Parameter inference.** The information of the observation about the assumed model is contained in posterior (5.28), which describes the distribution of likely parameter values within the parameter space of the model. Quantities of interest for the individual parameters, such as mean values and confidence intervals, can all be extracted from it in the usual ways. It must be noted that the posteriors in lens reconstructions are generally complicated. The principal cause is the high number of dimensions for any sufficiently developed model of the lens system, which increases the complexity of sampling enormously. Other reasons that arise naturally in lens reconstructions are more subtle. When an observation contains multiple images of one source, the lens model might be unable to reproduce all of the images equally well at the same time. Instead, different sets of parameter values might result in good reconstructions of different images, and the result is a multi-modal posterior distribution of the parameters. The posterior also features many intrinsic degeneracies between parameter values. For example, background source parameters such as the position and magnitude are only seen through the effects of lensing, and thus depend crucially on the deflection and magnification of the lens. It is clear that the exploration of the parameter space is not an easy task, and any practical implementation must be prepared to handle complications such as those mentioned here.

## 5.7 Relation to the inverse method

In practice, the forward and inverse methods of lens reconstruction are not very similar. Applications of forward reconstruction are mainly concerned with fast image synthesis and the simulation of physical models, while lens inversion is usually focussed on quick inversion of large matrices and optimisation of many parameters. However, in a theoretical framework, there is a clear correspondence between the forward and inverse methods, which is briefly shown below.

**Forward to inverse method.** Instead of the source models from Section 5.3 that follow some specific profile or expansion, a generic discretised source is used. The surface brightness function of such a source can be written in the general form

$$f_s(\mathbf{y}) = \sum_{j=1}^m s_j \chi_j(\mathbf{y}), \quad (5.30)$$

where  $m$  is the number of source grid cells, the numbers  $s_j \in \{s_1, \dots, s_m\}$  are the discrete surface brightness values, and the functions  $\chi_j$  are the indicator functions (also known as characteristic functions) of the source grid cells,

$$\chi_j(\mathbf{y}) = \begin{cases} 1 & \text{if } \mathbf{y} \text{ is in source grid cell } j, \\ 0 & \text{otherwise.} \end{cases} \quad (5.31)$$

If such a discrete source is inserted into integral (5.19) for the expected flux in a pixel, the result is

$$m_i = \sum_{j=1}^m s_j \int_{A_i} d^2x \chi_j(\mathbf{y}(\mathbf{x})) . \quad (5.32)$$

The sum in this expression can be understood as a matrix–vector multiplication

$$m_i = \sum_{j=1}^m L_{ij} s_j \quad (5.33)$$

of the source vector  $s = (s_1, \dots, s_m)$  and a lens matrix  $L$  with coefficients

$$L_{ij} = \int_{A_i} d^2x \chi_j(\mathbf{y}(\mathbf{x})) . \quad (5.34)$$

Defining the image vector  $m = (m_1, \dots, m_n)$ , the mapping from source values to image pixels can be written as the matrix product

$$m = L s . \quad (5.35)$$

This is precisely the usual formalism of semi-linear lens inversion [101, 114]. Source parameters of the forward method have become the pixel values of a discretised source plane. In order to constrain the lens, the discretised source cannot be left entirely free, and the required prior distribution on the possible values of the source grid cells corresponds to the regularisation normally used in lens inversion methods.

**Inverse to forward method.** An intuitive correspondence between the inverse and forward method arises when a delta function prior

$$P(s_j) = \delta(s_j - v_j) \quad (5.36)$$

is used for the regularisation of the value  $s_j$  of a source grid cell  $B_j$ . Given a source model such as those in Section 5.3 for the background source, the value  $v_j$  allowed by the prior is calculated as the integral

$$v_j = \int_{B_j} d^2y f_S(\mathbf{y}) \quad (5.37)$$

of the surface brightness  $f_S(\mathbf{y})$  over source grid cell  $B_j$ . It is clear that this choice of prior only permits a discretised version of the background source model, so that the inverse method then depends on the parameters of the source model in the usual way of the forward method.

## 6 The LENSED algorithm

The following chapters have been submitted as N. Tessore, F. Bellagamba and R. B. Metcalf, *Lensed: a code for the forward reconstruction of lenses and sources from strong lensing observations*, preprint (May 2015), arXiv: [1505.07674](https://arxiv.org/abs/1505.07674).

### 6.1 Rationale of the implementation

Lens reconstruction with the forward method, as presented in Chapter 5, could be summarised in the following algorithmic form.

1. Start with an image of observed pixel values  $d_i$  and covariance matrix  $\Sigma$ . If no variance is provided, generate it from the data.
2. Build a model of the lens and sources, using the parameters  $\xi$  with prior probabilities  $P(\xi)$ .
3. Pick a set of parameters  $\xi$  from the prior  $P(\xi)$ .
4. For the chosen parameters, calculate the expected pixel values  $m_i$  using (5.19).
5. Calculate likelihood  $P(d | \xi)$  of the model using (5.23).
6. Calculate the posterior probability  $P(\xi | d)$  using likelihood  $P(d | \xi)$  and prior  $P(\xi)$ .
7. Repeat steps (iii) – (vi) until the parameter space is sufficiently sampled.

Even though the algorithm in this form is conceptually simple, there has so far been no general purpose standard implementation. The forward reconstruction of lenses is mainly a computational challenge, and the existing implementations generally treat the individual requirements of the task they are written to perform. By identifying the key challenges that an implementation faces, one can find a solution that goes beyond the immediately necessary and thus arrive at a generic code for the forward reconstruction of lenses.

**Numerical simulation.** The first problem is step (iv) of the schematic algorithm laid out above. A precise calculation of the expected pixel values (5.19) of the model requires a full ray tracing simulation over the whole field of view of the observed lens system. With modern space-based observations of galaxy-galaxy lensing events, the number of pixels that have to be calculated in this way routinely ranges from 10.000 on the low end to far beyond 100.000, making each numerical simulation of the image costly. As every set of tested parameter values requires a separate simulation, many thousands of these simulations are necessary for one reconstruction. While ways exist to reduce the cost of computation, mainly by a more approximate simulation, there is a natural limit to the amount of time one can save in the calculation before the method breaks down. The necessary increase in performance to make the forward reconstruction feasible must therefore come from elsewhere. One major opportunity for optimisation is parallelisation: It is shown below that the nature of the problem allows for a nearly perfectly parallel computation of the results, and this fact, along with the rise of GPU computing, allow the forward reconstruction to be tackled in a massively parallel way even on normal workstation machines.

**Sampling of the parameter space.** The second problem of the forward method is the sampling of the parameter space, which is step (vii) of the above algorithm. It was mentioned in Chapter 5.6 how the parameter space of a lens model might contain multiple regions with good solutions, as in the case where not all multiple images of a source can be reproduced well at the same time, but different sets of parameter values each recover some of the images. In order to explore the whole parameter space of these multi-modal problems, which are common in strong lensing, an algorithm must be able to move away from “good” parameter values and into uncharted territory. This rules out a standard parameter optimisation approach for reconstruction, and instead requires a thorough sampling of the full posterior distribution. The task is rendered difficult by the usually large number of dimensions, as well as the intrinsic degeneracies of the problem. For example, swapping the major and minor axis of a nearly-circular ellipsoidal lens requires a  $\pm 90^\circ$  change in the position angle, even though both settings lead to physically similar results. Some correlations are intrinsic to surface brightness distributions of sources, e.g. between the position, ellipticity, and position angle. Others arise from gravitational lensing, where observed features of an image can be attributed to both the light deflection by the lens and the intrinsic shape of the background source. Many strategies exist to improve the sampling of the parameter space, and are crucial for an efficient implementation of the forward method.

**The LENSED algorithm.** Due to the difficulties outlined here, it is clear that the forward method for lens reconstruction is as much, and perhaps even more so, a technical challenge for practical computations as it is a theoretical or scientific one, and the rest of this chapter provides a number of possible solutions that should

help overcome some of the common obstacles which any implementation of the forward method faces. All of these techniques have been implemented in the LENSED algorithm for lens reconstruction [103], which is open-source code and publicly available [102]. The guiding principles in the development of LENSED have been the *correctness of the simulation* and the *robustness of the results*. Great care has been taken to avoid cutting computational corners, and focus instead on solutions that attack the forward problem as generally as possible. The result of this effort is a massively parallel algorithm for ray tracing and image comparison that outsources the bulk of the numerical burden to a modern graphics processing unit (GPU). GPUs are by design well-suited to perform geometric calculations in two dimensions, and the choice of computing platform provides the required performance for the reconstruction of the highly resolved data available today from space-based observations. Device code for parallel execution is written in OPENCL (a dialect of C), to ensure compatibility with all commonly used GPUs and also preserve the ability to compute on traditional parallel CPU architectures when necessary or desirable.<sup>1</sup> The chosen computational framework offers the additional benefit that new source and lens models can be implemented quickly — often in a matter of minutes — once their deflection or surface brightness are given in a suitable form for computations, without the need to alter or recompile existing code. This enables the quick development of made-to-measure models for individual reconstructions and numerical experiments in lens reconstructions that complete in hours instead of days. Finally, the setup of the physical system, as well as the program configuration itself, can be done entirely with a single file.

## 6.2 Numerical simulation

The expected pixel values (5.19) must be calculated by integration of the observed surface brightness  $f(\boldsymbol{x})$  over the area  $A_i$  of each pixel. In real applications, such an integration has to be performed numerically, approximating the integral by a weighted sum

$$m_i \approx \sum_{k=1}^N w_k f(\boldsymbol{x}_k) \quad (6.1)$$

of  $N$  sample values of the integrand function  $f$ . The weights  $w_k$  and points  $\boldsymbol{x}_k \in A_i$  are prescribed by some rule for numerical integration. The choice of integration rule determines the quality and speed of the approximation: generally speaking, integration rules with a higher number  $N$  of points are more accurate but slower to evaluate.

**Integration rules.** The simplest estimate of the flux integral evaluates the surface brightness function at only one point  $\boldsymbol{a}_i$  at the centre of a pixel. The result is used

---

<sup>1</sup>An introduction to the OPENCL parallel programming standard was given by Stone, Gohara and Guochun Shi [99].

as the mean value and multiplied with the pixel area  $A_i$  to give  $m_i \approx A_i f(\mathbf{a}_i)$  as a crude estimate of the pixel value. More accurate results can be obtained by using a regular grid of sampling points [86]. When the pixel is subdivided into  $N \times N$  cells with sampling points at their centres, the numerical integration uses the *midpoint rule* in two-dimensions. This “poor man’s ray tracing” technique is common in practice and can deliver good results [60]. It is also possible to position the sampling points at the vertices of the grid. In this case, the result is the *trapezoidal rule* with  $(N + 1) \times (N + 1)$  points. Many more rules exist, such as carefully constructed *quadrature rules* that give exact results for functions up to some given order, or *adaptive integration* schemes that refine the integration until a desired accuracy is achieved, and a large amount of research and expertise is dedicated to the topic of numerical integration [57, 80]. In Chapter 7.5, different integration rules are evaluated in the context of a realistic reconstruction.

**Error estimation.** In order to check the accuracy and precision of the numerical approximation, the error  $\Delta m_i$  of the integral is usually estimated by computing a second value  $m'_i$  from a coarser integration rule with  $N' < N$  weights  $w'_{k'}$  and points  $\mathbf{x}'_{k'}$ . The error estimate is given by the difference

$$\Delta m_i = A m_i - B m'_i = \sum_{k=1}^N A w_k f(\mathbf{x}_k) - \sum_{k'=1}^{N'} B w'_{k'} f(\mathbf{x}'_{k'}) \quad (6.2)$$

of the two approximations, where  $A$  and  $B$  are specific multipliers for the rule that extrapolate the true error from the two evaluations. If the points  $\mathbf{x}'_{k'}$  of the secondary rule are a subset of the points  $\mathbf{x}_k$  of the primary integration rule, the error estimate can be computed directly from a single sum

$$\Delta m_i = \sum_{k=1}^N e_k f(\mathbf{x}_k) \quad (6.3)$$

using the error weights  $e_1, \dots, e_N$ , which combine the different weights at the common points as

$$e_k = \begin{cases} A w_k - B w'_{k'} & \text{if there is } k' \in \{1, \dots, N'\} \text{ with } \mathbf{x}'_{k'} = \mathbf{x}_k, \\ A w_k & \text{else.} \end{cases} \quad (6.4)$$

For a pair of integration rules with this property, the error of the integration can be estimated without any additional evaluations of the function  $f(\mathbf{x})$ , and therefore at little computational cost. While not strictly necessary for the reconstruction of gravitational lenses, it is nevertheless good practice to check that the absolute and relative errors of the numerical integration are reasonably small, and a map of the per-pixel integration error can be provided by LENSED.

### 6.3 Variance estimation

In the common case where an observation does not come with an independent estimate of the covariance between the observed values, the covariance matrix  $\Sigma$  must be estimated from the data  $d$  itself. The basic assumption, here and in the following, is that each pixel value is independently observed, i.e. that the number of counts registered in one pixel does not depend on the counts for any other pixel. The reason for this assumption is twofold. First, there are the practical necessities of estimating the variance, a task which is rendered exceedingly complex if there are inter-pixel correlations to be taken into account. The second, and arguably more important reason is that the approximation leads to a significant reduction in the computational burden of the image comparison. For independent pixels, the covariance matrix  $\Sigma$  is diagonal,

$$\Sigma = \text{diag}(\sigma_1, \dots, \sigma_n) \quad (6.5)$$

and the  $\chi^2$ -term (5.24) that appears in the calculation of image likelihood (5.23) reduces to the simpler sum

$$\chi^2 = \sum_{i=1}^n \frac{(d_i - m_i)^2}{\sigma_i^2} . \quad (6.6)$$

The assumption of independence between pixels is not very far from the truth. Effects such as image degradation by the PSF happen before the counts for a given pixel are registered, and even though they influence the expected flux that arrives at the detector, they do not correlate the actual measurements of the pixel values. However, correlations between pixels can be (and most certainly are) introduced by the instrument electronics or data reduction techniques such as drizzling [38]. The assumption is therefore that these correlations are small, and that the variance for each pixel is enough to describe the statistics of the observation adequately.

**Poisson variance estimation.** When the observed signal is sufficiently strong, the per-pixel variance can be estimated from the Poisson statistics of the photon flux. The total photon counts  $k_i$  for each pixel are

$$k_i = g_i (d_i + b_i) , \quad (6.7)$$

where  $g_i$  is an effective gain and  $b_i$  is an eventual offset that was subtracted from the input data. The effective gain is the conversion factor from the data units to photon counts; for example, given an observation in detector units per unit time, the effective gain is

$$g_i = (\text{electronic gain}) \times (\text{exposure time}) . \quad (6.8)$$

The offset  $b_i$  is any constant that has been subtracted from the pixel values; this is often the estimated sky background. Assuming that the photons arrive at the

detector with some fixed rate given by the physical system under observation, the counts  $k_i$  follow a Poisson distribution

$$k_i \sim \text{Pois}(\lambda_i) \quad (6.9)$$

with parameter  $\lambda_i$ . The value of  $\lambda_i$  is estimated from the observation as  $\lambda_i \hat{=} k_i$ . The variance of the pixel counts  $k_i$  follows from the Poisson distribution,

$$\text{Var}[k_i] = \lambda_i \hat{=} k_i = g_i (d_i + b_i) . \quad (6.10)$$

Hence the variance  $\sigma_i^2$  of the pixel values  $d_i$  can be found by rearranging (6.7) as

$$d_i = g_i^{-1} k_i - b_i , \quad (6.11)$$

and calculating the variance of the individual terms

$$\sigma_i^2 = \text{Var}[d_i] = g_i^{-2} \text{Var}[k_i] \hat{=} g_i^{-1} (d_i + b_i) . \quad (6.12)$$

This is the estimator of the variance in case no such estimate was provided by the observation.

**Observations with low signal.** When the signal from astronomical sources is low, the simple Poisson model of the pixel distribution is no longer valid, and other processes become significant, such as noise due to the read-out process. These are not considered in the statistical variance described above and are more difficult to estimate. Determining the noise level directly from the data, e.g. from the RMS values of empty patches of sky, depends highly on the data processing pipeline and can easily bias the reconstruction. In this case, a more careful preparation of the variance map is necessary, so that the particulars of the observation can be correctly taken into account.

## 6.4 Sampling the parameter space

For a practical application, it is almost always infeasible to explore the posterior distribution (5.28) with a classic MCMC method, due to the high dimensionality of typical models and the usually strong correlations between individual model parameters. A recent alternative to traditional MCMC samplers is the Nested Sampling algorithm [94, 95]. LENSED uses the MULTINEST library [35–37], which is an implementation and extension of the Nested Sampling algorithm that is well suited for working with the  $10 < n < 50$  parameters, multiple modes, and strong correlations that typically arise in strong lensing reconstructions. In addition to finding the posterior distribution of the parameters, MULTINEST also calculates the evidence (5.29), which is a notoriously difficult problem in numerical Bayesian statistics.

**Sampling with MULTINEST.** For any given problem, MULTINEST requires the logarithm of likelihood (5.27) of the parameter values, which is

$$\log P(d | \xi) = \sum_{i=1}^m -\frac{1}{2} \left\{ \frac{(d_i - m_i)^2}{\sigma_i^2} + \log(2\pi \sigma_i^2) \right\}. \quad (6.13)$$

Since the variance  $\sigma_i^2$  is fixed for the reconstruction, the second term amounts to an overall normalisation that has no bearing on the results and thus can be dropped. The calculations are then performed with the simplified log-likelihood

$$\text{loglike}(d | \xi) = -\frac{1}{2} \sum_{i=1}^n w_i (d_i - L_i)^2, \quad (6.14)$$

where the weights  $w_i = 1/\sigma_i^2$  were introduced as the inverse of the variance. The advantage of the weights  $w_i$  over the variance  $\sigma_i^2$  is that a pixel can easily be masked by setting its weight to zero. It should further be noted that (6.14) now amounts to the  $\chi^2$  term (6.6), which is used to summarise the ability of the given parameter values  $\xi$  to reconstruct the observed data.

**Sampling settings.** Nested samplers, and MULTINEST in particular, offer many settings that can be tweaked to find the right balance between thoroughness and speed of the sampling for a given task. Within LENSED, these are set to reasonable defaults which work well in typical situations, with a slightly larger emphasis on speed. As in every numerical problem, it is unfortunately difficult to find values that work perfectly in all cases. It is generally a good idea to consider the details of the MULTINEST algorithm and try other combinations of parameters which work better for the specific problem at hand [35–37]. This can lead to significant improvements in speed, quality, or occasionally both.

## 6.5 Parallel computation

Reconstructions of CSWA 1, one of the largest galaxy-scale lenses, from *HST* data require the simulation and comparison of approximately  $500 \times 500$  pixel images. Assuming the 16-point integration rule from Section 6.2, a total of  $4 \times 10^6$  rays have to be traced from image plane to source plane for each simulation of the model. Every ray requires evaluation of the deflection for all lens components, and evaluation of the surface brightness function for all of the foreground and background source components. After the rays for a pixel have been added, and a possible PSF has been applied, every resulting pixel value has to be subsequently compared to the observation, using the provided covariance matrix. It is clear that the computational cost is one of the main issues in any implementation of the forward method.

**Ray tracing.** Even though the number of required ray tracing calculations is very large, their particular properties show huge potential for optimisation. This is based on the following observation. Once the model of the lens system is defined and its parameters are set, the calculations for any ray — i.e. the deflection and surface brightness evaluations — are entirely independent. Such “embarrassingly parallel” problems [64] can be perfectly parallelised with minimal changes to the computation. In this case, it is only necessary to initially distribute the model, parameter values and ray positions to all processors, because no inter-process communication is required at all during the ray tracing. Furthermore, if all rays for a single pixel are assigned to the same processor,<sup>2</sup> the numerical integration can be performed locally, thereby rendering the entire simulation of the image perfectly parallel. Not counting the initial overhead for constructing the model and possible subsequent updates of the parameter values, the performance of the simulation should increase linearly with the number of processors.

**Point spread function.** The situation is not as ideal for the application of a PSF to the simulated image. For the application of a PSF via discrete convolution (5.21), the results for any individual pixel are in principle independent of the convolution of other pixels. However, the computation requires pixel values in a PSF-sized neighbourhood around each pixel. Therefore, if not all of the simulated image is available at once (e.g. when not all pixels have been simulated yet, or because of distributed memory), the image must be partitioned into rectangular blocks which are to be processed independently. Pixels in the interior of the block will then have neighbouring values available, but pixels near the border still require values outside the block itself. It is thus necessary to make a larger portion of the simulation available to each block, with half the size of the PSF as “padding”. Intuitively, larger block sizes correspond to less relative overhead in the number of required pixels, which might require less communication between processes and hence less overhead in the computation. Once these requirements are fulfilled, each block can be convolved in parallel. If the number of blocks remains larger than the number of processing units, and the reading overhead per block is small, parallelisation of the direct convolution can still offer near-linear performance improvement over individual convolution of the pixels.

**Image comparison.** The comparison of simulated image and observation is done by the image likelihood (5.23), which is effectively the calculation of the value of  $\chi^2$  as defined in (5.24). Even though the required operations themselves are simple, the large number of terms to be computed means that a significant amount of time might be spent on the comparison, and it is worthwhile to perform it in parallel. It is assumed that the relevant fixed parts of the comparison, i.e. data and covariance matrix, are initially distributed to all processing units. If the covariance matrix is

---

<sup>2</sup>This does not affect parallelisation as long as there are more pixels than processors.

diagonal, as assumed, the evaluation of the  $\chi^2$  term (5.24) reduces to the sum

$$\chi^2 = \sum_{i=1}^n \frac{(d_i - m_i)^2}{\sigma_i^2}. \quad (6.15)$$

Computation of the sum can be split into two parts. First, the terms  $(d_i - m_i)^2 / \sigma_i^2$  can be evaluated independently for each pixel. Depending on their number (i.e. the number of pixels), parallelisation of this step can lead to some improvement in performance even though the operations are primitive, especially when the values of the pixels are already distributed to the processing units from prior calculations. Secondly, the sum has to be reduced to a single value. While it is certainly possible to perform the summation in parallel [9], this step is not as good a candidate for parallelisation and might not offer any gain over serial summation, in particular when communication of the individual terms to a single processor is fast.

## 7 Testing the forward method

### 7.1 Testing reconstructions with mock data

Before an implementation of the forward method such as LENSED can be used in applications, it is necessary to carefully assess its performance in a controlled setting under realistic conditions. This serves first and foremost to make sure the implementation works as intended. These tests of *verification* are internal to the implementation, and help identify bugs and other technical issues.<sup>1</sup> For example, the recovery of source parameters can be tested on observations without lensing, and the results compared to known codes such as GALFIT [75, 76]. This can be done for both real and mock observations, so that the performance of the code in reconstructing real source can be compared to current methods [70]. Testing the lensing features in a sandbox environment is more tricky: A possibility is the generation of images with well-aligned lens and source configurations for which analytical results are available, and check that the results contain the expected phenomena of Einstein rings or multiple images (Chapter 2.5 and 3).

**The constraining power of the forward method.** A different and scientifically more interesting kind of test concerns itself with the *validation* of the forward method. Although the forward problem laid out in Chapter 5 is well defined and understood, it is nonetheless not *a priori* clear how well a model of a lens system can be constrained by it, even with a perfect algorithm. Degeneracies can arise not only due to physical mechanisms such as the mass sheet degeneracy, which does not apply when the lens model follows a fixed functional form [30], but rather intrinsically when there is either too much freedom in the problem to recover any meaningful results, or so little freedom that results are never found. Hence it is necessary to carefully characterise the ability of any reconstruction method to constrain the models it is given, and in the following a number of tests for this task are developed and applied.

---

<sup>1</sup>Every program has bugs. And every program can be shortened. Therefore, as the saying goes, any program can be reduced to a single line that does not work. — *UNIX and Linux System Administration Handbook*

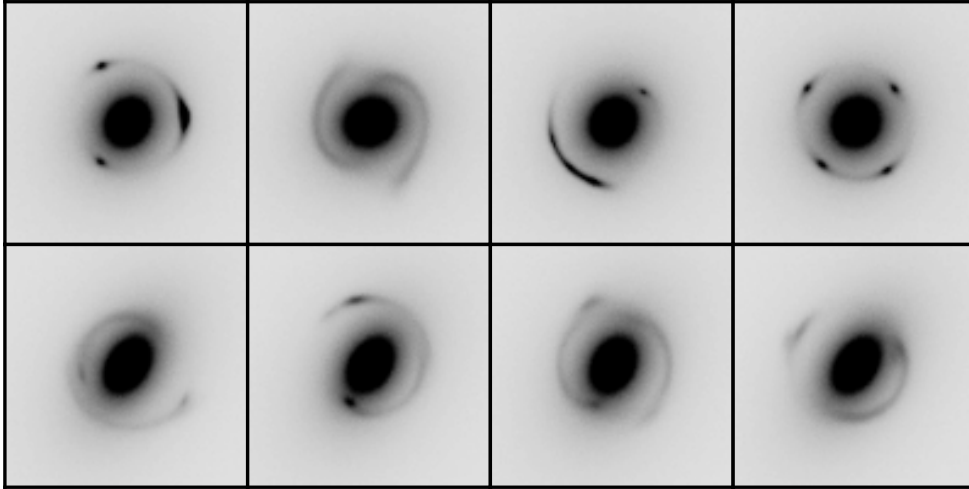


Figure 7.1: Sample mock observations of strong lenses. The lensed background sources use parametric Sérsic profiles (*top*) and observed galaxies decomposed into a shapelet basis (*bottom*) and are prepared as observation ensembles with randomised parameters. Images are *HST*-like with realistic noise and PSF and a side length of 6 arcsec. The lens is a singular isothermal ellipsoid located at the centre of the image, with Einstein radius  $r_L = 1.3624$  arcsec, axis ratio  $q_L = 0.75$ , and position angle  $\theta_L = 45^\circ$ . The foreground galaxy follows a semi-randomised de Vaucouleurs profile.

**Mock data pipeline.** For the following tests, mock observations are generated which realistically reproduce a space-based observation of the lensing system. Particularly, the images simulate a *HST*-like configuration of the virtual telescope for a 2000 second exposure in the *F814W* band. A typical PSF made with TINY TIM is used for image synthesis and reconstruction [56, 105]. The resulting images have a size of  $120 \times 120$  pixels at a resolution of 0.05 arcsec/px, giving a total side length of 6 arcsec. Realistic mock observations can be realised with existing packages such as GLAMER, a gravitational lensing simulator [63, 78]. The choice of space-based mock observations is due to the fact that the parameter space of detailed, high resolution images is generally more difficult to sample in a reconstruction. Ground-based observations of similarly-sized lenses contain fewer pixels, a larger PSF, and higher noise levels, which leads to a smoother likelihood with broader maxima that is easier to sample. Hence, if the method is able to reconstruct lenses in highly-resolved space-based observations, it is likewise expected to perform well on less detailed data (although the results will naturally be less precise).

## 7.2 The influence of lensed sources

The most important characteristic of a lens reconstruction algorithm must be its ability to actually constrain the parameters of the lens models it is given. This is not as straightforward a task as it may seem, because the reconstruction of any lens system depends crucially on the information provided by the lensed background sources. On one hand it is clear that if there are no visible signs of strong lensing in the observation, perhaps due to a grave misalignment between lens and source, then it will be impossible to constrain any lens parameters at all. On the other hand, a perfect alignment of an extended source and e.g. a circularly symmetric lens will illuminate the whole critical line, and the resulting Einstein ring allows an easy fixing of all lens parameters. Most real lens systems are of course somewhere in between these two extremes, and the degree to which they can be reconstructed will depend crucially on the particulars of the source. Hence it is clear that any test which strives to objectively quantify the reconstructive power of the forward method must somehow isolate the influence of the source on the results for lenses.

**Marginalising the influence of sources.** The desired source-independent test of lens reconstruction can be developed in analogy to the usual rules of probabilities. Denoting the true parameter values of the lens in a mock observation by  $\xi_0$ , the constraining power of the chosen lens reconstruction method is encoded in the probability  $P(\xi | \xi_0)$  of recovering any set of lens parameters  $\xi$ . Because the results of a single reconstruction depend quite strongly on the configuration  $\nu_0$  of the lensed sources, only the distribution  $P(\xi | \xi_0, \nu_0)$  can actually be observed. The desired distribution is related to the observable one through a marginalisation

$$P(\xi | \xi_0) = \int d\nu_0 P(\xi | \xi_0, \nu_0) P(\nu_0) \quad (7.1)$$

over all possible source configurations, which are distributed according to  $P(\nu_0)$ . The same concept of marginalising over source configurations can be turned into an experimental setup to disentangle the influence of the source from the lens reconstruction. For a given lens system, an ensemble of mock observations is prepared as follows. In each observation, the source parameters  $\nu_0$  are randomly drawn according to some distribution  $P(\nu_0)$ , while the lens is being kept fixed. Each observation is subsequently reconstructed on its own, resulting in one value of  $P(\xi | \xi_0, \nu_0)$ . In the end, the posterior distributions of the lens parameters are combined from all individual realisations of the source. This process is analogous to a Monte Carlo integration of the marginalisation (7.1), and the final result is the desired posterior distribution  $P(\xi | \xi_0)$  that truthfully represents the constraining power of the method, where the influence on the source is eliminated.

**Creating ensembles of observations.** The required ensembles of observations can be created in the following way. As noted, the parameters of lens model to be investigated are fixed over the whole set of observations. In order to restrict the

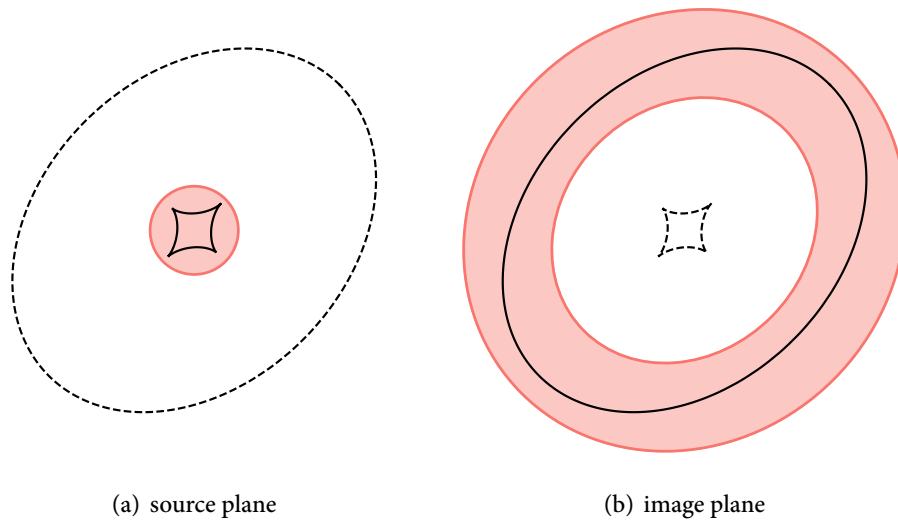


Figure 7.2: Distribution of the position of sources in an observation ensemble. The sources are randomly located within a disk that circumscribes the caustic of the lens (*left*). Also shown is the approximate resulting distribution of observed images, which forms an annulus containing the critical line (*right*).

sample of observations to reasonable candidates for strong lensing, the sources are positioned uniformly inside a disk circumscribing the caustic of the lens, as shown in Figure 7.2. The remaining source parameters are distributed “naturally”, e.g. uniformly between  $0^\circ$  and  $180^\circ$  for the position angle. The resulting images contain a good representation of the naturally occurring phenomena in strong lensing and cover a wide range of the lens systems for which the forward method was intended, with multiple images, arclets, large arcs, rings and crosses all readily found in the sample.

### 7.3 Reconstruction of lenses

With the testing procedure established, the constraining power of a code such as LENSED with respect to known lens parameters is now investigated. In total, two different tests are performed that involve a different kind of background source. The first uses mock data generated with and reconstructed by a parametric Sérsic model. This test represents the ideal situation in which the lens system can be modelled exactly, and therefore puts an absolute upper limit on the ability of the reconstruction method to recover the parameters of the lens. The ideal situation is subsequently relaxed in a second test where the mock data is generated from Shapelet sources, but the reconstruction is still performed with a single Sérsic component. The results can demonstrate the robustness — or lack thereof — of the reconstructed lens parameters when the background sources are not described

perfectly by the assumed model. For each test, a set of 100 mock observations is prepared with a fixed lens model, detailed below, where sources are randomised as described above.

**Lens model.** The lens is a central singular isothermal ellipsoid (Chapter 3.3) with fixed parameters Einstein radius  $r_L = 1.3624$  arcsec, axis ratio  $q_L = 0.75$ , and position angle  $\theta_L = 45^\circ$  between the major axis and  $x$ -axis. Assuming typical lens and source redshifts of  $z_L = 0.2$  and  $z_S = 1.0$ , the Einstein radius corresponds to a velocity dispersion of  $\sigma_v = 250$  km s $^{-1}$  for the isothermal ellipsoid. Co-centred with the mass distribution is a 16.5 mag foreground galaxy. Based on the majority of current galaxy-scale lensing observations, this is reasonably assumed to be an early-type object, which is well parameterised by a de Vaucouleurs profile [118]. The effective radius of the light profile is fixed at  $r_H = 2$  arcsec, or about 1.5 Einstein radii, which is a realistic ratio for typical lensing galaxies [96]. Other parameter values are randomly assigned for each image, using an axis ratio  $q_H$  between 0.6 and 0.9, and major axis angle  $\theta_H$  between  $25^\circ$  and  $65^\circ$ , in order to maintain a certain alignment between the respective light and mass profiles. A number of sample images are shown in Figure 7.1.

**Constraints from an exact model.** The first test is the reconstruction of a lens system which can be modelled exactly. Because the reconstruction is not limited by insufficient knowledge of the model, this exercise provides an upper bound on the constraining power of the method. Given that the aim here is not to create a realistic model, but rather one that can be recovered perfectly, the generated mock observations can contain only a single background component, which follows a parametric Sérsic profile (Chapter 5.3). Each image uses a different realisation of uniformly random source parameters, with Sérsic index  $n_S$  between 0.5 and 8.0, effective radius  $r_S$  between 0.1 and 0.4 arcsec, axis ratio  $q_S$  between 0.1 and unity, and position angle  $\theta_S$  between  $0^\circ$  and  $180^\circ$ . The range for the effective radius is compatible with observational results [92], while the ranges for other parameters allow for a very general set of possible source configurations. The magnitude of the background galaxies before lensing is 23 mag in each case.

The ensemble of observations is subsequently reconstructed with the forward method, using an SIE lens model where all parameters are left free. This was done using the LENSED algorithm. In most cases, the recovered maximum-likelihood lens parameters are very close to the input values. Possible outliers are usually those with a generally unsuccessful reconstruction ( $\chi^2/\text{dof} > 4$ ), indicating a likely insufficient sampling of the parameter space that terminated before the true maximum-likelihood region was found. Since the reconstruction with a MCMC sampler or related method (Chapter 6.4) involves a degree of randomness, such behaviour is occasionally expected, and the high value of  $\chi^2/\text{dof}$  and can be used to detect these cases. Further analysis of the offending cases with a more thorough sampling of the parameter space (e.g. increased number of live points for nested

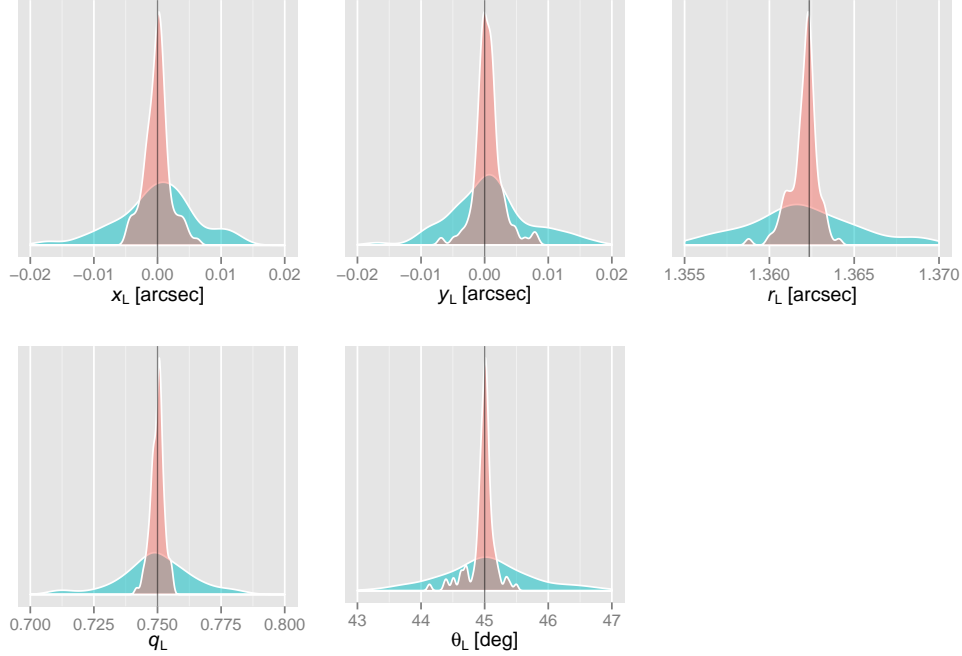


Figure 7.3: Posterior distributions of the lens parameters using an exact (*red*) and inexact (*blue*) model for the background sources. Shown are the position  $x_L$ ,  $y_L$ , Einstein radius  $r_L$ , axis ratio  $q_L$ , and position angle  $\theta_L$  of a singular isothermal ellipsoid. Input parameter values are indicated by a vertical line (*black*). Results are marginalised over ensembles of observations with randomised sources, see text. The analysis was performed using the LENSED algorithm on *HST*-like mock observations [103].

| parameter        | input value | exact source model    | inexact source model |
|------------------|-------------|-----------------------|----------------------|
| $x_L$ [arcsec]   | 0           | $-0.0000 \pm 0.0020$  | $-0.001 \pm 0.011$   |
| $y_L$ [arcsec]   | 0           | $0.0005 \pm 0.0021$   | $-0.001 \pm 0.013$   |
| $r_L$ [arcsec]   | 1.36235     | $1.36205 \pm 0.00080$ | $1.3619 \pm 0.0059$  |
| $q_L$            | 0.75        | $0.7499 \pm 0.0026$   | $0.750 \pm 0.016$    |
| $\theta_L$ [deg] | 45          | $44.97 \pm 0.20$      | $45.2 \pm 1.7$       |

Table 7.1: Results of the reconstruction of mock images using an exact and inexact model for the background sources. Shown are the parameters for position  $x_L$ ,  $y_L$ , Einstein radius  $r_L$ , axis ratio  $q_L$ , and position angle  $\theta_L$ . The quoted values are the sample mean and standard deviation of the marginal distribution over 100 randomised realisations of the lens system, as shown in Figure 7.3

samplers, or reduced tolerance) usually aligns the results with the rest of the set, and the outliers do not represent a true problem for the forward reconstruction method.

The recovered distributions of the lens parameters, marginalised over other parameters and over the ensemble of source realisations, are shown in Figure 7.3. No systematic bias is apparent in the outcome, and the results are distributed tightly around the true values. This is substantiated in Table 7.1, which contains the sample mean and standard deviation of the marginalised lens parameters. The accuracy of the results, i.e. the distance of the reconstructed mean from the true value, is remarkably high. The precision of the results, i.e. how much the recovered values are scattered about their common mean, is excellent as well: The position, Einstein radius, axis ratio, and orientation are constrained far below the pixel, percent, and degree level, respectively.

This basic test validates the forward method and implementation choices for lens reconstruction as presented so far, in a scenario where the model is completely known. Lens parameters are recovered almost identically and without apparent systematic biases, at a precision far below the model uncertainties in observations of real lens systems.

**Constraints from an inexact model.** So far, the model used for reconstruction agreed with the model used in the generation of the data, resulting in very tight constraints on the lens parameters. It is expected that these are loosened once the lensed background sources no longer correspond perfectly to the assumed model. To this end, a second ensemble of images is created, in which background sources do not follow an analytical profile, but are based on Shapelets instead (Chapter 5.3). The sources are randomly extracted from a catalogue of observed galaxies in the Hubble Ultra Deep Field [27] and subsequently decomposed into a Shapelet basis. For the virtual observations, only galaxies with a redshift between 0.8 and 1.5 are selected, to ensure a sample of galaxy shapes consistent with an assumed source redshift of  $z_S = 1.0$ . Galaxies that were observed with low S/N are filtered out by a cut in apparent magnitude at 27 mag. Each object is appropriately rescaled to have a magnitude of 23 mag before lensing and the same apparent size it would have had at redshift  $z_S = 1.0$ .

The new ensemble of mock observations is reconstructed with the same model as before, i.e. a singular isothermal ellipsoid and a de Vaucouleurs foreground galaxy, and a background galaxy following a Sérsic profile. However, the images now contain a realistic variety of shapes and structure in the lensed background sources that cannot be modelled exactly. The impact on the ability to recover lens parameters can be seen in the results of a reconstruction using LENSED, shown in Figure 7.3. The loss in precision due to the inexact nature of the model is clearly visible in the widened distributions for the recovered lens parameters. Still, the resulting distributions are remarkably symmetric and centred on the true values. The accuracy of the results, i.e. the difference of the recovered mean and the true

input value, over the whole sample of 100 reconstructions is quoted in Table 7.1; it remains far below the respective scales of one pixel, percent, or degree for all lens parameters. Even though the standard deviation of the individual parameters has increased five- to tenfold over the exact case, the precision is still excellent, with constraints on the position and Einstein radius at the intrapixel level, the axis ratio at the per cent scale, and the orientation correct to within two degrees.

This second test concludes the validation of the forward method to constrain lens parameters even when it is not possible to model the lensed galaxies exactly. Shapelet sources in this test are diffuse, usually with multiple peaks and troughs in the brightness distribution, and are generally only poorly fit by a single Sérsic component. Nevertheless, using the forward reconstruction method, it is possible to constrain the parameters of the given lens model to a very high degree. Because the reconstruction of real observations is expected to be limited first and foremost by model uncertainty due to an insufficient description of the mass distribution, the loss in constraining power from imperfectly modelled sources is insignificant in comparison. The reconstruction of lens parameters from real observations is therefore limited neither fundamentally nor by the proposed implementation of the forward method.

#### 7.4 Reconstruction of lensed sources

There are many applications in which a gravitational lens is only the telescope through which a faint, distant high-redshift source can be observed [5, 60, 70]. For these cases, the reconstructions of the source becomes as important as the reconstruction of the lens, and both must be performed at the same time. While it was shown in Section 7.3 that lens reconstruction is robust even when the sources are not characterised perfectly by their assumed model, the same is not necessarily true for the reconstruction of source parameters under the influence of lensing, and this question merits further testing of the forward method.

**Source parameters from an exact model.** Again, the first step is to validate that the forward method is able to reconstruct source parameters given an exact model. For this, the same ensemble of observations as before can be used, if instead of the parameters  $\xi$  themselves the error of the reconstruction  $\Delta\xi = \xi - \xi_0$  is considered, so that all realisations have a common expectation value  $E[\Delta\xi] = 0$ . The results of such an analysis are shown in Figure 7.4, and a summary is given in Table 7.2. Photometric precision in this case of an exact model is 0.07 mag at the  $2\sigma$  level, and the effective radius  $r_S$  of the sources is constrained to 12% precision at the  $2\sigma$  level. The least constrained parameter is the Sérsic index  $n_S$ , with a relative uncertainty of 10% at the  $2\sigma$  level due to the general difficulty of recovering highly peaked sources (i.e. those with  $n_S > 2$ ). Finally, the position angle  $\theta_S$  is very well reconstructed when the source is clearly elliptical, up to axis ratios of  $q_S \approx 0.85$ , while for almost circular sources, the position angle is naturally unconstrained.

Overall, the forward method can reliably find the parameters of parametric sources which have been distorted by an unknown lens that is simultaneously reconstructed. This is perhaps not a great surprise, but it is still a good validation of the fact that degeneracies and correlations between lens and source model do not impede the forward method’s ability of recovering source parameters. The next step must now test whether this remains true if the sources are no longer described perfectly by the model used for their reconstruction.

**Source parameters from an inexact model.** The problem in the reconstruction of lensed sources is gauging whether the lensing in itself influences the recovered parameters. In reconstructions that use e.g. a Sérsic model for the lensed sources, it might be that the reconstruction finds systematically different Sérsic indices due to the interactions of the deflection and the source profile. It must therefore be tested whether or not the reconstruction of a non-parametric surface brightness distribution is the same when done in front of or — theoretically — behind the lens, i.e. whether the source reconstruction is invariant under lensing. The main difficulty of this test is the absence of input parameters which can intrinsically be compared to the lens results. The first step is therefore necessarily finding the “input” parameters of each individual source in the assumed Sérsic model. This is unfortunately not as easy as taking the deflector out of the lens system, because the resulting unmagnified sources would be unrealistically small and faint for a direct reconstruction. For an objective comparison, both the total luminosity and the effective resolution of the non-lensed sources have to be increased until they are equivalent to their lensed counterparts. This can be achieved using a uniform magnification that has the same total magnification  $|\mu|_{\text{tot}}$  as in the case of lensing. In practice, the luminosity and the area of the sources are multiplied by  $|\mu|_{\text{tot}}$ . Equivalently, their magnitude is increased by  $-2.5 \log_{10}(|\mu|_{\text{tot}})$ , and each source is scaled by a factor of  $\sqrt{|\mu|_{\text{tot}}}$ . These relations can also be used to quickly find the value of  $|\mu|_{\text{tot}}$  from the lensed images: It is the ratio of total luminosity of the lensed sources (without noise) and the input luminosity before lensing.

Once the equivalent Sérsic parameters of the non-parametric sources have been found, the recovered and expected parameters can be compared as in the case of parametric sources. The resulting marginal distributions are shown in Figure 7.4. While the shape (position  $x_S$ ,  $y_S$ , axis ratio  $q_S$ , position angle  $\theta_S$ ) and the luminosity (magnitude  $\text{mag}_S$ ) of the sources are less constrained with respect to the fully parametric case, the constraints on the Sérsic profile (effective radius  $r_S$  and Sérsic index  $n_S$ ) remain practically unchanged. This is substantiated in Table 7.2, which shows only a minor increase in variance for these parameters.

This final validation of the forward reconstruction method has shown it to allow for a robust parameterisation of sources under the effect of strong lensing.

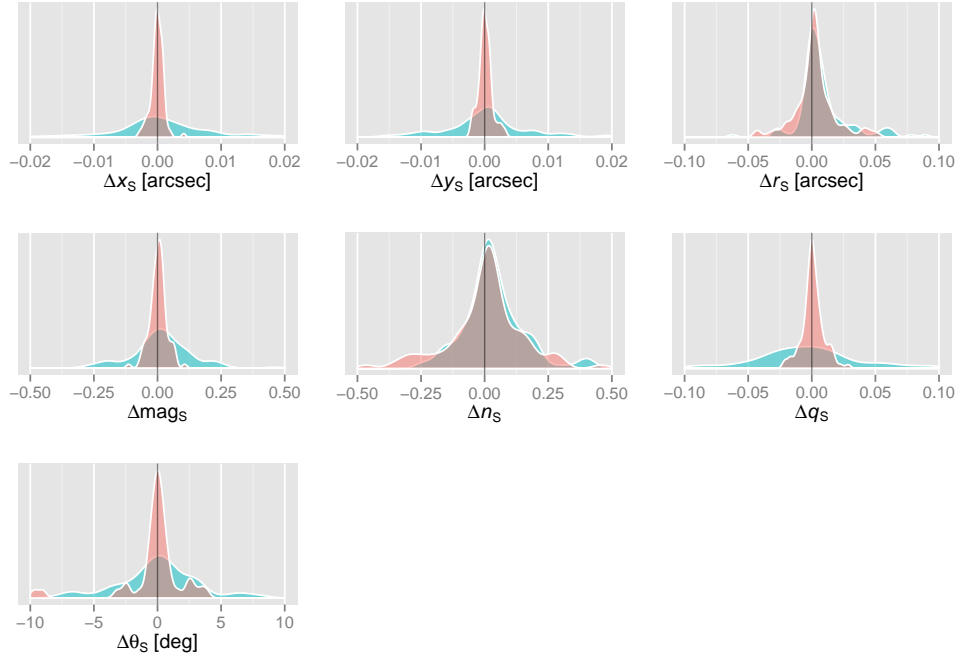


Figure 7.4: Posterior distributions of the source parameters using an exact (*red*) and inexact (*blue*) model for the background sources. Shown are the errors of the reconstruction  $\Delta = (\text{recovered}) - (\text{input})$  for the recovered position  $x_S$ ,  $y_S$ , effective radius  $r_S$ , magnitude  $\text{mag}_S$ , Sérsic index  $n_S$ , axis ratio  $q_S$ , and position angle  $\theta_S$  of the lensed sources, which are modelled in both cases with a Sérsic profile. Input parameters for the inexact sources were found as explained in the text. Results were obtained using the LENSED algorithm on *HST*-like mock observations. The results are marginalised over ensembles of observations with randomised sources, see text.

| parameter               | exact source model   | inexact source model |
|-------------------------|----------------------|----------------------|
| $\Delta x_S$ [arcsec]   | $-0.0000 \pm 0.0010$ | $-0.002 \pm 0.027$   |
| $\Delta y_S$ [arcsec]   | $0.0001 \pm 0.0011$  | $-0.002 \pm 0.029$   |
| $\Delta r_S$ [arcsec]   | $0.003 \pm 0.019$    | $0.008 \pm 0.034$    |
| $\Delta \text{mag}_S$   | $0.003 \pm 0.033$    | $0.03 \pm 0.19$      |
| $\Delta n_S$            | $0.01 \pm 0.25$      | $0.07 \pm 0.25$      |
| $\Delta q_S$            | $0.0009 \pm 0.0085$  | $-0.005 \pm 0.046$   |
| $\Delta \theta_L$ [deg] | $-1 \pm 14$          | $1 \pm 15$           |

Table 7.2: Constraining power of the forward method for the parameters of lensed background sources. Shown are results for the errors  $\Delta$  in the recovery, which are expected to vanish. The corresponding distributions are shown in Figure 7.4.

## 7.5 Choice of integration rule

To conclude the set of tests, it is briefly investigated how the results presented here are influenced by the choice of integration rule for the simulation of the model (Chapter 6.2). As mentioned, any implementations of the forward method has to select a suitable integration rule that is sufficiently fast and sufficiently accurate. The latter part is important as errors in the calculation of the expected image must be small enough not to degrade the results of the lens reconstruction. On the other hand, there is no need to waste time on a perfect integration when it can be shown that this does not improve the quality of the results. As usual in numerics, experimentation and testing is required to find the right choice for the task at hand, and an example is shown here.

**Comparison of different rules.** The tests of this chapter can be repeated using different integration rules, in order to observe their influence on the recovered parameters. The results of such an experiment using the exact test set is shown in Figure 7.5. The evaluated integration rules are

- `point` – a single point at the centre of each pixel,
- `sub2` –  $2 \times 2$  subsampling of the pixels,
- `sub4` –  $4 \times 4$  subsampling of the pixels,
- `g3k7` – Gauß–Kronrod quadrature rule [57, 74] with  $7 \times 7$  points,
- `g5k11` – Gauß–Kronrod quadrature rule with  $11 \times 11$  points, and
- `g7k15` – Gauß–Kronrod quadrature rule with  $15 \times 15$  points,

The model parameters for the lens are position  $x_L, y_L$ , scale radius  $r_L$ , axis ratio  $q_L$  and position angle  $PA_L$ , while the source has position  $x_S, y_S$ , effective radius  $r_S$ , magnitude  $mag_S$ , Sérsic index  $n_S$ , axis ratio  $q_S$ , and position angle  $\theta_S$ . The results show a clear convergence of the results for the Gauß–Kronrod rules, while  $4 \times 4$  subsampling has similar accuracy when only the lens parameters are considered. Given the substantially lower number of points (16 instead of  $\geq 49$ ), one concludes that  $4 \times 4$  subsampling is the integration rule of choice for lens reconstruction, at least for *HST*-like data using a realistic PSF at the same resolution. When source parameters are required, one of the Gauß–Kronrod rules might be preferable in order to not bias the results. Similar tests can be performed when investigating other kinds of observations, in order to determine the optimal integration rule to use in each case.

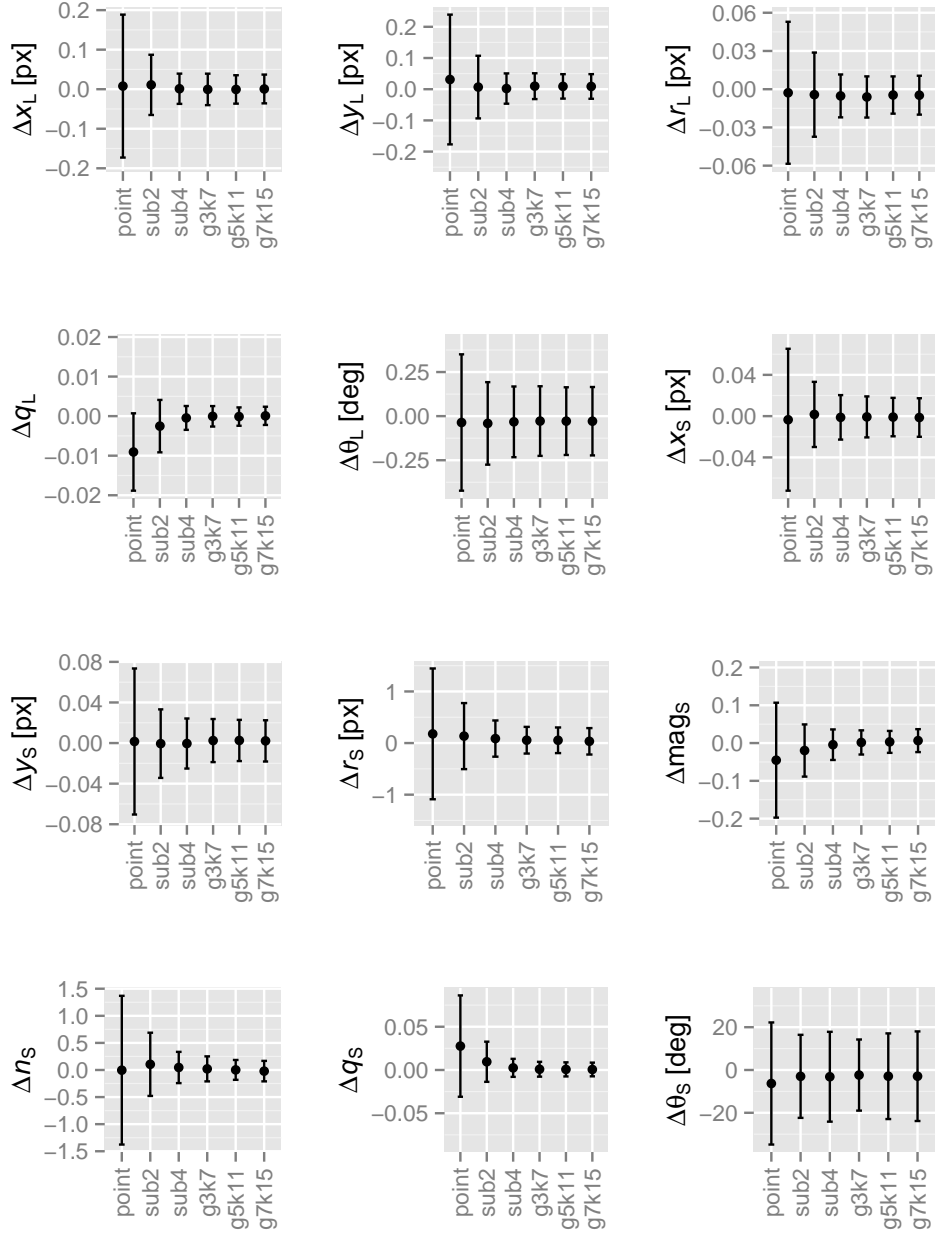


Figure 7.5: Comparison of lens reconstruction results for different integration rules. Shown are the mean and standard deviations for the errors  $\Delta$  over the sample of 100 reconstructions as a function of the chosen integration rule. For a list of the integration rules tested see text.

## 8 Application: Strong lensing surveys

### 8.1 Analysis of lens surveys

A major application for the parametric reconstruction of lenses are lens surveys that observe a large number of candidate lens systems with comparable properties. Naturally, the output of such a survey must be analysed. When there are hundreds of systems to be investigated — and possibly thousands for the next generation of surveys [28] — it becomes necessary to create a robust reconstruction pipeline that can handle the enormous amount of data. The forward method presented here is a natural candidate for this procedure, as it allows for the prescription of a well-defined, physically motivated lens and source model for the reconstruction. This is crucial in an application where not every result can be inspected manually, as the recovered parameters do not need additional interpretation and can quickly be checked for unrealistic or otherwise “strange” results indicating problematic reconstructions. Furthermore, the results from a large catalogue of lenses can lead to new insights about the distribution of the model parameters, which in turn allows for a deeper understanding about the physical nature of the observed systems.

**The Sloan Lens ACS survey.** An example of a large survey of strong lenses is the Sloan Lens ACS (SLACS) project [3, 4, 10–12, 19, 39, 40, 53, 70, 93, 106–109]. The survey performed space-based follow-up observations with *HST* of  $\sim 100$  lens candidates which were identified through ground-based SDSS spectroscopy. The final SLACS catalogue [3] contains 85 confirmed lenses and 13 likely ones. Among the major results of the survey is the analysis of the lens population showing that the radial mass density profile is inconsistent with a light-traces-mass model, and instead appears to be approximately isothermal. The main analysis of the lenses was performed with a method similar to the one presented here, which will now be compared in detail.

### 8.2 Comparative reconstruction

The SLACS lenses were originally analysed by Bolton et al. [11] using a variant of the forward method. Multiple preprocessing steps carefully removed foreground

objects, including the lensing galaxy, from the observation. The cleaned images were subsequently modelled using a singular isothermal ellipsoid positioned at the centre of the estimated foreground light distribution, and a background source containing a number of Gaussian or Sérsic components as necessary to obtain a good fit. Initial parameters of the model were found manually, and subsequently optimised by the Levenberg-Marquardt algorithm as implemented in the MPFIT routine of the IDL software package [66, 67]. The list of reconstructed model parameters, as well as model images and their residuals, is available [11].

In order to show the feasibility of the analysis of real data with the forward method as presented here and implemented in `LENSED`, a small sample of lenses from the SLACS catalogue is reexamined. Specifically, the first 8 observations of *HST* proposal 10886 [13] that are available on the Hubble Legacy Archive [44] are considered. This choice of sample observations is completely arbitrary but interesting, as it contains 7 systems previously modelled by Bolton et al. [11], which are used for comparison, and one system not modelled in the original analysis due to the presence of a companion to the lens galaxy, which highlights the power of the `LENSED` algorithm. Each observation is taken from the *F814W* band and contains 4 combined, cleaned and aligned exposures with a total exposure time of  $\sim 2100$  seconds. The full list of observations can be found in Table 8.1.

**Reconstruction method.** The base model for this analysis consists of a Sérsic component for the foreground galaxy, a singular isothermal ellipsoid lens, and a Sérsic component for the background galaxy. Instead of removing foreground objects in a preprocessing step, their model is reconstructed together with the rest of the observation. As in the original analysis, additional Sérsic components are added to the foreground or background sources until the reconstruction is satisfactory. For this process, a model is considered detailed enough if there are no longer any systematic differences between observation and reconstruction. In practice, this choice leads to only one or two components for each visible object. For a more competitive analysis, one might choose the number and distribution of source components by some objective criterion [18, 19]. The available data is sky-subtracted, and because this process depends critically on the distinction between galaxy light and sky light, a flat sky component is added to account for possible uncertainties. Since the original reconstruction [11] forced the centre of the mass distribution to coincide with the centre of the foreground object for all lenses, the same assumption is used here for the sake of comparison. It is noted that such a restriction is not necessary for `LENSED` in order to recover robust lens models, as demonstrated in Chapter 7. Other parameters are left unconstrained. Visible but unrelated objects close to the lens are excluded from the analysis by suitably masking the uninteresting regions.

### 8.3 Reconstruction results

The results of the reconstruction of the 8 sample observations from the SLACS survey are given in Table 8.1. Apart from the lens parameters, the table lists the number of source components used for foreground and background galaxies, as well as the results of the original SLACS analysis. The two reconstruction efforts are in good agreement. The reconstructed images are shown in Figure 8.1. As seen from the images, LENSED is able to model all observed lensing events, regardless of complexity, signal-to-noise of the background images or overlap between the different sources. Some lens systems require particular care due to their peculiar properties; they are briefly described below, in order to show the capabilities of the algorithm and possible strategies for modelling non-trivial systems.

**SDSS J0808+4706.** This system was not modelled in the SLACS results due to the presence of a close-by companion to the main lensing galaxy. The system was qualitatively investigated as an example of a multi-component lens system, but without reconstruction [73]. With LENSED, two independent SIE components are used to model the main lensing galaxy and its companion. For the sources, two Sérsic components are used for the light distribution of the main lensing galaxy, one Sérsic component is used for the companion, and two Sérsic components for the background source. In total, the model has 35 free parameters, which is the highest number among the models of this chapter. Despite the complexity of the system, LENSED was able to explore the posterior distribution of the parameters, shown in Figure 8.2, and obtain reasonable results for the model. Of particular interest is the strong anti-correlation of the Einstein radii of the two lenses; this would not have been evident in a maximum-likelihood reconstruction method.

**SDSS J0822+2652.** The initial model allows for a very accurate reconstruction of the bright arc on the right, but the residuals clearly show a circular structure around the central galaxy. As this could be the signature of a second background component, one is added to the model, as in the original analysis [11]. The result is a significant improvement in the evidence of the reconstruction ( $\Delta \log \text{ev} \approx 800$ , Chapter 5.6). Quoted here are the results from this second model, although the possibility exists that the residuals in the first analysis are not due to a second background component but instead to a mismatch between the light profile for the central galaxy and the model. If this is the case, the favoured model is much more elliptical, with a recovered axis ratio of  $q_L = 0.6285 \pm 0.0089$ .

**Image plane priors for source positions.** In the case of SDSS J0728+3835 and SDSS J0841+3824, the foreground galaxy is not well enough reconstructed by one or two Sérsic components to reduce the significance of its residuals below that of the lensing signal. Therefore, with a completely free prior distribution for the position, the background source may be placed on top of the central galaxy to

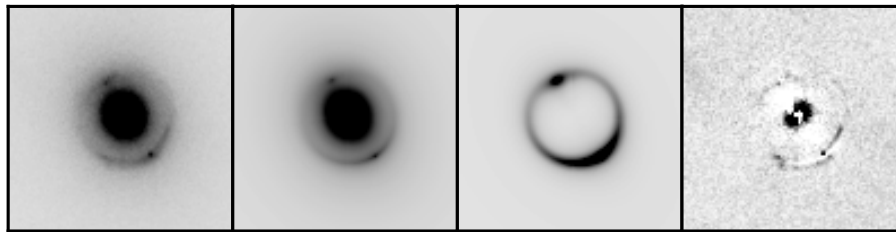
make up for the insufficiencies of the foreground model. This can be prevented by a better modelling of the foreground galaxy. However, a simple and efficient method is to use *image plane priors* for the background source positions. Instead of defining the prior distribution on the source plane, one can define a prior on the image plane for the position at which one of the images of the source is required to appear. Drawing from such a distribution is done in a straightforward way by first sampling a position on the image plane, mapping it to the source plane, and assigning it to the source. This is a “prior” in the true sense of the definition, as it uses an observer’s prior knowledge regarding the apparent position of an image for the distribution of possible source positions. The use of image plane priors reduces the correlations between lens and source parameters, as a source normally has to be repositioned any time the lens is updated to make the observed images appear once again where they are observed. At the same time, the parameter space volume of the source position is dramatically reduced, as the observed position is well constrained from the start.

**Summary.** The reconstructions of this section show that the forward method as implemented in `LENSED` is able to obtain robust and meaningful results from the analysis of real data, where uncertainties are much more severe than in tests on mock data (Chapter 7). The algorithm reliably reconstructs foreground sources, the deflecting lens, and lensed background sources at the same time. As in the case of mock data, no informative priors were used, and the analysis was, apart from the model choices described above, fully automatic. Intervention was required only due to inherent difficulties in the identification of lensing signatures, such as the circular residual in SDSS J0822+2652 and the poor counter-image in SDSS J0841+3824. These are peculiar cases that inevitably require some decision made by the modeller on the interpretation of the lensing event. In all cases in which there are clear signs of multiple images of the background source, `LENSED` is able to appropriately disentangle them from the light of the host galaxy, even in cases such as SDSS J0330-0020 and SDSS J0903+4116 in which there is significant overlap between the foreground and background light distributions.

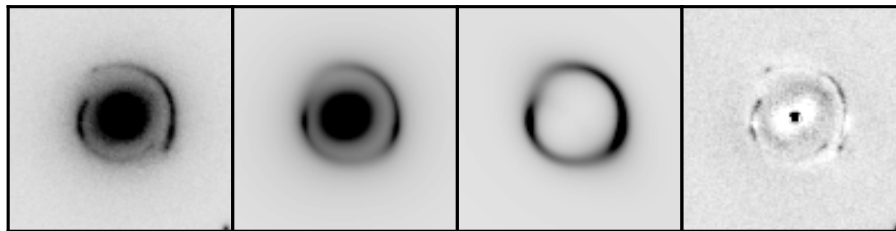
**Errors.** It should be clarified that the errors given in this analysis are of a purely statistical nature, and correspond to real uncertainties only in the ideal case in which the model used for lenses and sources offers a correct description of these objects. In the analysis of real data, this may not be true, and a change of model influences the recovered parameters possibly far beyond the errors quoted, which characterise the width of the distributions within a fixed model. Thus, if one wants to interpret the quoted values in an extensive way, an additional empirical error of the order of a few percent should be considered, as done in other works [11, 96].

| lens name                               | LENSED                    |                     |                     |                 |                  |                           | SLACS |                     |      |                     |                  |  |
|---|---------------------------|---------------------|---------------------|-----------------|------------------|---------------------------|-------|---------------------|------|---------------------|------------------|--|
|   | $b_{\text{SIE}}$ [arcsec] | $q$                 | P.A. [ $^{\circ}$ ] | $N_{\text{fg}}$ | $N_{\text{src}}$ | $b_{\text{SIE}}$ [arcsec] | $q$   | P.A. [ $^{\circ}$ ] | $q$  | P.A. [ $^{\circ}$ ] | $N_{\text{src}}$ |  |
| SDSS J0029-0055                         | $0.9603 \pm 0.0010$       | $0.8824 \pm 0.0020$ | $113.09 \pm 0.45$   | 1               | 1                | 0.96                      | 0.89  | 115.4               | 0.89 | 115.4               | 2                |  |
| SDSS J0252+0039                         | $1.0244 \pm 0.0006$       | $0.9226 \pm 0.0011$ | $16.07 \pm 0.47$    | 1               | 1                | 1.04                      | 0.93  | 16.2                | 0.93 | 16.2                | 3                |  |
| SDSS J0330-0020                         | $1.1012 \pm 0.0008$       | $0.8119 \pm 0.0032$ | $24.09 \pm 0.24$    | 1               | 1                | 1.10                      | 0.81  | 23.2                | 0.81 | 23.2                | 3                |  |
| SDSS J0728+3835                         | $1.2344 \pm 0.0014$       | $0.8958 \pm 0.0027$ | $159.80 \pm 0.62$   | 2               | 2                | 1.25                      | 0.85  | 157.6               | 0.85 | 157.6               | 4                |  |
| SDSS J0808+4706<br>( <i>companion</i> ) | $1.1699 \pm 0.0022$       | $0.7991 \pm 0.0019$ | $9.37 \pm 0.41$     | 2               | 1                | —                         | —     | —                   | —    | —                   | —                |  |
|   | $0.3335 \pm 0.0045$       | $0.9943 \pm 0.0024$ | $111.36 \pm 10.82$  | 1               | —                | —                         | —     | —                   | —    | —                   | —                |  |
| SDSS J0822+2652                         | $1.1081 \pm 0.0037$       | $0.9577 \pm 0.0095$ | $99.14 \pm 7.39$    | 1               | 2                | 1.17                      | 0.88  | 158.2               | 0.88 | 158.2               | 2                |  |
| SDSS J0841+3824                         | $1.3850 \pm 0.0024$       | $0.7831 \pm 0.0019$ | $171.42 \pm 1.02$   | 2               | 2                | 1.41                      | 0.79  | 1.4                 | 0.79 | 1.4                 | 2                |  |
| SDSS J0903+4116                         | $1.2911 \pm 0.0022$       | $0.8784 \pm 0.0038$ | $68.04 \pm 1.08$    | 1               | 1                | 1.29                      | 0.90  | 71.3                | 0.90 | 71.3                | 2                |  |

Table 8.1: Estimated parameters for the SIE lens models of 8 SLACS lenses from *HST* proposal 10886 [13]. The table compares the mean and standard deviation obtained from LENSED [103] with the SLACS lens modelling results [11]. The columns  $N_{\text{fg}}$  and  $N_{\text{src}}$  give the number of components used to model the foreground and background galaxies, respectively. East-of-north angles from the SLACS results have been changed to match the definition of LENSED. Dashed fields indicate that the lens has not been analysed.



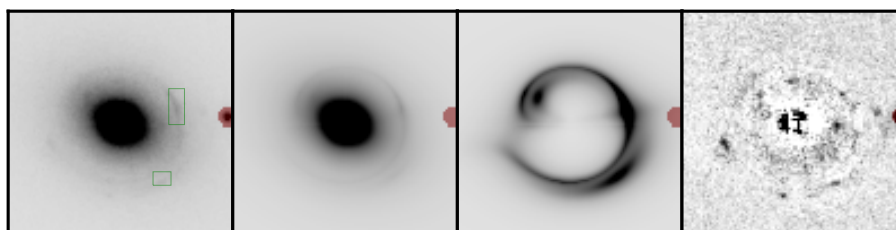
(a) SDSS J0029-0055



(b) SDSS J0252+0039

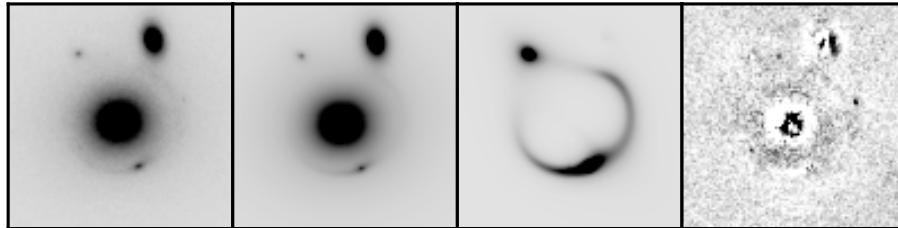


(c) SDSS J0330-0020

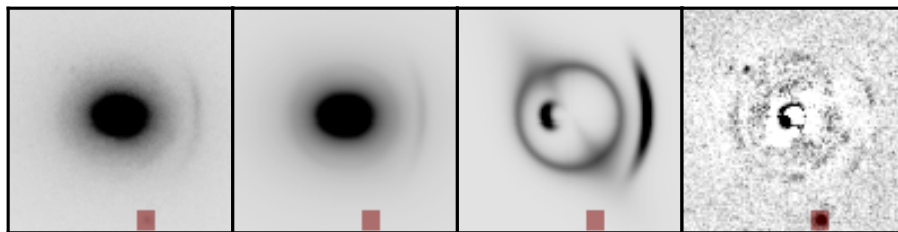


(d) SDSS J0728+3835

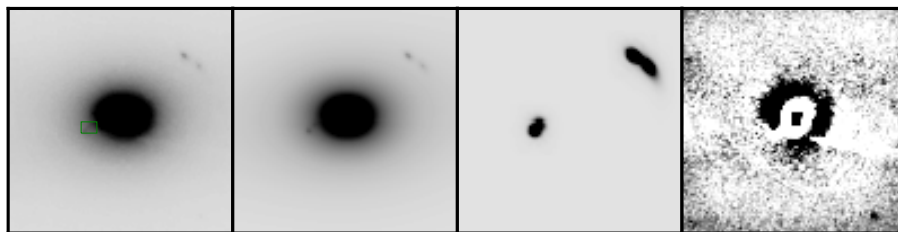
Figure 8.1: Reconstructions of SLACS observations from the  $F814W$  band. Each figure shows (*left to right*) the original observation, the maximum-likelihood model from LENSED, the lensed images of the background source only, and the residuals. Images are 5 arcsec by side, north up and east left. The scale ranges from  $-0.25 X$  (*white*) to  $X$  (*black*), where  $X$  is set to the 97th percentile value of the recovered model for the first and second image, and the 99th percentile value of the lensed background source for the third and fourth image. This matches the figures of Bolton et al. [11]. Overlays show masked regions (*red*) or image plane priors (*green*) if used during the reconstruction.



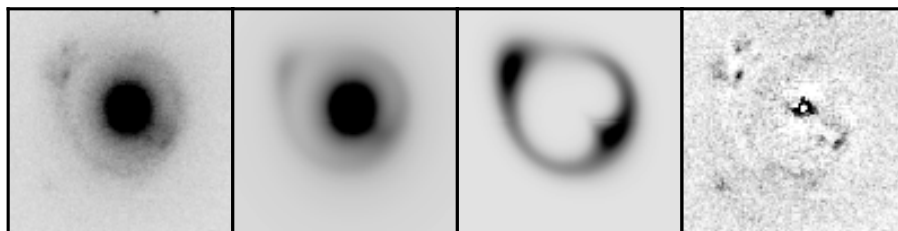
(e) SDSS J0808+4706



(f) SDSS J0822+2652



(g) SDSS J0841+3824



(h) SDSS J0903+4116

Figure 8.1: Continued.

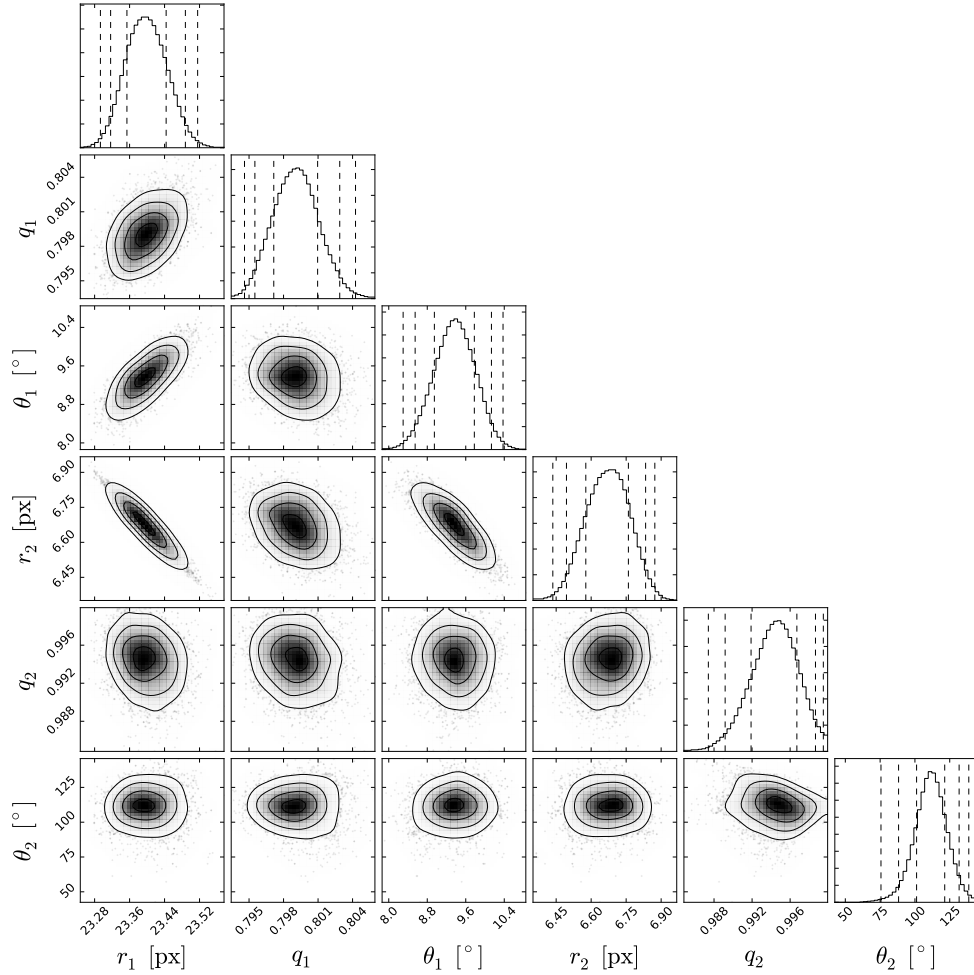


Figure 8.2: Lens parameter constraints for the model of SDSS J0808+4706, which contains a galaxy and a close-by companion. The galaxies are modelled as SIEs at the same redshift. The model contains a total of 35 free parameters, including the foreground and background source components. The plot shows the marginal posterior distributions for the lens parameters, with contours and dashed lines indicating the 68%, 95%, and 99% confidence regions, respectively.

## 9 Application: Flexible lens modelling

### 9.1 Modelling individual lenses

Instead of finding the distribution of parameters for a single model over many observations, the forward reconstruction method is also uniquely adapted for the analysis of a single observations with multiple competing models. Composition of individual lens and source components allows for a great amount of control over the model and the reconstruction, which in turn leads to greater confidence in the results with respect to non-parametric, free-form models. Since a modern implementation of the forward method such as `LENSED`, which incorporates all of the optimisations presented in this work, performs a complex reconstruction in a matter of hours — and often minutes — the process is fast enough to allow the user to play with many different models in a short amount of time, and thus explore the lens system more thoroughly than possible with a method that takes several days for each reconstruction. This often leads to an intuitive understanding of the lens system and the individual multiple images of the background source, which appear, disappear or move as components are added or removed from the model. Finally, the particular implementation of `LENSED` has the additional benefit that new lens models can be developed quickly — often in a matter of minutes — and added without any changes to the algorithm or even recompilation. This makes it possible to quickly design specific lens models for a single observation, instead of having to rely on the default selection that comes with the implementation. All of these features will now be demonstrated in a sample analysis of a particular gravitational lens system.

**The Cosmic Horseshoe.** The spectacular gravitational lens shown in Figure 9.1 is known as the “Cosmic Horseshoe”. First discovered [8] in ground-based data from SDSS Data Release 5 as SDSS J1148+1930, the lens system features a nearly complete Einstein ring ( $\approx 300^\circ$ ) with a very large diameter ( $\approx 10''$ ). Spectroscopy revealed the redshifts of lens and source to be 0.444 and 2.379, respectively, and the measured velocity dispersion  $\sigma_v > 400$  km/s made the Cosmic Horseshoe “the most massive galaxy lens hitherto discovered” [8]. As CSWA 1, the lens system was one of the founding entries in the CASSOWARY catalogue [20]. The lens system was later observed by *HST* under proposal 11602 [2], and high resolution images in

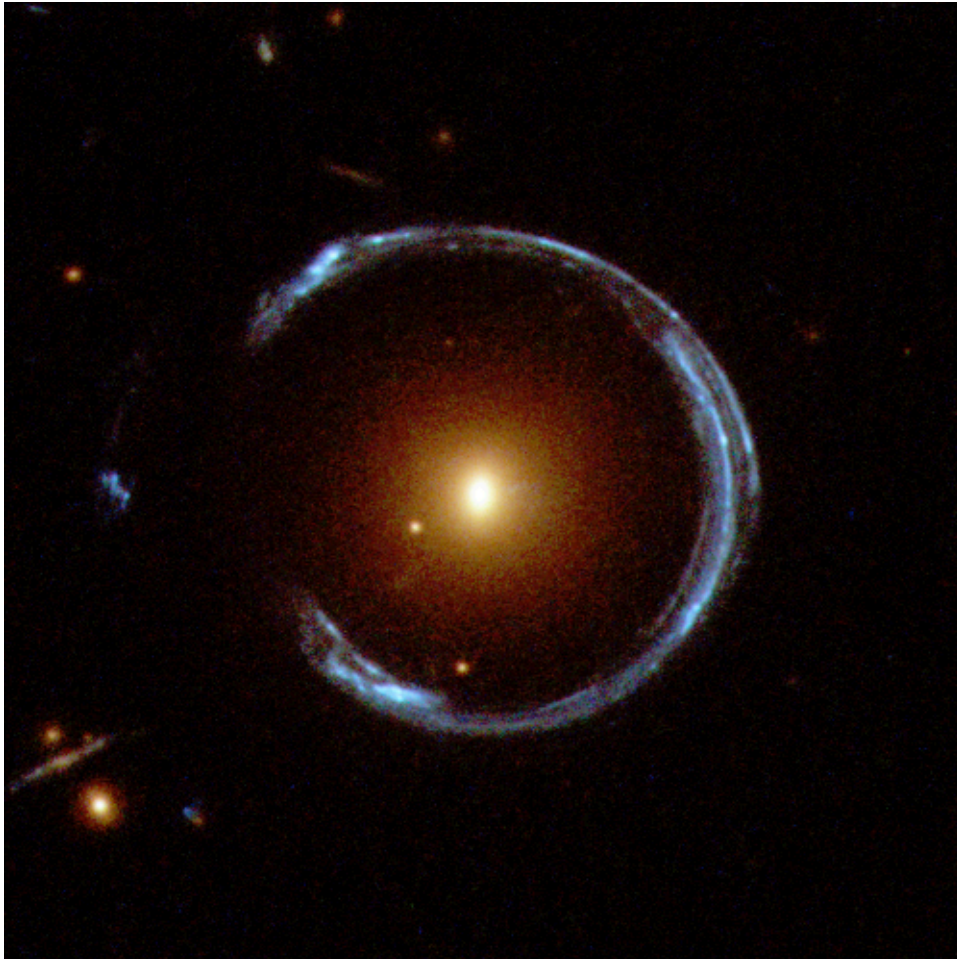


Figure 9.1: The “Cosmic Horseshoe” CSWA 1 as observed by *HST*. The lens system consists of a  $z = 0.444$  luminous red galaxy in the foreground lensing a  $z = 2.379$  star-forming background galaxy, creating an almost perfect Einstein ring ( $\approx 300^\circ$ ) with a very large diameter ( $\approx 10''$ ). With a spectroscopically measured velocity dispersion of  $\sigma_v = 430 \pm 50$  km/s, this is the most massive galaxy lens observed. The colour image is a composition of the optical *B* (blue), optical *V* (green) and infrared *I* (red) bands from Hubble’s Wide Field Camera 3.

Image credit: *ESA/Hubble & NASA*

the *F475W*, *F606W* and *F814W* bands are freely available from the Hubble Legacy Archive [44].

**Existing models.** The Cosmic Horseshoe has been analysed with a diverse set of astronomical tools. Although the discovery by Belokurov et al. [8] does not include a reconstruction, the reported velocity dispersion  $\sigma_v = 430 \pm 50$  km/s can be used to construct an equivalent singular isothermal sphere (SIS) model. This is useful for an independent comparison of the subsequent lens modelling efforts. A follow-up observation by Dye et al. [30] using data obtained with the *Isaac Newton Telescope (INT)* contains the comparative reconstruction of the obtained data with three different models — singular isothermal ellipsoid (SIE), Navarro, Frenk and White (NFW), and elliptical power law (EPL) — each with and without external shear. Instead of the forward method, the reconstruction uses lens inversion with an adaptive source grid [29, 114]. Hence this set of results allows for an external check of the forward method across reconstruction methods. There have been a number of subsequent spectroscopic investigations of the Cosmic Horseshoe’s high-redshift background source<sup>1</sup> [43, 46, 59, 81, 84, 98]. Spiniello et al. [98] and Agnello, Auger and Evans [1] give estimates for the slope of a power law mass density profile, which can be compared to results from lens modelling. The only further direct lens reconstruction of the Cosmic Horseshoe, among a number of other CASSOWARY lenses, was performed by Kostrzewa-Rutkowska et al. [55] using the original SDSS data and a SIE model. They remark that the low quality of the data did not allow for the estimation of the slope of an EPL model. It is curious that there does not appear to be a single reconstruction to date which utilises the high resolution follow-up observations done by *HST*.

The existing results are compiled in Table 9.1. For comparison purposes, all parameters have been converted to the definitions of Chapter 3 and 4. Some of the results require a non-trivial transformation of the reported constraints to the new definitions. This is done by sampling a large number of parameter values from an independent set of normal distributions with the given mean and standard deviation in each parameter, performing the transformation, and then computing the statistics of the updated results. It should be noted that this ignores possible correlations in the original distributions of the parameter values, which might alter some of the error bounds.

**Methodology.** In the following, a number of different reconstructions of the Cosmic Horseshoe are presented. Each reconstruction is performed using the LENSED algorithm with default settings [103]. The data is a *HST* observation from proposal I1602 [2] in the *F475W* band, which consists of six exposures with a total exposure time of 5454 seconds. Images were obtained from the Hubble Legacy Archive [44], which provides cleaned, drizzled and aligned science products. The resolution of the data is  $\sim 0.04$  arcsec/pixel. From the large field of view, a region

---

<sup>1</sup>Which was subsequently found to be at a slightly larger redshift of  $z \approx 2.381$ .

| lens           | source   | from | data | $b$ [arcsec]            | $t$                  | $q$                  | $\theta$ [°]      | $\gamma$          | $\theta_\gamma$ [°] |
|----------------|----------|------|------|-------------------------|----------------------|----------------------|-------------------|-------------------|---------------------|
| SIS *          | —        | [8]  | —    | $3.79 \pm 0.87^*$       | (1)                  | (1)                  | —                 | —                 | —                   |
| SIE            | —        | [30] | INT  | $4.99 \pm 0.12^\dagger$ | (1)                  | $0.76 \pm 0.03$      | $46.5 \pm 2.7$    | —                 | —                   |
| SIE + $\gamma$ | —        | [30] | INT  | $4.98 \pm 0.08^\dagger$ | (1)                  | $0.81 \pm 0.02$      | $49.8 \pm 2.7$    | $0.017 \pm 0.005$ | $38.2 \pm 9.4$      |
| EPL            | —        | [30] | INT  | $4.96 \pm 0.26^\dagger$ | $0.96 \pm 0.02$      | $0.78 \pm 0.03$      | $49.2 \pm 3.0$    | —                 | —                   |
| EPL + $\gamma$ | —        | [30] | INT  | $5.08 \pm 0.27^\dagger$ | $0.95 \pm 0.02$      | $0.83 \pm 0.02$      | $50.8 \pm 3.1$    | $0.020 \pm 0.005$ | $37.7 \pm 8.6$      |
| EPL ‡          | —        | [98] | —    | —                       | $0.72^{0.05}_{0.06}$ | —                    | —                 | —                 | —                   |
| EPL ‡          | —        | [1]  | —    | —                       | $0.76 \pm 0.08$      | —                    | —                 | —                 | —                   |
| SIE + $\gamma$ | 1 Sérsic | [55] | SDSS | $5.08 \pm 0.02$         | (1)                  | $0.89^{0.03}_{0.04}$ | $40 \pm^{8}_{14}$ | $0.021 \pm 0.012$ | $-14 \pm^{19}_{13}$ |

Table 9.1: Comparison of existing reconstructions of the Cosmic Horseshoe CSWA 1. For a summary of the individual results given here see text. Models include singular isothermal ellipsoids (SIE), Navarro, Frenk and White profiles (NFW), and elliptical power law profiles (EPL). Some models contain an external shear component ( $+$   $\gamma$ ). SIS models are a special case of SIE models with fixed axis ratio  $q = 1$ . SIE models are a special case of EPL models with fixed slope  $t = 1$ . One model features a parametric background source with a Sérsic profile. Listed parameters are the model-dependent scale length  $b$ , power law slope  $t$ , axis ratio  $q$ , position angle  $\theta$  measured counterclockwise from the positive  $x$ -axis, magnitude of the external shear  $\gamma$ , and direction of the external shear  $\theta_\gamma$ . All parameters have been changed to the definitions in the text.

\* The SIS model was not originally reconstructed; instead, values are calculated from the quoted velocity dispersion  $\sigma_v = 430 \pm 50$  km/s [8].

† The distribution for the scale length is sampled from the given distributions of  $k_0$  and  $q$ , which ignores possible correlations.

‡ These results were obtained from spectroscopic or kinematic observations.

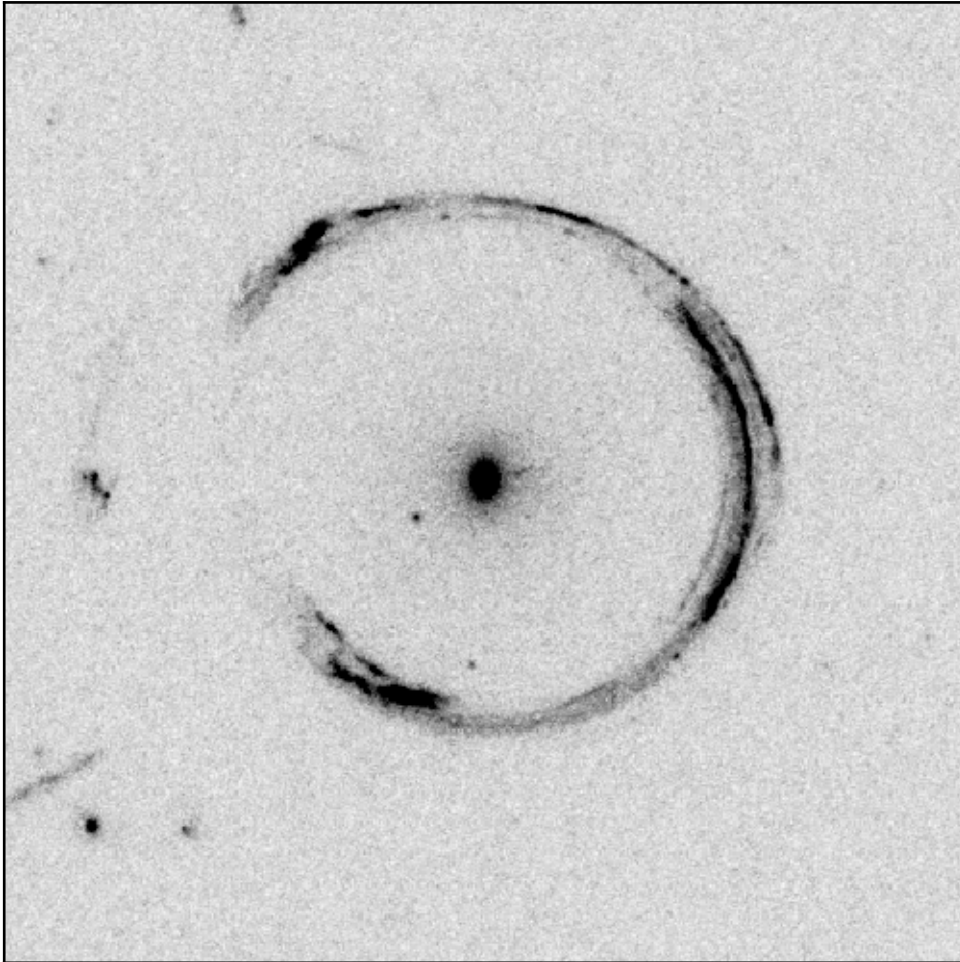


Figure 9.2: *HST* observation of CSWA 1 in the *F475W* band, with north up and east left. Shown is a  $470 \times 470$  pixel ( $18.6 \times 18.6$  arcsec) region centred on the lens system and used for reconstruction. The image consists of 6 exposures with a total exposure time of 5454 seconds.

of  $470 \times 470$  pixels ( $18.6 \times 18.6$  arcsec) centred on the lens system is selected for reconstruction. The resulting input is shown in Figure 9.2. A variance map for the image is generated by LENSED. No pixels in the selected region are masked or otherwise excluded.

**Lens and foreground models.** This reconstruction uses two lens models: the singular isothermal ellipsoid lens (SIE, Chapter 3) and the elliptical power law lens (EPL, Chapter 4). It shall be noted that the former is a special case of the latter, and corresponds to a fixed slope  $t = 1$ . For each model, an external shear component might be added to the reconstruction. Non-informative and uniform priors are used for all parameters.

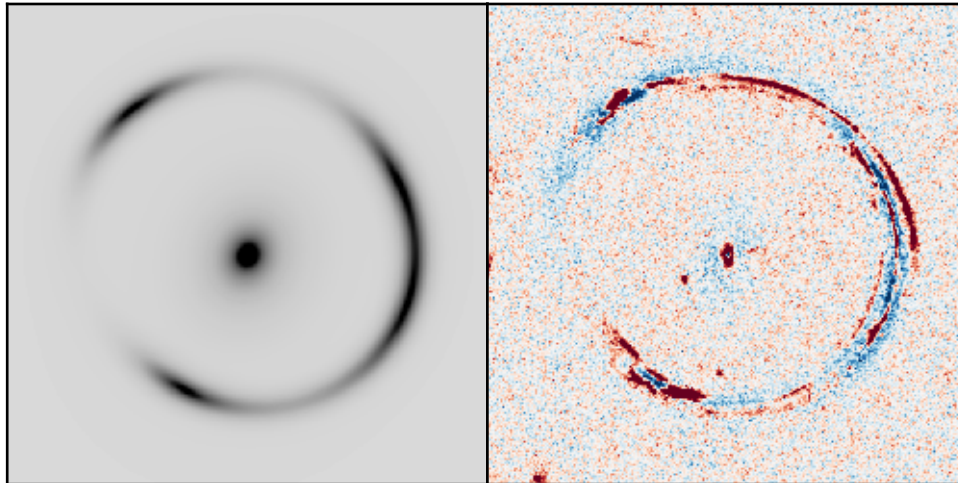
The central foreground galaxy is modelled in all cases by a parametric source containing a single Sérsic component. A further flat sky component is added to the foreground to account for diffuse light. For both foreground sources (the central galaxy and the flat sky), the priors of the parameters are non-informative uniform distributions over the whole range of sensible values.

**Background source models.** In contrast to the reconstruction by Dye et al. [30], the background source is a parametric model in this analysis using the forward method. For a qualitative investigation of the effect of the number of background components on the results, each of the lens models is subsequently reconstructed using 1, 2 and 4 individual Sérsic components. The source positions are uniformly distributed within regions that correspond to their eventual image positions, but which are nevertheless large enough to be considered non-informative priors. All other parameters are left free as usual.

## 9.2 Singular isothermal models

The reconstruction of the Cosmic Horseshoe CSWA 1 using a singular isothermal ellipsoid, with and without external shear, and different numbers of background Sérsic components, is shown in Figure 9.3. The SIE model is a reliably good fit to the observation, and in no case did the reconstruction fail. The model with only one background source component (Figure 9.3a, b) produces a smooth model of the Cosmic Horseshoe that is very similar in appearance to the original SDSS and *INT* observations. The results in this case, shown in Table 9.2, are therefore in good agreement with existing values from low-resolution data [30, 55]. Going to models that contain background source substructure in the form of additional Sérsic components, the higher resolution of the data has a clear differentiating effect on models with and without shear.

**The effect of external shear on multiple components.** If more components are added to the background source model, the external shear has a visible effect on the reconstructed images. With two components (SIE + 2 Sérsic, Figure 9.3c, d),



(a) SIE + 1 Sérsic

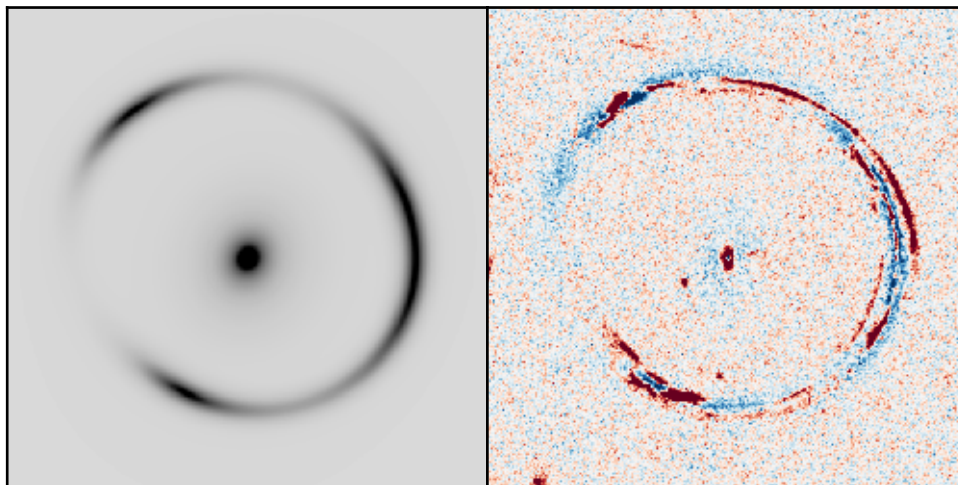
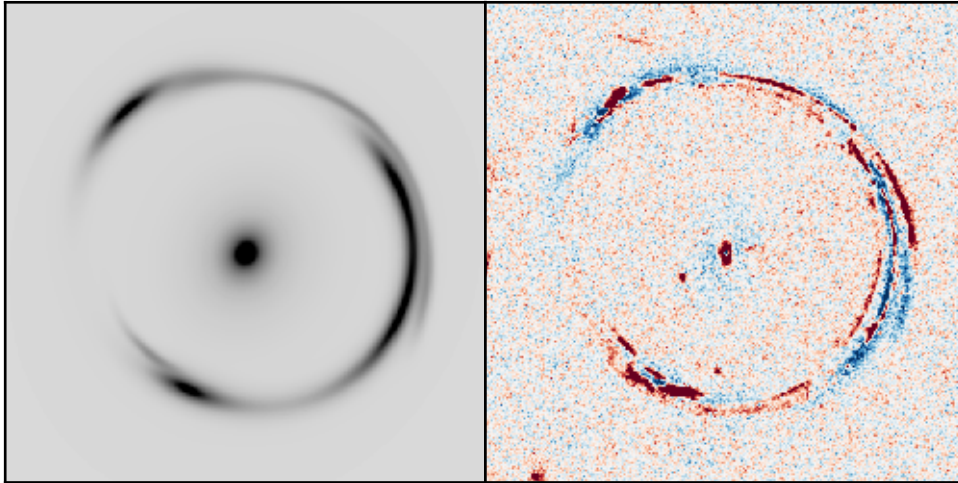
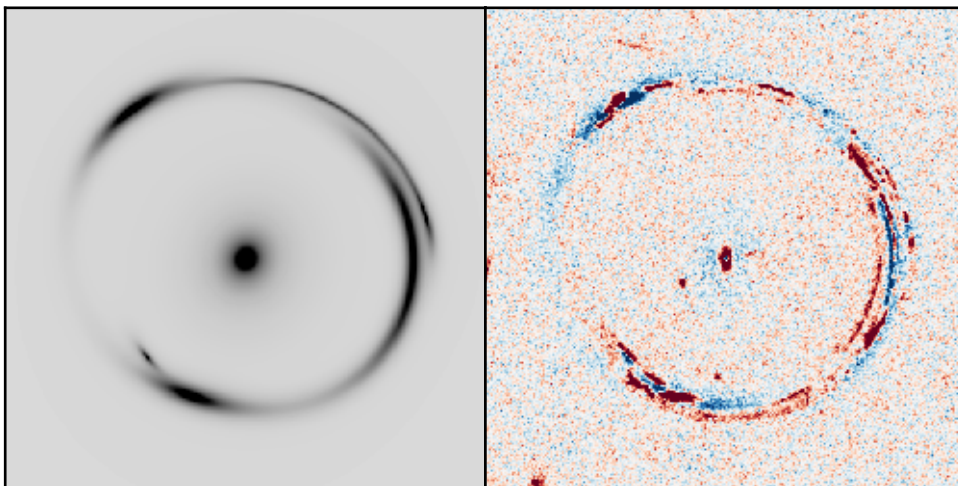
(b) SIE +  $\gamma$  + 1 Sérsic

Figure 9.3: Singular isothermal ellipsoid (SIE) models of CSWA 1. Shown are the maximum-likelihood reconstructions and residuals for models without and with shear ( $+\gamma$ ) and different numbers  $n$  of Sérsic components ( $+n$  Sérsic) of the lensed background source. All images use the same scale. The residual images show overcompensation of the model in blue, and uncompensated light in red.

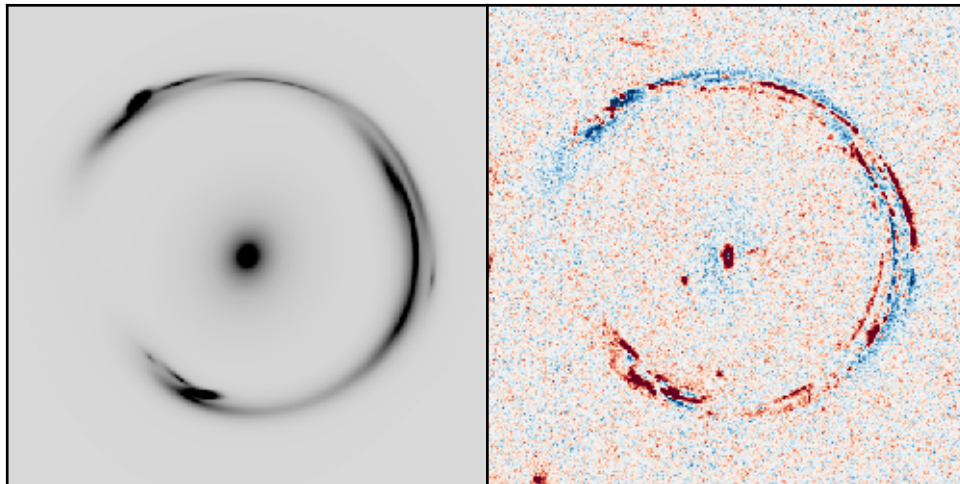


(c) SIE + 2 Sérsic

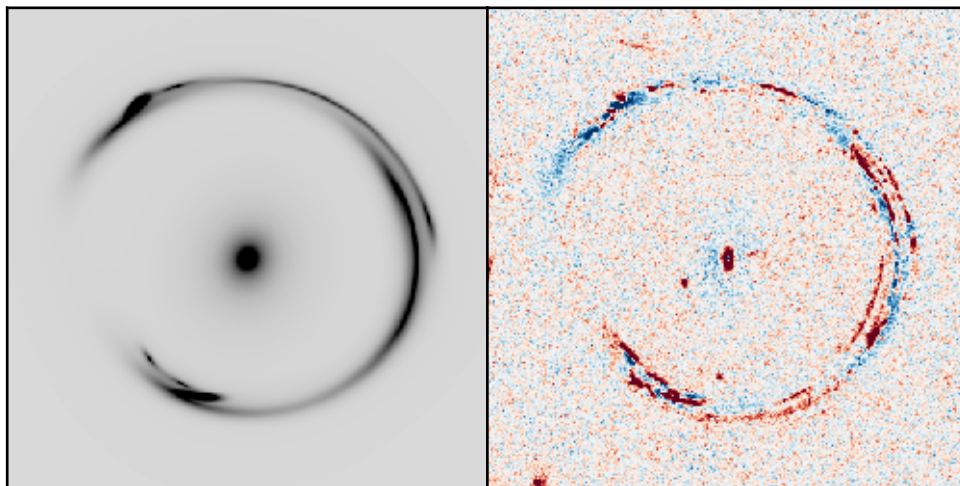


(d) SIE +  $\gamma$  + 2 Sérsic

Figure 9.3: Continued.



(e) SIE + 4 Sérsic



(f) SIE +  $\gamma$  + 4 Sérsic

Figure 9.3: Continued.

the shear allows for the correct reproduction of the curvature over much of the observed arc. It also correctly localises the second lane of the ring on the right, which goes too far down in the reconstruction without shear, and does not show the observed peak in the surface brightness distribution. This correction of the right-hand arc results in the correct reconstruction of the compact counter-image on the bottom left, which is only correctly reproduced with shear. All of these effects are clearly discernible in the residual images.

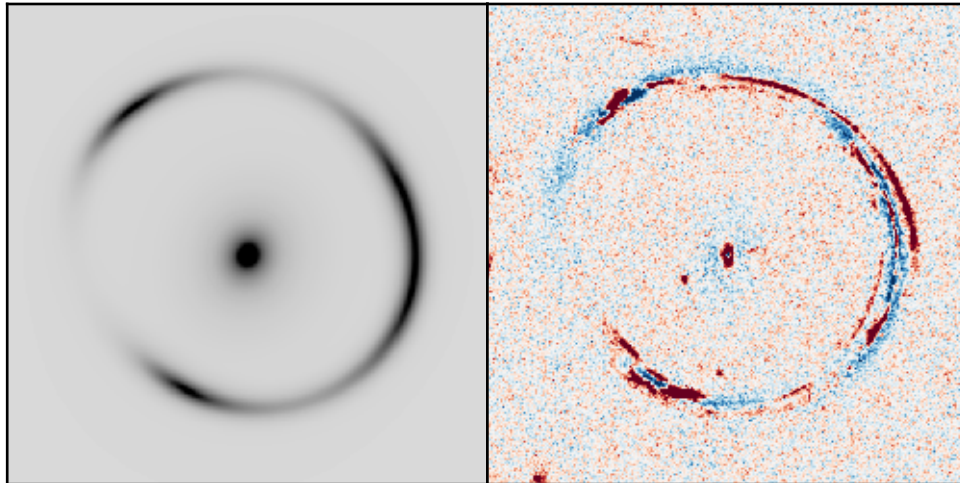
For four source components, the observed effect is similar (SIE + 4 Sérsic, Figure 9.3e, f). The two small and compact images on the bottom left are now correctly placed even without shear, but the residuals show that their counter-images on the right-hand arc do not correctly reproduce the surface brightness distribution of the observation, in particular regarding the location of the two maxima. By adding shear, the situation is remedied in the same way as before.

That the shear has a definite and significant impact on the reconstruction is represented well in the results of Table 9.2, as the magnitude  $\gamma$  of the shear with multiple source components is twice as big as in the case of a single background component, but almost unchanged between 2 and 4 Sérsic components, and here the orientation agrees to within  $5^\circ$  as well.

**Additional background source components.** In reconstructions with external shear (SIE +  $\gamma$ ), the subsequent addition of background components to the model beautifully highlights the constructive nature of the forward method. Each new source component resolves one of the multiple images in the observation, and each model results in a progressively better reconstruction (Figure 9.3b, d, f). This direct, step-by-step reconstruction of the observed image, in combination with the accompanying convergence of the lens parameters, is a good validation of the results and the forward method in general.

### 9.3 Power law models

The elliptical power law (Chapter 4) models of the Cosmic Horseshoe show a clear preference for less-than-isothermal slopes (Table 9.2), in disagreement with the original reconstruction [30]. Even in the case of a model with no background source substructure and no shear (EPL + 1 Sérsic, Figure 9.4a), the combination of power law slope  $t \approx 0.67$  and axis ratio  $q \approx 0.89$  reconstructs the curvature of the ring much better than the equivalent SIE model (SIE + 1 Sérsic, Figure 9.3a). There is also tension between lens reconstruction and results for the power law slope obtained by Spiniello et al. [98] and Agnello, Auger and Evans [1], and only the simplest model of EPL + 1 Sérsic is anywhere near agreement. As soon as the background source contains resolved substructure, much flatter than isothermal profiles with  $t \lesssim 0.5$  are preferred.



(a) EPL + 1 Sérsic

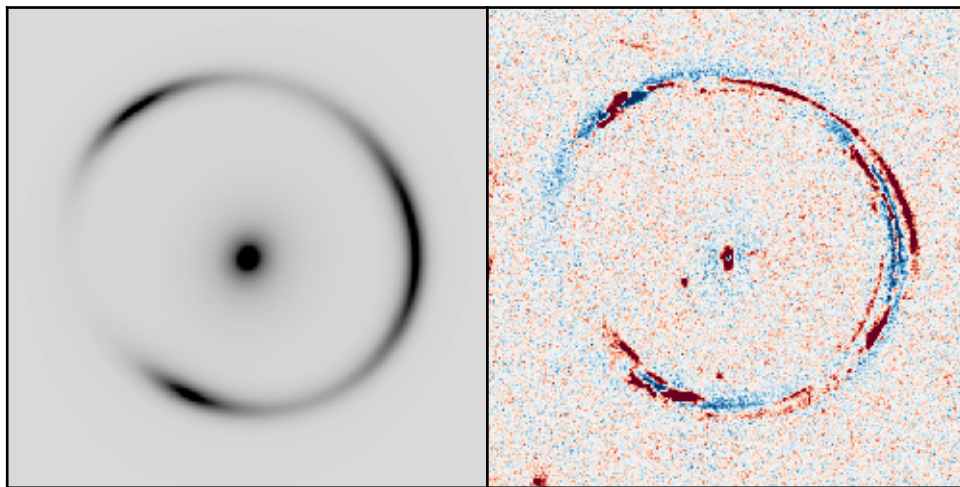
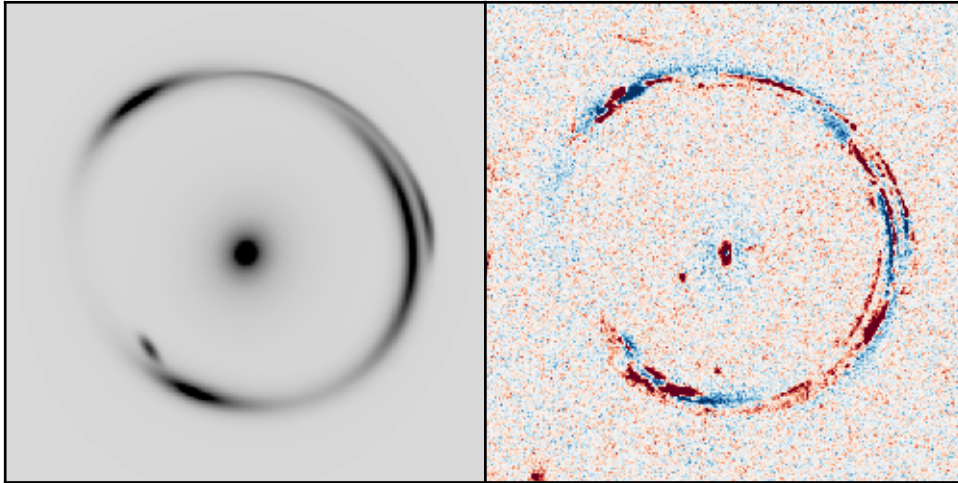
(b) EPL +  $\gamma$  + 1 Sérsic

Figure 9.4: Elliptical power law profile (EPL) models of CSWA 1. Shown are the maximum-likelihood reconstructions and residuals for models without and with shear ( $+\gamma$ ) and different numbers  $n$  of Sérsic components ( $+n$  Sérsic) of the lensed background source. All images use the same scale. The residual images show overcompensation of the model in blue, and uncompensated light in red.



(c) EPL + 2 Sérsic

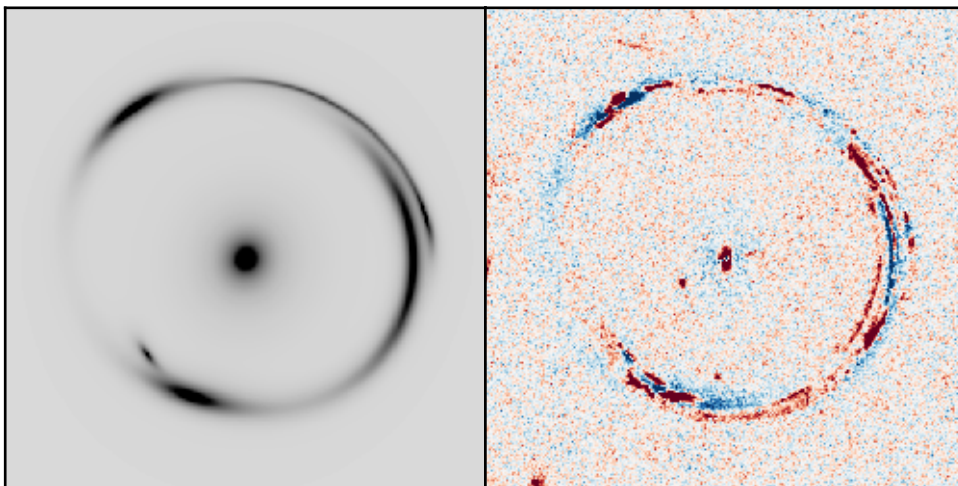
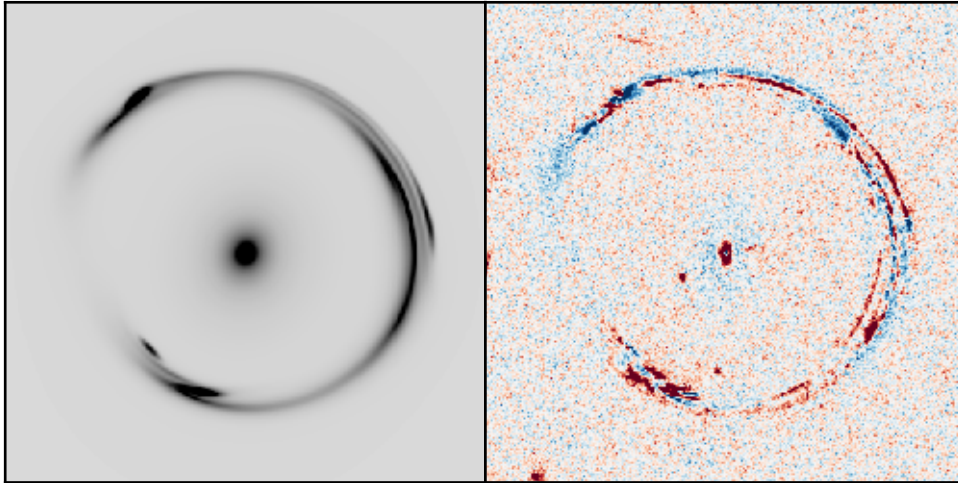
(d) EPL +  $\gamma$  + 2 Sérsic

Figure 9.4: Continued.



(e) EPL + 4 Sérsic

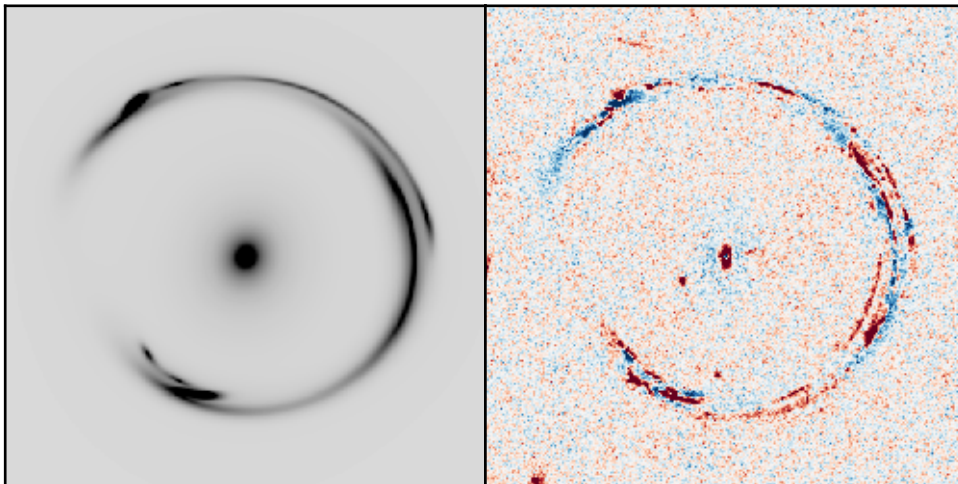
(f) EPL +  $\gamma$  + 4 Sérsic

Figure 9.4: Continued.

**The interplay of shear and power law slope.** The results of Table 9.2 show that models with external shear feature a systematically lower slope of the power law, even though the magnitude of the shear is comparable to that of the respective SIE models. However, a significant difference is found in the direction of the shear. For a future analysis of the results, it will be necessary to investigate the environment of the Cosmic Horseshoe and identify realistic sources of external shear. This can subsequently be incorporated into a prior distribution on the direction of the shear, and will hopefully align the results of separate models more closely than in this demonstration.

#### 9.4 Summary of the results

The results of all reconstructions performed here are listed in Table 9.2. They demonstrate the power of the forward reconstruction method to model complex lenses with a relatively small number of simple lens and source components, even for highly-resolved data which contains a lot of difficult to reproduce substructure in the surface brightness distribution. The results further show that this amount of detail in the data can be necessary: Dye et al. [30] noted that external shear was curiously missing from the reconstruction, since the observed Einstein ring is practically circular. With more resolved observations from *HST*, this is no longer the case, and the former result can be understood as a sort of degeneracy between the ellipticity of the lens and the external shear, which here is broken as soon as substructure is added to the background source.

A final reconstruction of the Cosmic Horseshoe is shown in Figure 9.5. The model consists of an EPL lens and 6 Sérsic components for the lensed background source, for a total of 56 free parameters. With this model, all of the visible source substructure of the Cosmic Horseshoe is reproduced, including the faint inner lane of the right-hand arc. At the same time, the recovered lens parameters are not significantly different from the same reconstruction with 4 Sérsic components, and it is reasonable to assume that the result truthfully represents the best model of the Cosmic Horseshoe to date.

| lens           | source   | $b$ [arcsec]        | $t$                 | $q$                 | $\theta$ [°]     | $\gamma$            | $\theta_\gamma$ [°] |
|----------------|----------|---------------------|---------------------|---------------------|------------------|---------------------|---------------------|
| SIE            | 1 Sérsic | $5.1030 \pm 0.0006$ | (1)                 | $0.7710 \pm 0.0006$ | $49.50 \pm 0.06$ | —                   | —                   |
| SIE + $\gamma$ | 1 Sérsic | $5.0865 \pm 0.0007$ | (1)                 | $0.8533 \pm 0.0017$ | $40.82 \pm 0.36$ | $0.0279 \pm 0.0006$ | $-20.75 \pm 0.52$   |
| SIE            | 2 Sérsic | $5.0940 \pm 0.0005$ | (1)                 | $0.7583 \pm 0.0004$ | $49.02 \pm 0.05$ | —                   | —                   |
| SIE + $\gamma$ | 2 Sérsic | $5.0739 \pm 0.0009$ | (1)                 | $0.8518 \pm 0.0015$ | $21.81 \pm 0.21$ | $0.0565 \pm 0.0003$ | $-14.62 \pm 0.26$   |
| SIE            | 4 Sérsic | $5.1034 \pm 0.0003$ | (1)                 | $0.7668 \pm 0.0004$ | $51.34 \pm 0.03$ | —                   | —                   |
| SIE + $\gamma$ | 4 Sérsic | $5.0858 \pm 0.0005$ | (1)                 | $0.8308 \pm 0.0010$ | $26.28 \pm 0.16$ | $0.0536 \pm 0.0003$ | $-10.06 \pm 0.17$   |
| EPL            | 1 Sérsic | $5.0887 \pm 0.0007$ | $0.6698 \pm 0.0079$ | $0.8858 \pm 0.0021$ | $50.50 \pm 0.08$ | —                   | —                   |
| EPL + $\gamma$ | 1 Sérsic | $5.1173 \pm 0.0005$ | $0.1181 \pm 0.0015$ | $0.9093 \pm 0.0008$ | $37.47 \pm 0.25$ | $0.0391 \pm 0.0004$ | $34.78 \pm 0.29$    |
| EPL            | 2 Sérsic | $5.0904 \pm 0.0004$ | $0.2998 \pm 0.0046$ | $0.9604 \pm 0.0007$ | $51.63 \pm 0.04$ | —                   | —                   |
| EPL + $\gamma$ | 2 Sérsic | $5.1020 \pm 0.0004$ | $0.1300 \pm 0.0014$ | $0.8952 \pm 0.0005$ | $21.67 \pm 0.12$ | $0.0492 \pm 0.0003$ | $17.54 \pm 0.14$    |
| EPL            | 4 Sérsic | $5.0952 \pm 0.0003$ | $0.5020 \pm 0.0047$ | $0.9274 \pm 0.0009$ | $52.88 \pm 0.04$ | —                   | —                   |
| EPL + $\gamma$ | 4 Sérsic | $5.1027 \pm 0.0003$ | $0.3624 \pm 0.0025$ | $0.8780 \pm 0.0004$ | $26.79 \pm 0.08$ | $0.0455 \pm 0.0002$ | $14.96 \pm 0.15$    |
| EPL + $\gamma$ | 6 Sérsic | $5.1002 \pm 0.0003$ | $0.3591 \pm 0.0034$ | $0.8798 \pm 0.0005$ | $25.81 \pm 0.09$ | $0.0456 \pm 0.0002$ | $13.96 \pm 0.17$    |

Table 9.2: Reconstruction results of the Cosmic Horseshoe CSWA 1 using the forward method implemented in LENSED. The applied lens models are the singular isothermal ellipsoid (SIE) and the elliptical power law (EPL). Lens models may contain an external shear component (+  $\gamma$ ). SIE models are a special case of EPL models with fixed slope  $t = 1$ . The number  $n$  of Sérsic components used for the background source varies between the reconstructions. Listed parameters are the model-dependent scale length  $b$ , power law slope  $t$ , axis ratio  $q$ , position angle  $\theta$  measured counterclockwise from the positive  $x$ -axis, magnitude of the external shear  $\gamma$ , and direction of the external shear  $\theta_\gamma$ .

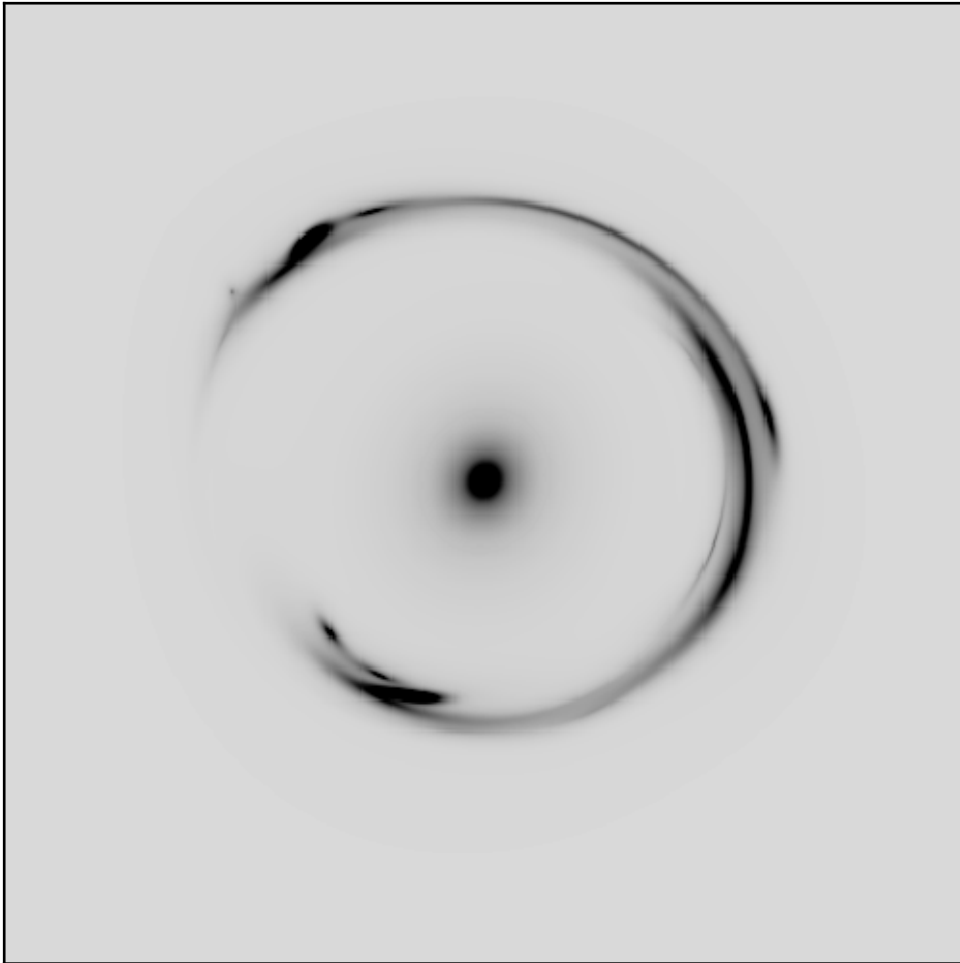


Figure 9.5: The final reconstruction of the Cosmic Horseshoe CSWA 1. The model consists of an EPL lens and 6 Sérsic components for the lensed background source. In this reconstruction, all of the major details of the observation are reproduced.

## 10 Conclusion

This thesis has developed the forward method for lens reconstruction and applied it to a number of select problems. The forward method, presented in Chapter 5, offers conceptual simplicity in the creation of models for observations of strong lenses and allows for a clear interpretation of the results of a reconstruction for both lenses and sources. It is furthermore a uniquely adapted tool for testing new analytical models of lenses and — eventually — sources at higher redshifts than otherwise accessible.

There are however a number of challenges that must be overcome before any implementation of this reconstruction method can be realised. The first lies in the simulation of the lens model, which is the numerical integration of the surface brightness distribution for each observed pixel, and therefore a computationally intensive task, especially in modern space-based observations of large arcs with high resolution. Secondly, the parameter space of the combined lens and source model is usually high-dimensional and moderately to highly degenerate, making a straightforward sampling very difficult. Chapter 6 contains a number of solutions to the most severe of these problems as implemented in the LENSED algorithm, but which are generally applicable and useful for any implementation of a lensing pipeline. By carefully rewriting the necessary calculations in a massively parallel fashion, it is possible to harness the multiprocessing capabilities of modern GPUs and maximise the efficiency of the lens reconstruction code. The resulting increase in computational speed allows for a precise simulation of the expected image of a model, even using numerical quadrature for each individual pixel, and still test thousands of individual parameter settings per second. Combining the fast and accurate simulation with a modern library for Bayesian analysis makes it possible to achieve a true sampling of the system's parameter space in reasonable time.

Chapter 7 contains the tests performed to ensure that the forward method, and LENSED in particular, is working as expected. This is done by analysing a fixed lens model in an ensemble of 100 mock images containing randomised sources. By recovering lens parameters in a setting where the mock data can be reconstructed exactly, it is possible to show that the method has no intrinsic biases. This remains true after generating mock observations with more complex background sources based on real galaxies, which therefore cannot be modelled exactly. Subsequent analysis shows that the lens parameters are still very well constrained, to a degree

far beyond the uncertainties that arise from the modelling of the systems. Thus it is demonstrated that in lens reconstruction applications, the quality of the results is not limited by either the forward method or the particular algorithm used for the reconstruction.

A further set of tests shows that the forward method is also uniquely adapted for studying the properties of lensed background sources. Repeating the above tests, this time with focus on the source parameters, it could be shown that the results are nearly invariant under the influence of the lens. This means that sources return the same set of parameters when reconstructed through a lens as if they had been observed directly, but with the effective magnification that the lens provides.

The implementation of the forward method in `LENSED` is used to analyse a number of real observations in Chapter 8. The data originates from the SLACS survey [10, 11] and has been previously analysed there with a similar method. This is an opportunity to compare different implementations of the forward method, highlight possible differences and their origins, and verify that the techniques presented here lead to acceptable results. Overall, the results agree very well with the previously published ones. At the same time, this experiment showcases how `LENSED` can be used in practise.

In a second application, `LENSED` is used in Chapter 9 to analyse the “Cosmic Horseshoe” CSWA 1. This is a spectacular, almost complete Einstein ring ( $\sim 300^\circ$ ) with large diameter ( $\sim 10''$ ), and one of the most massive galaxies observed. Using models and the reconstruction method presented here, it was possible to show that the high resolution data from *HST* contains information about the lens model and its environment (in the form of shear) which has not been accessible in earlier reconstructions with different methods. The final result of this application is an impressive reconstruction that reproduces even small details of the observation with only a handful of simple, parametric models.

**Future applications.** It will be interesting to extend the example demonstrations given here to a full analysis. In the first case, one of the major SLACS results is that the mass density profile across the population of lenses is approximately isothermal. This could be verified with moderate effort using `LENSED` and the elliptical power law profile lens presented here. In the second case of the “Cosmic Horseshoe”, a careful analysis of the environment of the galaxy can provide a prior constraint on the admissible external shear of the lens model. If, once the shear is realistically constrained, the resulting power law slope remains considerably flatter than isothermal, i.e.  $t < 1$  or even  $t < 0.5$ , this could be a powerful indicator of a possible dark, flat component to the lens.

**Extension of the method.** There are a number of conceivable extensions to the forward method in its current form. One such extension the treatment of multi-plane lensing [78], and the `LENSED` algorithm in particular was designed with this

goal in mind. This would be useful for gravitational lens systems which contain images from sources at different redshifts, such as the so-called “Jackpot” lens [40].

Another possible extension is the simultaneous reconstruction of observations in multiple bands, similar to the GALFITM [112] extension to GALFIT [75, 76]. This can possibly lead to drastically improved constraints, as the information content of the reconstruction is multiplied, and help in the resolution of possible deficiencies or degeneracies in the data of a single band. The difficulty here is not so much the lensing, which is the same, but a meaningful relation of the source models between the bands.

Given the speed and robustness of the implementation, it is also conceivable that a code like LENSED can be useful in a lens finding scenario [16]. Here many candidate lens systems would be analysed with a fixed lens model, and flagged as soon as the reconstructions finds tangible indicators for a deflecting mass.

Finally, it is possible to implement specialised treatment for lensing by galaxy clusters, the images of which are commonly much larger in size than those of galaxy-galaxy lensing events. This is a new frontier for the forward method of lens reconstruction, and the different context provides new and unique opportunities for further optimisation.

---

#### Thanks and acknowledgements

I would like to thank Fabio Bellagamba, Ben Metcalf, Dominik Leier and the rest of the GLENCO group for their help and support over the course of this Ph.D. programme.

The analysis of Chapter 8 and Chapter 9 is based on observations made with the NASA/ESA Hubble Space Telescope, and obtained from the Hubble Legacy Archive, which is a collaboration between the Space Telescope Science Institute (STScI/NASA), the Space Telescope European Coordinating Facility (ST-ECF/ESA) and the Canadian Astronomy Data Centre (CADAC/NRC/CSA).

## References

- [1] A. Agnello, M. W. Auger and N. W. Evans, *Lensing and dynamics in two simple steps*, *MNRAS* **429** (Feb. 2013) L35, arXiv: [1209.2554](#).
- [2] S. Allam, *High-resolution imaging of three new UV-bright lensed arcs*, HST Proposal 11602, July 2009.
- [3] M. W. Auger, T. Treu, A. S. Bolton, R. Gavazzi, L. V. E. Koopmans, P. J. Marshall, K. Bundy and L. A. Moustakas, *The Sloan Lens ACS Survey. IX. Colors, Lensing, and Stellar Masses of Early-Type Galaxies*, *ApJ* **705** (Nov. 2009) 1099, arXiv: [0911.2471](#).
- [4] M. W. Auger, T. Treu, A. S. Bolton, R. Gavazzi, L. V. E. Koopmans, P. J. Marshall, L. A. Moustakas and S. Burles, *The Sloan Lens ACS Survey. X. Stellar, Dynamical, and Total Mass Correlations of Massive Early-type Galaxies*, *ApJ* **724** (Nov. 2010) 511, arXiv: [1007.2880](#).
- [5] K. Bandara, D. Crampton, C. Peng and L. Simard, *Witnessing the Differential Evolution of Disk Galaxies in Luminosity and Size via Gravitational Lensing*, *ApJ* **777** (Nov. 2013) 1.
- [6] R. Barkana, *Fast Calculation of a Family of Elliptical Mass Gravitational Lens Models*, *ApJ* **502** (Aug. 1998) 531, arXiv: [astro-ph/9802002](#).
- [7] M. Bartelmann, *Arcs from a universal dark-matter halo profile*. *A&A* **313** (Sept. 1996) 697, arXiv: [astro-ph/9602053](#).
- [8] V. Belokurov, N. W. Evans, A. Moiseev, L. J. King, P. C. Hewett, M. Pettini, L. Wyrzykowski, R. G. McMahon, M. C. Smith, G. Gilmore, S. F. Sanchez, A. Udalski, S. Koposov, D. B. Zucker and C. J. Walcher, *The Cosmic Horseshoe: Discovery of an Einstein Ring around a Giant Luminous Red Galaxy*, *ApJ* **671** (Dec. 2007) L9, arXiv: [0706.2326](#).
- [9] G. E. Blelloch, "Prefix sums and their applications", in: *Synthesis of Parallel Algorithms*, ed. by J. H. Reif, Morgan Kaufmann, 1993.
- [10] A. S. Bolton, S. Burles, L. V. E. Koopmans, T. Treu and L. A. Moustakas, *The Sloan Lens ACS Survey. I. A Large Spectroscopically Selected Sample of Massive Early-Type Lens Galaxies*, *ApJ* **638** (Feb. 2006) 703, arXiv: [astro-ph/0511453](#).

- [11] A. S. Bolton, S. Burles, L. V. E. Koopmans, T. Treu, R. Gavazzi, L. A. Moustakas, R. Wayth and D. J. Schlegel, *The Sloan Lens ACS Survey. V. The Full ACS Strong-Lens Sample*, *ApJ* **682** (Aug. 2008) 964, arXiv: [0805.1931](#).
- [12] A. S. Bolton, T. Treu, L. V. E. Koopmans, R. Gavazzi, L. A. Moustakas, S. Burles, D. J. Schlegel and R. Wayth, *The Sloan Lens ACS Survey. VII. Elliptical Galaxy Scaling Laws from Direct Observational Mass Measurements*, *ApJ* **684** (Sept. 2008) 248, arXiv: [0805.1932](#).
- [13] A. Bolton, *The Sloan Lens ACS Survey: Towards 100 New Strong Lenses*, HST Proposal, July 2006.
- [14] R. R. Bourassa and R. Kantowski, *The theory of transparent gravitational lenses*, *ApJ* **195** (Jan. 1975) 13.
- [15] R. R. Bourassa, R. Kantowski and T. D. Norton, *The Spheroidal Gravitational Lens*, *ApJ* **185** (Nov. 1973) 747.
- [16] F. Brault and R. Gavazzi, *Extensive light profile fitting of galaxy-scale strong lenses. Towards an automated lens detection method*, *A&A* **577** (May 2015) A85.
- [17] I. Bray, *Spheroidal gravitational lenses*, *MNRAS* **208** (June 1984) 511.
- [18] B. J. Brewer, D. Huijser and G. F. Lewis, *Trans-Dimensional Bayesian Inference for Gravitational Lens Substructures*, preprint (Aug. 2015), arXiv: [1508.00662](#).
- [19] B. J. Brewer, G. F. Lewis, V. Belokurov, M. J. Irwin, T. J. Bridges and N. W. Evans, *Modelling of the complex CASSOWARY/SLUGS gravitational lenses*, *MNRAS* **412** (Apr. 2011) 2521, arXiv: [1010.5298](#).
- [20] *Cambridge and Sloan Survey of Wide Arcs in the Sky (CASSOWARY) catalogue*, URL: <http://www.ast.cam.ac.uk/ioa/research/cassowary/>.
- [21] M. Capaccioli, “Photometry of early-type galaxies and the  $R^{1/4}$  law”, in: *World of Galaxies*, ed. by H. G. Corwin Jr. and L. Bottinelli, 1989.
- [22] C. L. Carilli and S. Rawlings, *Motivation, key science projects, standards and assumptions*, *New A Rev.* **48** (Dec. 2004) 979, arXiv: [astro-ph/0409274](#).
- [23] K.-H. Chae, V. K. Khersonsky and D. A. Turnshek, *Gravitational Lensing by Power-Law Mass Distributions: A Fast and Exact Series Approach*, *ApJ* **506** (Oct. 1998) 80, arXiv: [astro-ph/9808354](#).
- [24] L. Ciotti, *Stellar systems following the  $R^{1/m}$  luminosity law*, *A&A* **249** (Sept. 1991) 99.
- [25] L. Ciotti and G. Bertin, *Analytical properties of the  $R^{1/m}$  law*, *A&A* **352** (Dec. 1999) 447, arXiv: [astro-ph/9911078](#).
- [26] T. Clifton, P. G. Ferreira, A. Padilla and C. Skordis, *Modified gravity and cosmology*, *Physics Reports* **513** (Mar. 2012) 1, arXiv: [1106.2476](#).

- [27] D. Coe, N. Benítez, S. F. Sánchez, M. Jee, R. Bouwens and H. Ford, *Galaxies in the Hubble Ultra Deep Field. I. Detection, Multiband Photometry, Photometric Redshifts, and Morphology*, *AJ* **132** (Aug. 2006) 926, arXiv: [astro-ph/0605262](#).
- [28] T. E. Collett, *The Population of Galaxy-Galaxy Strong Lenses in Forthcoming Optical Imaging Surveys*, *ApJ* **811** (Sept. 2015) 20, arXiv: [1507.02657](#).
- [29] S. Dye and S. J. Warren, *Decomposition of the Visible and Dark Matter in the Einstein Ring 0047-2808 by Semilinear Inversion*, *ApJ* **623** (Apr. 2005) 31, arXiv: [astro-ph/0411452](#).
- [30] S. Dye, N. W. Evans, V. Belokurov, S. J. Warren and P. Hewett, *Models of the Cosmic Horseshoe gravitational lens J1004+4112*, *MNRAS* **388** (July 2008) 384, arXiv: [0804.4002](#).
- [31] F. W. Dyson, A. S. Eddington and C. Davidson, *A Determination of the Deflection of Light by the Sun's Gravitational Field, from Observations Made at the Total Eclipse of May 29, 1919*, *Phil. Trans. R. Soc. Lond. Ser. A* **220** (1920) 291.
- [32] N. W. Evans and M. I. Wilkinson, *Lens models with density cusps*, *MNRAS* **296** (June 1998) 800.
- [33] E. E. Falco, M. V. Gorenstein and I. I. Shapiro, *On model-dependent bounds on  $H(0)$  from gravitational images Application of Q0957 + 561A,B*, *ApJ* **289** (Feb. 1985) L1.
- [34] J. Fanelli, *A perfect coupling*, *J. Celest. Bodies* **18** (Feb. 2010).
- [35] F. Feroz and M. P. Hobson, *Multimodal nested sampling: an efficient and robust alternative to Markov Chain Monte Carlo methods for astronomical data analyses*, *MNRAS* **384** (Feb. 2008) 449, arXiv: [0704.3704](#).
- [36] F. Feroz, M. P. Hobson and M. Bridges, *MULTINEST: an efficient and robust Bayesian inference tool for cosmology and particle physics*, *MNRAS* **398** (Oct. 2009) 1601, arXiv: [0809.3437](#).
- [37] F. Feroz, M. P. Hobson, E. Cameron and A. N. Pettitt, *Importance Nested Sampling and the MultiNest Algorithm*, preprint (June 2013), arXiv: [1306.2144](#).
- [38] A. S. Fruchter and R. N. Hook, *Drizzle: A Method for the Linear Reconstruction of Undersampled Images*, *PASP* **114** (Feb. 2002) 144, eprint: [astro-ph/9808087](#).
- [39] R. Gavazzi, T. Treu, J. D. Rhodes, L. V. E. Koopmans, A. S. Bolton, S. Burles, R. J. Massey and L. A. Moustakas, *The Sloan Lens ACS Survey. IV. The Mass Density Profile of Early-Type Galaxies out to 100 Effective Radii*, *ApJ* **667** (Sept. 2007) 176, arXiv: [astro-ph/0701589](#).

- [40] R. Gavazzi, T. Treu, L. V. E. Koopmans, A. S. Bolton, L. A. Moustakas, S. Burles and P. J. Marshall, *The Sloan Lens ACS Survey. VI. Discovery and Analysis of a Double Einstein Ring*, *ApJ* **677** (Apr. 2008) 1046, arXiv: [0801.1555](#).
- [41] M. V. Gorenstein, I. I. Shapiro and E. E. Falco, *Degeneracies in parameter estimates for models of gravitational lens systems*, *ApJ* **327** (Apr. 1988) 693.
- [42] A. W. Graham and S. P. Driver, *A Concise Reference to (Projected) Sérsic  $R^{1/n}$  Quantities, Including Concentration, Profile Slopes, Petrosian Indices, and Kron Magnitudes*, *PASA* **22** (2005) 118, arXiv: [astro-ph/0503176](#).
- [43] K. N. Hainline, A. E. Shapley, K. A. Kornei, M. Pettini, E. Buckley-Geer, S. S. Allam and D. L. Tucker, *Rest-Frame Optical Spectra of Three Strongly Lensed Galaxies at  $z \sim 2$* , *ApJ* **701** (Aug. 2009) 52, arXiv: [0906.2197](#).
- [44] *Hubble Legacy Archive*, URL: <http://hla.stsci.edu>.
- [45] Z. Ivezić et al., *LSST: from Science Drivers to Reference Design and Anticipated Data Products*, preprint (May 2008), arXiv: [0805.2366](#).
- [46] T. A. Jones, R. S. Ellis, M. A. Schenker and D. P. Stark, *Keck Spectroscopy of Gravitationally Lensed  $z \gtrsim 4$  Galaxies: Improved Constraints on the Escape Fraction of Ionizing Photons*, *ApJ* **779** (Dec. 2013) 52, arXiv: [1304.7015](#).
- [47] R. E. Kass and A. E. Raftery, *Bayes Factors*, *J. Am. Stat. Assoc.* **90** (June 1995) 773.
- [48] A. Kassiola and I. Kovner, *Elliptic Mass Distributions versus Elliptic Potentials in Gravitational Lenses*, *ApJ* **417** (Nov. 1993) 450.
- [49] C. R. Keeton, *A Catalog of Mass Models for Gravitational Lensing*, preprint (Feb. 2001), arXiv: [astro-ph/0102341](#).
- [50] C. R. Keeton and C. S. Kochanek, *Gravitational Lensing by Spiral Galaxies*, *ApJ* **495** (Mar. 1998) 157, eprint: [astro-ph/9705194](#).
- [51] J. Khoury, *Les Houches Lectures on Physics Beyond the Standard Model of Cosmology*, preprint (Dec. 2013), arXiv: [1312.2006](#).
- [52] C. S. Kochanek and R. Narayan, *LensClean - an algorithm for inverting extended, gravitationally lensed images with application to the radio ring lens PKS 1830-211*, *ApJ* **401** (Dec. 1992) 461.
- [53] L. V. E. Koopmans, T. Treu, A. S. Bolton, S. Burles and L. A. Moustakas, *The Sloan Lens ACS Survey. III. The Structure and Formation of Early-Type Galaxies and Their Evolution since  $z \sim 1$* , *ApJ* **649** (Oct. 2006) 599, arXiv: [astro-ph/0601628](#).
- [54] R. Kormann, P. Schneider and M. Bartelmann, *Isothermal elliptical gravitational lens models*, *A&A* **284** (Apr. 1994) 285.
- [55] Z. Kostrzewa-Rutkowska, L. Wyrzykowski, M. W. Auger, T. E. Collett and V. Belokurov, *The evolution of late-type galaxies from CASSOWARY lensing systems*, *MNRAS* **441** (July 2014) 3238, arXiv: [1406.1114](#).

- [56] J. E. Krist, R. N. Hook and F. Stoehr, “20 years of Hubble Space Telescope optical modeling using Tiny Tim”, in: *Proc. SPIE*, vol. 8127, Oct. 2011.
- [57] A. Krommer and C. Ueberhuber, *Computational Integration*, SIAM, 1998.
- [58] A. T. Lefor, T. Futamase and M. Akhlaghi, *A systematic review of strong gravitational lens modeling software*, *New A Rev.* 57 (July 2013) 1, arXiv: [1206.4382](#).
- [59] C. Leitherer, C. A. Tremonti, T. M. Heckman and D. Calzetti, *An Ultraviolet Spectroscopic Atlas of Local Starbursts and Star-forming Galaxies: The Legacy of FOS and GHRS*, *AJ* 141 (Feb. 2011) 37, arXiv: [1011.0385](#).
- [60] P. J. Marshall, T. Treu, J. Melbourne, R. Gavazzi, K. Bundy, S. M. Ammons, A. S. Bolton, S. Burles, J. E. Larkin, D. Le Mignant, D. C. Koo, L. V. E. Koopmans, C. E. Max, L. A. Moustakas, E. Steinbring and S. A. Wright, *Superresolving Distant Galaxies with Gravitational Telescopes: Keck Laser Guide Star Adaptive Optics and Hubble Space Telescope Imaging of the Lens System SDSS J0737+3216*, *ApJ* 671 (Dec. 2007) 1196, arXiv: [0710.0637](#).
- [61] P. Melchior, M. Meneghetti and M. Bartelmann, *Reliable shapelet image analysis*, *A&A* 463 (Mar. 2007) 1215, arXiv: [astro-ph/0608369](#).
- [62] M. Meneghetti, P. Melchior, A. Grazian, G. De Lucia, K. Dolag, M. Bartelmann, C. Heymans, L. Moscardini and M. Radovich, *Realistic simulations of gravitational lensing by galaxy clusters: extracting arc parameters from mock DUNE images*, *A&A* 482 (May 2008) 403, arXiv: [0711.3418](#).
- [63] R. B. Metcalf and M. Petkova, *GLAMER - I. A code for gravitational lensing simulations with adaptive mesh refinement*, *MNRAS* 445 (Dec. 2014) 1942, arXiv: [1312.1128](#).
- [64] C. Moler, “Matrix Computation on Distributed Memory Multiprocessors”, in: *Hypercube Multiprocessors 1986*, ed. by M. T. Heath, SIAM, 1986.
- [65] B. Moore, T. Quinn, F. Governato, J. Stadel and G. Lake, *Cold collapse and the core catastrophe*, *MNRAS* 310 (Dec. 1999) 1147, arXiv: [astro-ph/9903164](#).
- [66] J. J. Moré, “The Levenberg-Marquardt algorithm: Implementation and theory”, in: *Numerical Analysis*, ed. by G. A. Watson, vol. 630, Lecture Notes in Mathematics, Springer, 1978.
- [67] J. Moré and S. Wright, *Optimization Software Guide*, SIAM, 1993.
- [68] *NIST Digital Library of Mathematical Functions*, Online companion to [72], URL: <http://dlmf.nist.gov/>.
- [69] J. F. Navarro, C. S. Frenk and S. D. M. White, *The Structure of Cold Dark Matter Halos*, *ApJ* 462 (May 1996) 563, arXiv: [astro-ph/9508025](#).

- [70] E. R. Newton, P. J. Marshall, T. Treu, M. W. Auger, R. Gavazzi, A. S. Bolton, L. V. E. Koopmans and L. A. Moustakas, *The Sloan Lens ACS Survey. XI. Beyond Hubble Resolution: Size, Luminosity, and Stellar Mass of Compact Lensed Galaxies at Intermediate Redshift*, *ApJ* **734** (June 2011) 104, arXiv: [1104.2608](#).
- [71] J. W. Nightingale and S. Dye, *Adaptive semi-linear inversion of strong gravitational lens imaging*, *MNRAS* **452** (Sept. 2015) 2940, arXiv: [1412.7436](#).
- [72] F. W. J. Olver, D. W. Lozier, R. F. Boisvert and C. W. Clark, eds., *NIST Handbook of Mathematical Functions*, Print companion to [68], Cambridge University Press, 2010.
- [73] G. Orban de Xivry and P. Marshall, *An atlas of predicted exotic gravitational lenses*, *MNRAS* **399** (Oct. 2009) 2, arXiv: [0904.1454](#).
- [74] T. N. L. Patterson, *The Optimum Addition of Points to Quadrature Formulae*, *Math. Comput.* **22** (Oct. 1968) 847.
- [75] C. Y. Peng, L. C. Ho, C. D. Impey and H.-W. Rix, *Detailed Decomposition of Galaxy Images. II. Beyond Axisymmetric Models*, *AJ* **139** (June 2010) 2097, arXiv: [0912.0731](#).
- [76] C. Y. Peng, L. C. Ho, C. D. Impey and H.-W. Rix, *Detailed Structural Decomposition of Galaxy Images*, *AJ* **124** (July 2002) 266, arXiv: [astro-ph/0204182](#).
- [77] C. Y. Peng, C. D. Impey, H.-W. Rix, C. S. Kochanek, C. R. Keeton, E. E. Falco, J. Lehár and B. A. McLeod, *Probing the Coevolution of Supermassive Black Holes and Galaxies Using Gravitationally Lensed Quasar Hosts*, *ApJ* **649** (Oct. 2006) 616, eprint: [astro-ph/0603248](#).
- [78] M. Petkova, R. B. Metcalf and C. Giocoli, *GLAMER - II. Multiple-plane gravitational lensing*, *MNRAS* **445** (Dec. 2014) 1954, arXiv: [1312.1536](#).
- [79] A. O. Petters, H. Levine and J. Wambsganss, *Singularity Theory and Gravitational Lensing*, Progress in Mathematical Physics 21, Birkhäuser, 2001.
- [80] W. H. Press, S. A. Teukolsky, W. T. Vetterling and B. P. Flannery, *Numerical Recipes*, 3rd ed., Cambridge University Press, Sept. 2007.
- [81] A. M. Quider, M. Pettini, A. E. Shapley and C. C. Steidel, *The ultraviolet spectrum of the gravitationally lensed galaxy 'the Cosmic Horseshoe': a close-up of a star-forming galaxy at  $z \sim 2$* , *MNRAS* **398** (Sept. 2009) 1263, arXiv: [0906.2412](#).
- [82] A. Refregier, *Shapelets - I. A method for image analysis*, *MNRAS* **338** (Jan. 2003) 35, arXiv: [astro-ph/0105178](#).
- [83] A. Refregier and D. Bacon, *Shapelets - II. A method for weak lensing measurements*, *MNRAS* **338** (Jan. 2003) 48, arXiv: [astro-ph/0105179](#).

- [84] J. Richard, T. Jones, R. Ellis, D. P. Stark, R. Livermore and M. Swinbank, *The emission line properties of gravitationally lensed  $1.5 < z < 5$  galaxies*, *MNRAS* **413** (May 2011) 643, arXiv: [1011.6413](#).
- [85] R. Scaramella, Y. Mellier, J. Amiaux, C. Burigana, C. S. Carvalho, J. C. Cuillandre, A. da Silva, J. Dinis, A. Derosa, E. Maiorano, P. Franzetti, B. Garilli, M. Maris, M. Meneghetti, I. Tereno, S. Wachter, L. Amendola, M. Cropper, V. Cardone, R. Massey, S. Niemi, H. Hoekstra, T. Kitching, L. Miller, T. Schrabback, E. Semboloni, A. Taylor, M. Viola, T. Maciaszek, A. Ealet, L. Guzzo, K. Jahnke, W. Percival, F. Pasian, M. Sauvage and the Euclid Collaboration, *Euclid space mission: a cosmological challenge for the next 15 years*, preprint (Jan. 2015), arXiv: [1501.04908](#).
- [86] P. Schneider, J. Ehlers and E. E. Falco, *Gravitational Lenses*, Springer, 1992.
- [87] P. Schneider, C. S. Kochanek and J. Wambsganss, *Gravitational Lensing: Strong, Weak and Micro*, ed. by G. Meylan, P. Jetzer and P. North, Saas-Fee Advanced Courses 33, Springer, 2006, arXiv: [astro-ph/0407232](#).
- [88] P. Schneider and A. Weiss, *A practical approach to (nearly) elliptical gravitational lens models*, *A&A* **247** (July 1991) 269.
- [89] T. Schramm, *Realistic elliptical potential wells for gravitational lens models*, *A&A* **231** (May 1990) 19.
- [90] J. L. Sérsic, *Atlas de galaxias australes*, Observatorio Astronomico, Universidad Nacional de Cordoba, 1968.
- [91] J. L. Sérsic, *Influence of the atmospheric and instrumental dispersion on the brightness distribution in a galaxy*, *Bol. Asociacion Argentina Astron.* **6** (1963) 41.
- [92] T. Shibuya, M. Ouchi and Y. Harikane, *Morphologies of  $\sim 190,000$  Galaxies at  $z = 0-10$  Revealed with HST Legacy Data. I. Size Evolution*, *ApJS* **219** (Aug. 2015) 15, arXiv: [1503.07481](#).
- [93] Y. Shu, A. S. Bolton, J. R. Brownstein, A. D. Montero-Dorta, L. V. E. Koopmans, T. Treu, R. Gavazzi, M. W. Auger, O. Czoske, P. J. Marshall and L. A. Moustakas, *The Sloan Lens ACS Survey. XII. Extending Strong Lensing to Lower Masses*, *ApJ* **803** (Apr. 2015) 71, arXiv: [1407.2240](#).
- [94] J. Skilling, "Nested Sampling", in: *AIP Conf. Proc.* Ed. by R. Fischer, R. Preuss and U. V. Toussaint, vol. 735, Nov. 2004.
- [95] J. Skilling, *Nested sampling for general Bayesian computation*, *Bayesian Anal.* **1** (Dec. 2006) 833.
- [96] A. Sonnenfeld, R. Gavazzi, S. H. Suyu, T. Treu and P. J. Marshall, *The SL2S Galaxy-scale Lens Sample. III. Lens Models, Surface Photometry, and Stellar Masses for the Final Sample*, *ApJ* **777** (Nov. 2013) 97, arXiv: [1307.4764](#).

- [97] D. Spergel, N. Gehrels, J. Breckinridge, M. Donahue, A. Dressler, B. S. Gaudi, T. Greene, O. Guyon, C. Hirata, J. Kalirai, N. J. Kasdin, W. Moos, S. Perlmutter, M. Postman, B. Rauscher, J. Rhodes, Y. Wang, D. Weinberg, J. Centrella, W. Traub, C. Baltay, J. Colbert, D. Bennett, A. Kiessling, B. Macintosh, J. Merten, M. Mortonson, M. Penny, E. Rozo, D. Savransky, K. Stapelfeldt, Y. Zu, C. Baker, E. Cheng, D. Content, J. Dooley, M. Foote, R. Goullioud, K. Grady, C. Jackson, J. Kruk, M. Levine, M. Melton, C. Peddie, J. Ruffa and S. Shaklan, *Wide-Field InfraRed Survey Telescope-Astrophysics Focused Telescope Assets WFIRST-AFTA Final Report*, preprint (May 2013), arXiv: [1305.5422](#).
- [98] C. Spiniello, L. V. E. Koopmans, S. C. Trager, O. Czoske and T. Treu, *The X-Shooter Lens Survey - I. Dark matter domination and a Salpeter-type initial mass function in a massive early-type galaxy*, *MNRAS* **417** (Nov. 2011) 3000, arXiv: [1103.4773](#).
- [99] J. E. Stone, D. Gohara and Guochun Shi, *OpenCL: A Parallel Programming Standard for Heterogeneous Computing Systems*, *Comput. Sci. Eng.* **12** (May 2010) 66.
- [100] S. H. Suyu, P. J. Marshall, M. P. Hobson and R. D. Blandford, *A Bayesian analysis of regularized source inversions in gravitational lensing*, *MNRAS* **371** (Sept. 2006) 983, arXiv: [astro-ph/0601493](#).
- [101] A. S. Tagore and C. R. Keeton, *Statistical and systematic uncertainties in pixel-based source reconstruction algorithms for gravitational lensing*, *MNRAS* **445** (Nov. 2014) 694, arXiv: [1408.6297](#).
- [102] N. Tessore, F. Bellagamba and R. B. Metcalf, *Lensed: Forward parametric modelling of strong lenses*, Astrophysics Source Code Library, May 2015, ascl: [1505.026](#).
- [103] N. Tessore, F. Bellagamba and R. B. Metcalf, *Lensed: a code for the forward reconstruction of lenses and sources from strong lensing observations*, preprint (May 2015), arXiv: [1505.07674](#).
- [104] N. Tessore and R. B. Metcalf, *The elliptical power law profile lens*, *A&A* **580** (Aug. 2015) A79, arXiv: [1507.01819](#).
- [105] *TINY TIM web interface*, URL: <http://tinytim.stsci.edu>.
- [106] T. Treu, R. Gavazzi, A. Gorecki, P. J. Marshall, L. V. E. Koopmans, A. S. Bolton, L. A. Moustakas and S. Burles, *Erratum: "The SLACS Survey. VIII. The Relation Between Environment and Internal Structure of Early-Type Galaxies"*, *ApJ* **692** (Feb. 2009) 1690.
- [107] T. Treu, L. V. E. Koopmans, A. S. Bolton, S. Burles and L. A. Moustakas, *Erratum: "The Sloan Lens ACS Survey. II. Stellar Populations and Internal Structure of Early-Type Lens Galaxies"*, *ApJ* **650** (Oct. 2006) 1219.

- [108] T. Treu, R. Gavazzi, A. Gorecki, P. J. Marshall, L. V. E. Koopmans, A. S. Bolton, L. A. Moustakas and S. Burles, *The SLACS Survey. VIII. The Relation between Environment and Internal Structure of Early-Type Galaxies*, *ApJ* **690** (Jan. 2009) 670, arXiv: [0806.1056](#).
- [109] T. Treu, L. V. Koopmans, A. S. Bolton, S. Burles and L. A. Moustakas, *The Sloan Lens ACS Survey. II. Stellar Populations and Internal Structure of Early-Type Lens Galaxies*, *ApJ* **640** (Apr. 2006) 662, arXiv: [astro-ph/0512044](#).
- [110] S. Vegetti and L. V. E. Koopmans, *Bayesian strong gravitational-lens modelling on adaptive grids: objective detection of mass substructure in Galaxies*, *MNRAS* **392** (Jan. 2009) 945, arXiv: [0805.0201](#).
- [111] S. Vegetti, L. V. E. Koopmans, A. Bolton, T. Treu and R. Gavazzi, *Detection of a dark substructure through gravitational imaging*, *MNRAS* **408** (Nov. 2010) 1969, arXiv: [0910.0760](#).
- [112] M. Vika, S. P. Bamford, B. Häußler, A. L. Rojas, A. Borch and R. C. Nichol, *MegaMorph - multiwavelength measurement of galaxy structure. Sérsic profile fits to galaxies near and far*, *MNRAS* **435** (Oct. 2013) 623, arXiv: [1307.4996](#).
- [113] S. Wallington, C. S. Kochanek and R. Narayan, *LensMEM: A Gravitational Lens Inversion Algorithm Using the Maximum Entropy Method*, *ApJ* **465** (July 1996) 64, arXiv: [astro-ph/9511137](#).
- [114] S. J. Warren and S. Dye, *Semilinear Gravitational Lens Inversion*, *ApJ* **590** (June 2003) 673, arXiv: [astro-ph/0302587](#).
- [115] C. M. Will, *Henry Cavendish, Johann von Soldner, and the deflection of light*, *Am. J. Phys.* **56** (May 1988) 413.
- [116] C. M. Will, *The 1919 measurement of the deflection of light*, *Class. Quantum Grav.* **32** (June 2015) 124001, arXiv: [1409.7812](#).
- [117] C. M. Will, *The Confrontation between General Relativity and Experiment*, *Living Rev. Relativ.* **17** (June 2014) 4, arXiv: [1403.7377](#).
- [118] G. de Vaucouleurs, *Recherches sur les Nebuleuses Extragalactiques*, *Ann. Astrophys.* **11** (Jan. 1948) 247.

# Appendix

---

## Weak lensing and cosmology

# A Weak lensing of large scale structure in the presence of screening

The contents this chapter have been published as N. Tessore et al., *Weak lensing of large scale structure in the presence of screening*, *J. Cosmology Astropart. Phys.* **10** (Oct. 2015) 36, arXiv: [1508.04011](https://arxiv.org/abs/1508.04011).

## A.1 Introduction

A possible approach to explaining the observational evidence for cosmic acceleration is that general relativity is modified in regions of low density, low acceleration or, simply, on large scales. A number of models have been proposed [16], and the idea that there may be a *gravitational* solution to the dark energy problem has led to a renewed scrutiny of the fundamental properties of gravity. The hope is that, in the very least, a better understanding of general relativity will emerge from current and future cosmological observations.

A common feature in a number of modified theories of gravity is that there is some form of *screening* [31]. Precision tests [5, 64] indicate that general relativity is at least an excellent effective theory for describing gravitational physics locally or in regions of moderately high density and curvature. This means that, in any modification of the theory, the nature of gravity must depend on its environment and that deviations from general relativity are absent (or screened) in regions in which it has been well tested. Current proposals involve the chameleon [32, 41], symmetron [25, 44, 48] or Vainshtein [62] mechanism, all of which lead to particular features in the gravitational potential.

A key characteristic of the various screening mechanisms [25, 32, 62] currently being considered is that they are fundamentally non-linear. While they might have an effect in regimes where density perturbations are still in the linear regime, their full effect comes into play in the non-linear regime of gravitational collapse. This means that, in order to fully understand the effect of screening in universes which closely resemble our own, it must be possible to model non-linear structure formation not only accurately but also efficiently. There has been substantial progress in numerically modelling the quasi-linear and non-linear regime of structure formation using adapted  $N$ -body codes [37, 39, 49, 68], and codes are now beginning to reach the level of accuracy required for what has been dubbed “precision cosmology”. Such accuracy is at the expense of highly intensive com-

puter algorithms which focus on specific models and hence on a reduced subset of the full parameter space that needs to be explored. Winther and Ferreira [65] have therefore recently advocated the development of approximate algorithms to explore a broader range of parameter space at the expense of accuracy.

With a modified  $N$ -body code it is then possible to study the observational consequences of gravitational screening by generating a wide suite of simulations which in turn can be used to design future surveys. Converting such simulations into mock surveys is a crucial step in optimising the scientific returns of cosmological experiments such as Euclid [51], LSST [29], WFIRST [57] and SKA [15].

One particular cosmological probe — the weak lensing of galaxies by intervening gravitational potentials — has been heralded as a particularly powerful test of gravitational physics on large scales. It should supply complementary information to probes of the matter density field through spectroscopic and photometric galaxy redshift surveys and, in principle, will be insensitive to galaxy bias. Current measurements of weak lensing on large scales are not yet competitive with other cosmological probes, but the future looks promising with the surveys mentioned above.

This chapter describes the algorithms that can be used to produce lensing maps in cosmologies with screening. The modified gravity simulations are realised with the code described in [39] and for lensing, the GLAMER pipeline [40, 47] is used. The methods proposed here are the starting point for developing a concerted and comprehensive search for signatures of screening in observations of weak lensing. This work complements a larger effort by many groups [18, 23, 28, 40, 47, 50].

The outline of this chapter is as follows. Section A.2 briefly summarises the theoretical framework with a particular and systematic focus on the different mechanisms for gravitational screening and how they can be parametrised. Section A.3 describes the modified  $N$ -body algorithm which produces the density field, as well as the lensing pipeline consisting of MAPSIM and GLAMER. Section A.4 presents the results of a suite of simulations, focusing on maps and a few of the main one-point and two-point statistics. Finally, Section A.5 discusses the results as well as the limitations and future applications of this approach.

## A.2 Theory

### Scalar-tensor theories

This chapter will focus on scalar-tensor theories of modified gravity that display some form of screening mechanism. These are contained in the general Lag-

rangian<sup>1</sup>

$$\mathcal{L} = \frac{R}{2} M_{\text{Pl}}^2 + \mathcal{L}_\phi(\phi, \partial\phi, \partial\partial\phi) + \mathcal{L}_m(A^2(\phi)g_{\mu\nu}, \psi_m), \quad (\text{A.1})$$

where  $M_{\text{Pl}}^2 \equiv (8\pi G)^{-1}$  and  $\psi_m$  are the matter-fields. Matter is coupled to the scalar field via the effective metric

$$\tilde{g}_{\mu\nu} = A^2(\phi)g_{\mu\nu}, \quad (\text{A.2})$$

and therefore moves on geodesics of the  $\tilde{g}_{\mu\nu}$  metric. In the Einstein frame, where gravity is described by general relativity, this implies the existence of a fifth-force; for a test mass in the non-relativistic limit the force is given by

$$F_\phi = \nabla \log A(\phi). \quad (\text{A.3})$$

The key to a successful modified gravity model is a way of evading the stringent constraints from local gravity experiments and at the same time giving rise to interesting astrophysical and cosmological signatures. One such way is through what is commonly called a ‘‘screening mechanism’’, and below a short review is given of the different screening mechanisms investigated here.

### Screening mechanisms

To see how screening can emerge in a scalar tensor theory, the general scalar field Lagrangian (A.1) is expanded to quadratic order about a given field value  $\phi_0$

$$\mathcal{L}_{\text{quadratic}} = X^{\mu\nu}(\phi_0)\partial_\mu\delta\phi\partial_\nu\delta\phi + m^2(\phi_0)\delta\phi^2 + \frac{\beta(\phi_0)\delta\phi}{M_{\text{Pl}}}\rho_m, \quad (\text{A.4})$$

where  $m(\phi_0) = \sqrt{d^2V(\phi_0)/d\phi^2}$  is the (local) value of the scalar field mass,  $V(\phi)$  is the potential for  $\phi$ , and  $\beta = \frac{d\log A}{d\phi}M_{\text{Pl}}$  is the (local) coupling strength of the fifth-force. The value  $2\beta^2 = 1$  corresponds to a force with the strength of gravity. The fifth-force on a test mass, from a source of mass  $M$ , can schematically be written in the form

$$F_\phi \simeq \frac{GM}{r^2} \frac{2\beta^2(\phi_0)}{\sqrt{|X^{\mu\nu}(\phi_0)|}} e^{-m(\phi_0)r}. \quad (\text{A.5})$$

Now two different regions  $A$  and  $B$  of space-time are considered, where  $\phi_0 = \phi_A$  and  $\phi_0 = \phi_B \neq \phi_A$ . From the quadratic Lagrangian (A.4) it follows that there are at least three ways in which some form of screening can emerge. One way to reduce the effect of the fifth-force (in region  $B$  compared to  $A$ ) is by having a

---

<sup>1</sup> $f(R)$  gravity requires a conformal transformation  $g_{\mu\nu} \rightarrow g_{\mu\nu}A^2(\phi)$  with  $A(\phi) = e^{\frac{\beta\phi}{M_{\text{Pl}}}}$  and  $\beta = 1/\sqrt{6}$  to be brought into this form [12].

large local mass  $m(\phi_B) \gg m(\phi_A)$  which implies a very short interaction range (the chameleon mechanism). If the matter coupling  $\beta(\phi_B) \ll \beta(\phi_A)$ , the fifth-force will also be suppressed (the symmetron mechanism). Lastly, the condition  $|X^{\mu\nu}(\phi_B)| \gg |X^{\mu\nu}(\phi_A)|$  leads, after canonical normalisation, to a weakened matter source and therefore also a weakened fifth-force (the Vainshtein mechanism).

It should be noted that this simplified description does not tell the whole story; added to these effects there can be (and is) additional screening which can only be studied by considering the full non-linear dynamics of the scalar field.

**Chameleon mechanism** The chameleon mechanism [32, 41] can be found in models defined by the Lagrangian

$$\mathcal{L}_\phi = \frac{1}{2}(\nabla\phi)^2 + V(\phi). \quad (\text{A.6})$$

The Klein-Gordon equation for the scalar field reads

$$\square\phi + V_{\text{eff},\phi} = 0. \quad (\text{A.7})$$

In the presence of matter sources, the dynamics of  $\phi$  are determined by an effective potential which, for non-relativistic matter, is given by

$$V_{\text{eff}} = V(\phi) + \frac{A(\phi)\rho_m}{M_{\text{Pl}}}. \quad (\text{A.8})$$

To see how screening works in detail, one can consider a static and spherically symmetric object of density  $\rho_0$  and radius  $R$  embedded in a background of density  $\rho_{\text{env}}$ . The approximate solution to the Klein-Gordon equation [32] in this case leads to a fifth-force given by

$$F_\phi \simeq 2\beta^2 \frac{\Delta R}{R} \frac{GM}{r^2} e^{-m_{\text{env}} r}, \quad (\text{A.9})$$

where  $m_{\text{env}} = \sqrt{V_{\text{eff},\phi\phi}(\phi_{\text{env}})}$  is the mass of the scalar field in the background,  $\beta = M_{\text{Pl}} \frac{d \log A}{d\phi}$  is the coupling strength (which is constant in the chameleon model) and

$$\frac{\Delta R}{R} = \min \left\{ 1, \frac{|\phi_0 - \phi_{\text{env}}|}{2\beta M_{\text{Pl}} \Phi_N} \right\} \quad (\text{A.10})$$

is the so-called thin-shell screening factor where  $\Phi_N$  is the Newtonian potential of the object and the subscript “0” or “env” refers to quantities at the centre or in the environment of the object, respectively. The larger the Newtonian potential becomes, the smaller  $\frac{\Delta R}{R}$  is, and the fifth-force is screened. On top of this, and in dense environments, the term  $|\phi_0 - \phi_{\text{env}}|$  also becomes small (and  $m_{\text{env}}$  becomes large), giving rise to an environmental screening effect, i.e. an object that is not screened on its own can be screened if it is in a very dense environment. This environmental dependence has many interesting consequences [52, 67, 70].

**Symmetron mechanism** The original symmetron model [25] is defined by the same Lagrangian as for the chameleon, where

$$V(\phi) = -\frac{1}{2}\mu^2\phi^2 + \frac{1}{4}\lambda\phi^4, \quad (\text{A.11})$$

$$A(\phi) = 1 + \frac{1}{2}\frac{\phi^2}{M^2} \rightarrow \beta(\phi) = \frac{\phi M_{\text{Pl}}}{M^2}, \quad (\text{A.12})$$

and where  $\mu, M, \lambda$  are model parameters. The effective potential in the presence of matter sources is given by

$$V_{\text{eff}}(\phi) = \frac{1}{2}\left(\frac{\rho_m}{\mu^2 M^2} - 1\right)\mu^2\phi^2 + \frac{1}{4}\lambda\phi^4. \quad (\text{A.13})$$

The symmetron mechanism is similar to the chameleon mechanism, except that the coupling  $\beta$  is now field dependent, leading to an additional screening effect. If the local density satisfies  $\rho_m > \mu^2 M^2$ , the effective potential has a minimum at  $\phi = 0$ , and the field will reside near it. Since the coupling is proportional to  $\phi$ , the effective matter coupling is suppressed in high density regions, and the fifth-force is additionally screened.

The same screening conditions (A.9)–(A.10) as for the chameleon also apply to the symmetron, but now  $\beta = \beta(\phi_{\text{env}})$  is not a constant anymore.

**Vainshtein mechanism** The Vainshtein mechanism [62] is responsible for the viability of *massive gravity*, but it can be present in other theories, most notably the Galileons [42] and the DGP model [21]. Instead of the original DGP model, a toy model is used with the same fifth-force, thus having the correct Vainshtein screening, but a  $\Lambda$ CDM background instead. This is known as the normal branch DGP model, where dark energy is added in the form of a cosmological constant [22]. The field equation for the scalar field, which is the so-called brane-bending mode in the DGP model, reads

$$\square\phi + \frac{r_c^2}{3\beta_{\text{DGP}}(a)a^2}((\square\phi)^2 - (\nabla_\mu\nabla_\nu\phi)^2) = \frac{8\pi G a^2}{3\beta_{\text{DGP}}} \delta\rho_m, \quad (\text{A.14})$$

where  $r_c$  is the so-called cross-over scale and  $a$  is the scale parameter of the background metric. In the original DGP model,  $r_c$  dictates at what length-scales gravity becomes 5D and  $\beta_{\text{DGP}}(a) = 1 + 2r_c H(a) \left(1 + \frac{\dot{H}}{3H^2}\right)$ . For static spherical symmetric configurations, the field equation reduces to

$$\frac{1}{r^2} \frac{d}{dr} \left[ r^2 \frac{d\phi}{dr} \right] + \frac{2r_c^2}{3\beta_{\text{DGP}}(a)} \frac{d}{dr} \left[ r \left( \frac{d\phi}{dr} \right)^2 \right] = \frac{8\pi G \delta\rho_m}{3\beta_{\text{DGP}}(a)}. \quad (\text{A.15})$$

This equation can be integrated to yield

$$\frac{d\phi}{rdr} + \frac{2r_c^2}{3\beta_{\text{DGP}}(a)a^2} \left( \frac{d\phi}{rdr} \right)^2 = \frac{2a^2}{3\beta_{\text{DGP}}(a)} \frac{GM}{r^3}, \quad (\text{A.16})$$

which results in the fifth-force on a test-mass being

$$F_\phi = \frac{GM}{r^2} \frac{1}{3\beta_{\text{DGP}}(a)} 2 \left[ \frac{\sqrt{1 + (r_V/r)^3} - 1}{(r_V/r)^3} \right], \quad (\text{A.17})$$

where  $r_V = \left( \frac{16GM}{9\beta_{\text{DGP}}^2} r_c^2 \right)^{1/3}$  is the so-called Vainshtein radius. The screening mechanism works so that the fifth-force is screened at distances smaller than the Vainshtein radius ( $r \ll r_V$ ). As opposed to the chameleon and symmetron screening mechanisms, where the mass-term gives the fifth-force at finite range, gravity in this case is modified on the largest scales:  $F_\phi \simeq \frac{GM}{r^2} \frac{1}{3\beta_{\text{DGP}}(a)}$  for  $r \gg r_V$ .

### Linear perturbations in modified gravity

The evolution of linear matter density perturbations in the relevant models can be written in the general form [11]

$$\ddot{\delta}_m + 2H\dot{\delta}_m = \frac{3}{2}\Omega_m(a)H^2\delta_m \frac{G_{\text{eff}}(k, a)}{G}, \quad (\text{A.18})$$

where  $G_{\text{eff}}(k, a)$  is the effective gravitational constant in Fourier space. In the case  $G_{\text{eff}}(k, a) = G$  the equation governing the evolution of density perturbations in  $\Lambda$ CDM is recovered. For the chameleon and symmetron mechanism [11]

$$\frac{G_{\text{eff}}(k, a)}{G} = 1 + \frac{2\beta^2(a)k^2}{k^2 + a^2m(a)^2}, \quad (\text{A.19})$$

where  $\beta(a)$  and  $m(a)$  are the respective coupling and mass of the scalar field along the cosmological attractor solutions. The form of this equation can be understood as the ratio of the Fourier transforms of the fifth-force potential and Newtonian gravitational potential,  $\mathcal{F}[\nabla^2\Phi_N + \nabla^2\log A]/\mathcal{F}[\nabla^2\Phi_N] = 1 + 2\beta^2(a) \frac{k^2}{k^2 + m^2 a^2}$ .

For large scales  $k/a \ll \frac{1}{m(a)}$ , it follows that  $\frac{G_{\text{eff}}(k, a)}{G} \approx 1$ , in which case the  $\Lambda$ CDM evolution is recovered. On the other hand, on small scales  $k/a \gg 1/m(a)$  it follows that  $\frac{G_{\text{eff}}(k, a)}{G} = 1 + 2\beta^2(a)$ , and gravity is modified. For the symmetron, relevant expressions are

$$m(a) = \frac{1}{\lambda_\phi} \sqrt{1 - (a_{\text{ssb}}/a)^3}, \quad (\text{A.20})$$

$$\beta(a) = \beta_0 \sqrt{1 - (a_{\text{ssb}}/a)^3}, \quad (\text{A.21})$$

where  $\lambda_\phi = \frac{1}{\sqrt{2\mu}}$  is the range of the symmetron field at  $z = 0$ ,  $\beta_0 = \frac{\mu M_{\text{pl}}}{\sqrt{\lambda} M^2}$  is the coupling strength relative to gravity and  $a_{\text{ssb}} = \left( \frac{3H_0^2 M_{\text{pl}}^2 \Omega_m}{M^2 \mu^2} \right)^{1/3}$  is the scale-factor at which the modifications of gravity become noticeable.

For the Hu-Sawicky  $f(R)$  model [27], which is one of the simulated models, the relevant expressions are

$$m(a) = \frac{H_0 \sqrt{\Omega_m + 4\Omega_\Lambda}}{\sqrt{(n+1)|f_{R0}|}} \left( \frac{\Omega_m a^{-3} + 4\Omega_\Lambda}{\Omega_m + 4\Omega_\Lambda} \right)^{n/2+1}, \quad (\text{A.22})$$

$$\beta(a) = \frac{1}{\sqrt{6}}, \quad (\text{A.23})$$

where  $n$  and  $|f_{R0}|$  are model parameters. In the following, only the case where the primordial power spectrum index is  $n = 1$  will be considered. The DGP model used here corresponds to taking

$$m(a) = 0, \quad (\text{A.24})$$

$$\beta(a) = \frac{1}{\sqrt{6\beta_{\text{DGP}}(a)}}. \quad (\text{A.25})$$

Note that, since  $m(a) = 0$ , there is no scale (or  $k$ ) dependence in  $G_{\text{eff}}(a)$ .

Another way to look at these models is within the  $\gamma, \mu$  parameterisation [1], where the metric potentials are given by  $\nabla^2 \Psi = 4\pi G a^2 \mu \delta \rho_m$  and  $\Phi = \gamma \Psi$ . It follows that

$$\mu = \frac{m^2(a)a^2 + (1 + 2\beta^2(a))k^2}{m^2(a)a^2 + k^2}, \quad (\text{A.26})$$

$$\gamma = \frac{m^2(a)a^2 + (1 - 2\beta^2(a))k^2}{m^2(a)a^2 + (1 + 2\beta^2(a))k^2}. \quad (\text{A.27})$$

For the symmetron and  $f(R)$  gravity theories, the two functions interpolate the fixed values  $\mu = \gamma = 1$  for large scales  $k/a \ll m(a)$  and  $\mu = 1 + 2\beta^2(a)$  and  $\gamma = 1 - \frac{4\beta^2(a)}{1+2\beta^2(a)}$  for small scales  $k/a \gg m(a)$ . On the other hand, the DGP-like model has  $\mu = 1 + 2\beta^2(a)$  and  $\gamma = 1 - \frac{4\beta^2(a)}{1+2\beta^2(a)}$  for all  $k$ , so gravity is modified even on the largest scales.

The linear theory is useful for obtaining a qualitative understanding of the signatures to expect, but it neglects an important part of the model's behaviour, namely the screening mechanism.  $N$ -body simulations of modified gravity models, such as the ones considered here, have shown that the predictions of linear perturbation theory become inaccurate as soon as the evolution of the density perturbations starts to deviate from  $\Lambda$ CDM [3, 9, 10, 19, 35, 53]. Therefore,  $N$ -body simulations are needed to obtain accurate predictions for the non-linear evolution of these models.

### Gravitational lensing in modified gravity

Gravitational lensing is determined by the so-called lensing potential  $\Phi_+ = \frac{\Phi + \Psi}{2}$ . For the modified gravity models considered here, there is no difference to the

Newtonian potential. This can most easily be seen from the  $\gamma, \mu$  parameterisation mentioned in the previous section, which gives expression

$$\Phi_+ = \frac{(1 + \gamma)\mu}{2} \Phi_N, \quad (\text{A.28})$$

where  $\nabla^2 \Phi_N = 4\pi G a^2 \delta\rho_m$  is the Newtonian potential, i.e. the same equation as in  $\Lambda$ CDM.

When  $(1 + \gamma)\mu = 2$ , as is the case for the particular modified gravity theories studied here, lensing itself is not modified. The differences in lensing with respect to  $\Lambda$ CDM are encoded in the differences in the matter distribution caused by the modifications of gravity during the process of gravitational collapse. Modified gravity models where lensing itself is modified [3] can also be studied within the following numerical framework, but this is left for future work.

### A.3 Simulations

#### Gravitational $N$ -body code

The simulations of this chapter have been performed using the ISIS code [39] which is an adaptation of the multi-purpose  $N$ -body code RAMSES [61] for modified gravity. The DGP model has been implemented following the description laid out in [35].

Standard  $N$ -body simulations of dark matter are evolved using only two equations. First, the gravitational potential is calculated (after having used the location of the  $N$ -body particles to calculate the density field) using the Poisson equation

$$\nabla^2 \Phi_N = 4\pi G a^2 (\rho_m - \bar{\rho}_m), \quad (\text{A.29})$$

and the particles are then evolved using the geodesic equation

$$\ddot{\mathbf{x}} + 2H\dot{\mathbf{x}} = -\nabla\Phi_N. \quad (\text{A.30})$$

When going to the modified gravity models, the only change (as long as the background is close to  $\Lambda$ CDM) is that the fifth-force must be included. This adds a term  $F_\phi$  from (A.3) to the right hand side of the geodesic equation. The expression for the force terms and the corresponding field equations that are solved in the  $N$ -body code can be found below. Solving these highly non-linear differential equations is the most challenging and time-consuming part of modified gravity simulations.<sup>2</sup> All models simulated here have been simulated before; and more information and details about the implementation of the scalar field solver and modified gravity simulations in general can be found in the literature [37, 39].

<sup>2</sup>See [68] for a comparison of different codes used to simulate modified gravity. The code used here was found to compare very well (to percent accuracy) with other high-resolution codes deep into the non-linear regime.

| model          | type      | parameters   |
|----------------|-----------|--|
| $F_5$          | $f(R)$    | $ f_{R0}  = 10^{-5}, n = 1$  |
| $F_6$          | $f(R)$    | $ f_{R0}  = 10^{-6}, n = 1$  |
| Symm. $A$      | symmetron | $\lambda_\phi = 1.0 \text{ Mpc}/h, a_{\text{SSB}} = 0.50, \beta_0 = 1.0$ |
| Symm. $B$      | symmetron | $\lambda_\phi = 1.0 \text{ Mpc}/h, a_{\text{SSB}} = 0.33, \beta_0 = 1.0$ |
| DGP, $r = 1.2$ | DGP       | $r_c H_0 = 1.2$  |
| DGP, $r = 5.6$ | DGP       | $r_c H_0 = 5.6$  |

Table A.1: The modified gravity models which are used for  $N$ -body simulations. The background cosmology in each simulation is a standard  $\Lambda$ CDM cosmology with  $\Omega_m = 0.271$ ,  $\Omega_\Lambda = 0.729$ ,  $h = 0.703$ ,  $n_s = 0.966$  and  $\sigma_8 = 0.8$ .

The code was also part in a recent code comparison project for modified gravity  $N$ -body codes [68] and it was found to agree to the  $\sim 1\%$  level deep into the non-linear regime ( $k \sim 5 h/\text{Mpc}$ ) with similar codes for the models simulated for this work.

The simulations performed all start from the same initial conditions and are run with  $N = 512^3$  particles in a box of size  $B_0 = 250.0 \text{ Mpc}/h$  and with a  $\Lambda$ CDM cosmology given by  $\Omega_m = 0.271$ ,  $\Omega_\Lambda = 0.729$ ,  $h = 0.703$ ,  $n_s = 0.966$  and  $\sigma_8 = 0.8$ . For each simulation, output of the particles for the lensing analysis is done at redshifts  $z = 0.000, 0.046, 0.111, 0.176, 0.244, 0.333, 0.422, 0.538, 0.660, 0.818, 1.000, 1.250, 1.500, 1.750, \text{ and } 1.981$ .

The simulated modified gravity models are the Hu-Sawicky  $f(R)$  model, the symmetron model, and the normal branch DGP model. Table A.1 lists the parameters used in the simulations.<sup>3</sup> The background evolution in each modified gravity simulation corresponds to  $\Lambda$ CDM, allowing for the direct comparison of the effect of the fifth-force (and the corresponding screening mechanism).

**Field equations.** For completeness, the field equations solved in the  $N$ -body code for the different modified gravity models are presented here. In the equations, the quasi-static approximation has been applied [7, 38, 43, 66]. The equation of motion for particles in the  $N$ -body simulations can be written in the form

$$\ddot{\mathbf{x}} + 2H\dot{\mathbf{x}} = -\nabla\Phi_N - \mathbf{F}_\phi, \quad (\text{A.31})$$

where  $\nabla^2\Phi_N = 4\pi G a^2(\rho_m - \bar{\rho}_m)$  is the Newtonian potential and  $\mathbf{F}_\phi$  is the fifth-force.

<sup>3</sup>With the chosen parameters, the DGP model with  $r_c H_0 = 1.2$  ( $r_c H_0 = 5.6$ ) has the same value of  $\sigma_8$  as the  $f(R)$  model with  $f_{R0} = 10^{-5}$  ( $f_{R0} = 10^{-5}$ ).

**$f(\mathbf{R})$**  For the Hu-Sawicky  $f(R)$  model it follows that

$$\mathbf{F}_\phi = -\frac{1}{2}\nabla f_R, \quad (\text{A.32})$$

where the scalar field  $f_R$  is determined by

$$\nabla^2 f_R = -\Omega_m H_0^2 a^2 \left( \frac{\rho_m}{\bar{\rho}_m} - 1 \right) + a^2 H_0^2 \Omega_m \left[ \left( 1 + 4 \frac{\Omega_\Lambda}{\Omega_m} \right) \left( \frac{f_{R0}}{f_R} \right)^{n+1} - a^{-3} - 4 \frac{\Omega_\Lambda}{\Omega_m} \right]. \quad (\text{A.33})$$

**Symmetron** For the symmetron model it follows that

$$\mathbf{F}_\phi = \frac{6\Omega_m (H_0 \lambda_\phi)^2 \beta_0^2}{a_{\text{ssb}}^3} \chi \nabla \chi, \quad (\text{A.34})$$

where the scalar field  $\chi$  is determined by

$$\nabla^2 \chi = \frac{a^2}{a \lambda_\phi^2} \left( \frac{a_{\text{ssb}}^3 \rho_m}{a^3 \bar{\rho}_m} \chi - \chi + \chi^3 \right). \quad (\text{A.35})$$

**DGP** For the DGP model it follows that

$$\mathbf{F}_\phi = \frac{1}{2}\nabla \phi, \quad (\text{A.36})$$

where the scalar field  $\phi$  is determined by

$$\nabla^2 \phi + \frac{r_c^2}{3\beta_{\text{DGP}}(a)a^2} \left( (\nabla^2 \phi)^2 - (\nabla_i \nabla_j \phi)^2 \right) = \frac{H_0^2}{a\beta_{\text{DGP}}} \frac{\delta\rho_m}{\bar{\rho}_m}. \quad (\text{A.37})$$

### Lensing pipeline

Light passing through an inhomogeneous matter field is deflected by the intervening large-scale structure. This effect, called *cosmic shear*, promises to be a powerful probe of cosmology. As long as  $\Psi = \Phi$  holds for the gravitational potential, the cosmic deflection potential for a light cone out to comoving distance  $\chi$  is given by [20, 55]

$$\psi(\boldsymbol{\theta}) = \frac{2}{c^2} \int_0^\chi \frac{D_A(\chi - \chi')}{D_A(\chi) D_A(\chi')} \Phi(D_A(\chi') \boldsymbol{\theta}, \chi') d\chi', \quad (\text{A.38})$$

where  $D_A$  is the comoving angular diameter distance. The deflection potential is sourced by an effective dimensionless surface mass density

$$\kappa(\boldsymbol{\theta}) = \frac{3H_0^2 \Omega_m}{2c^2} \int_0^\chi \frac{D_A(\chi') D_A(\chi - \chi')}{D_A(\chi)} \frac{\delta(D_A(\chi') \boldsymbol{\theta}, \chi')}{a(\chi')} d\chi', \quad (\text{A.39})$$

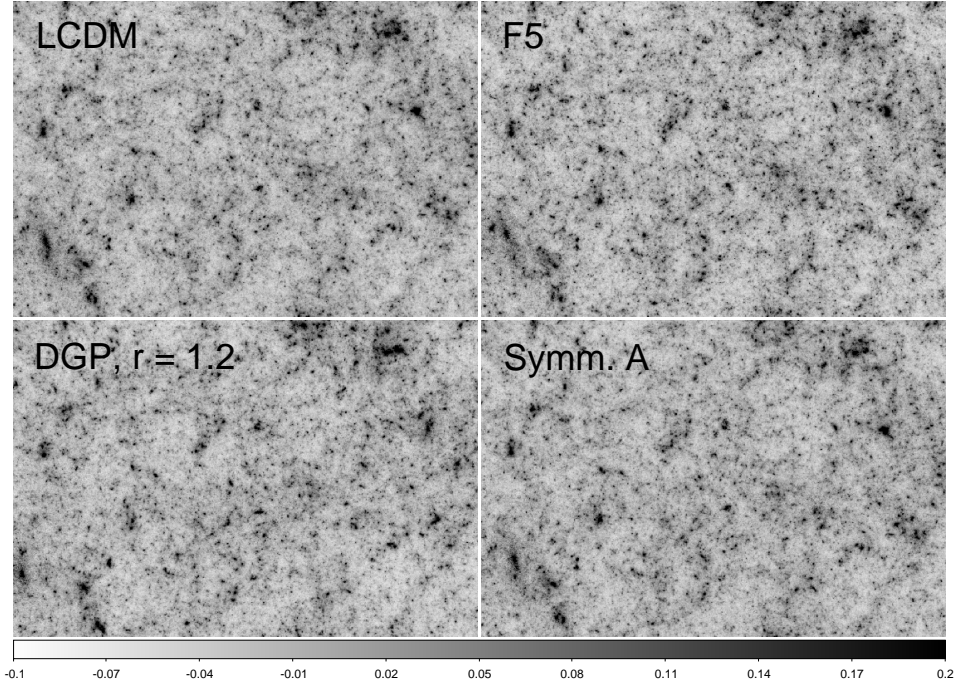


Figure A.1: Comparison of a  $1.85 \text{ deg} \times 1.25 \text{ deg}$  field of view of the convergence  $\kappa$  in  $\Lambda\text{CDM}$  and the modified gravity models, using a source redshift  $z_s = 2$ . All four panels show the same light cone extracted from the respective simulations. The convergence maps were simulated with the GLAMER pipeline for gravitational lensing.

where  $\delta$  is the matter density contrast  $\Delta\rho/\rho$ .

Extracting lensing quantities from simulations using (A.38) and (A.39) is cumbersome and numerically intensive, as each calculation and each desired source redshift involves raytracing through the simulation volume. Instead, weak lensing by the large-scale structure is simulated using the multi-plane approach of the GLAMER lensing pipeline [40, 47]. An observed light cone is first segmented in the radial direction into a number of slices, and the three-dimensional mass distribution in each slice is projected onto a plane at the mean comoving distance of that slice. The resulting two-dimensional surface mass density maps  $\kappa_i$ ,  $i = 1, 2, \dots$  serve as lensing planes for GLAMER, which traces the propagation of light from plane to plane using the deflection angle

$$\boldsymbol{\alpha}_i = \nabla\psi_i \quad (\text{A.40})$$

and the Poisson equation [47]

$$\nabla^2\psi_i = 2\kappa_i \quad (\text{A.41})$$

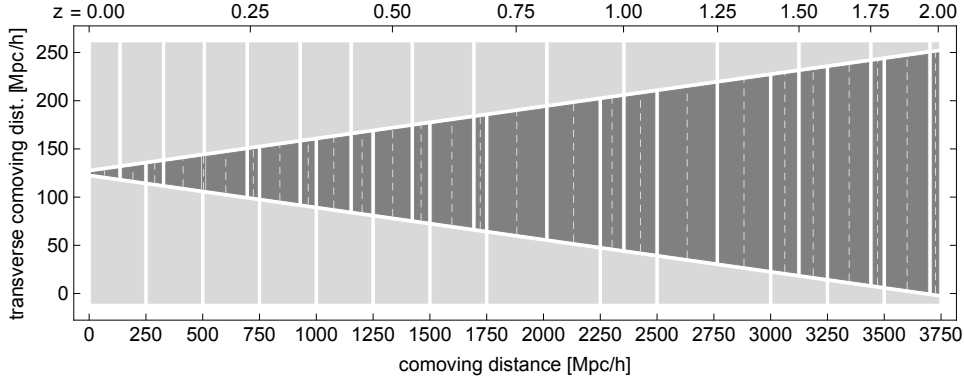


Figure A.2: Light cone construction with MAPSIM for the  $\Lambda$ CDM simulation. The simulation box size is  $B_0 = 250 \text{ Mpc}/h$ . The dark shaded area is the light cone, growing to a transverse comoving size equal to the box size  $B_0$ . The mass distribution in each of the individual light cone segments is projected onto a lensing plane at the centre of the segment (dashed line). The regions above the light cone indicate the simulation snapshots used to construct each segment. The regions below the light cone indicate groups of segments that have been randomised in the same way.

which relates the surface mass density  $\kappa_i$  to the Laplacian of the deflection potential  $\nabla^2 \psi_i$  on each plane. Having thus constructed the lensing simulation, one is free to place a source plane at any redshift inside the light cone (i.e. a delta distribution of source redshifts), and calculate maps of lensing quantities such as the convergence  $\kappa$  or the shear  $\gamma$  for an observer at redshift zero. Sample convergence maps for the  $\Lambda$ CDM,  $f(R)$ , symmetron, and DGP simulations are shown in Figure A.1.

The construction of light cones from simulations and the projection of the mass distribution onto individual planes is done by the MAPSIM tool [23] in a single step. Each light cone is constructed up to redshift  $z_{\text{max}} = 2.0$ , which is thus the highest source redshift available for the lensing maps. The field of view of the light cone is a square with a side length of  $3.85 \text{ deg}$ , which is the angle subtended by the simulation box size  $B_0$  at redshift  $z_{\text{max}}$ , giving a total area of  $14.82 \text{ deg}^2$ .

Figure A.2 shows the schematic construction of a light cone for the  $\Lambda$ CDM simulation. It is clear that for lower redshifts, much of the simulation box volume is unused. Randomisation of the box volume through rotation and translation offers a way to extract multiple light cones from a single simulation [30], where each of the light cones ends up with a random portion of the simulation box.

MAPSIM constructs a light cone by randomly picking an origin and orientation of the box volume, defining zero comoving distance and the direction of the line of sight. Increasing the comoving distance, particles in the field of view are

mapped into the light cone, making use of the periodic boundary conditions of the simulation box. This continues until the comoving distance is a multiple of the simulation box size  $B_0$ , changing snapshots as they become a better fit for current redshift. The process is repeated, starting from the randomisation, until the whole light cone has been constructed.

Using the technique laid out above, ten randomised light cones are extracted from each of the simulations and gravitational lensing of the contained large scale structure is simulated. Lensing maps of the convergence fields  $\kappa$  are then created for source redshifts  $z_S = 0.5, 1.0, 1.5, 2.0$ . These maps have a size of  $2048 \times 2048$  pixels for the aforementioned field of view of  $3.85 \text{ deg} \times 3.85 \text{ deg}$ , resulting in an angular resolution of 6.77 arcsec per pixel. It is noted that since the simulation box fills the whole field of view at  $z = 2.0$ , the same large-scale structure is present in each light cone for the higher redshift slices. It is thus expected that the sample variance is underestimated with increasing redshift.

## A.4 Results

### Matter power spectrum

The matter power spectrum is defined via

$$\langle \delta_m(\mathbf{k}) \delta_m(\mathbf{q}) \rangle = (2\pi)^3 \delta^{(3)}(\mathbf{k} + \mathbf{q}) P(k), \quad (\text{A.42})$$

where  $\delta_m(\mathbf{k})$  is Fourier transform of the density field  $\delta_m(\mathbf{x}) \equiv \rho_m(\mathbf{x})/\bar{\rho}_m - 1$ . The matter power spectrum is calculated for all of the simulations using POWMES [17]. The power spectra obtained agree well with previous  $N$ -body simulations of the same models [10, 19, 35, 37, 39, 45, 49], and serve as a good cross-check for the validity of the results. Also computed are both the linear predictions (A.18), and the HALOFIT [56] predictions for the non-linear power spectrum using MGCAMB [26]. This latter code is a modified gravity modification of the Boltzmann-code CAMB [34] and uses the improved fitting formula (designed for  $\Lambda$ CDM) of [59] to get better agreement with simulations on small scales. The fractional difference of the matter power spectrum with respect to  $\Lambda$ CDM as a function of redshift can be seen in Figure A.3 for the  $f(R)$ , symmetron, and DGP models, respectively.

Before the results are discussed in more detail, it shall be noted that, overall, the results confirm the qualitative features discussed in Section A.2. For  $f(R)$  and the symmetron model, it can be seen that the power spectrum approaches  $\Lambda$ CDM on large scales, while for DGP there are modifications on all scales. Furthermore, comparing the full simulation results with the predictions of linear theory shows the effect of screening: linear theory greatly overestimates the amount of clustering on small scales. This confirms the point made above: non-linear effects are crucial for accurately modelling the effects of gravitational screening and methods such as those presented in this chapter, play an essential role. The HALOFIT predictions will be discussed in more detail below.

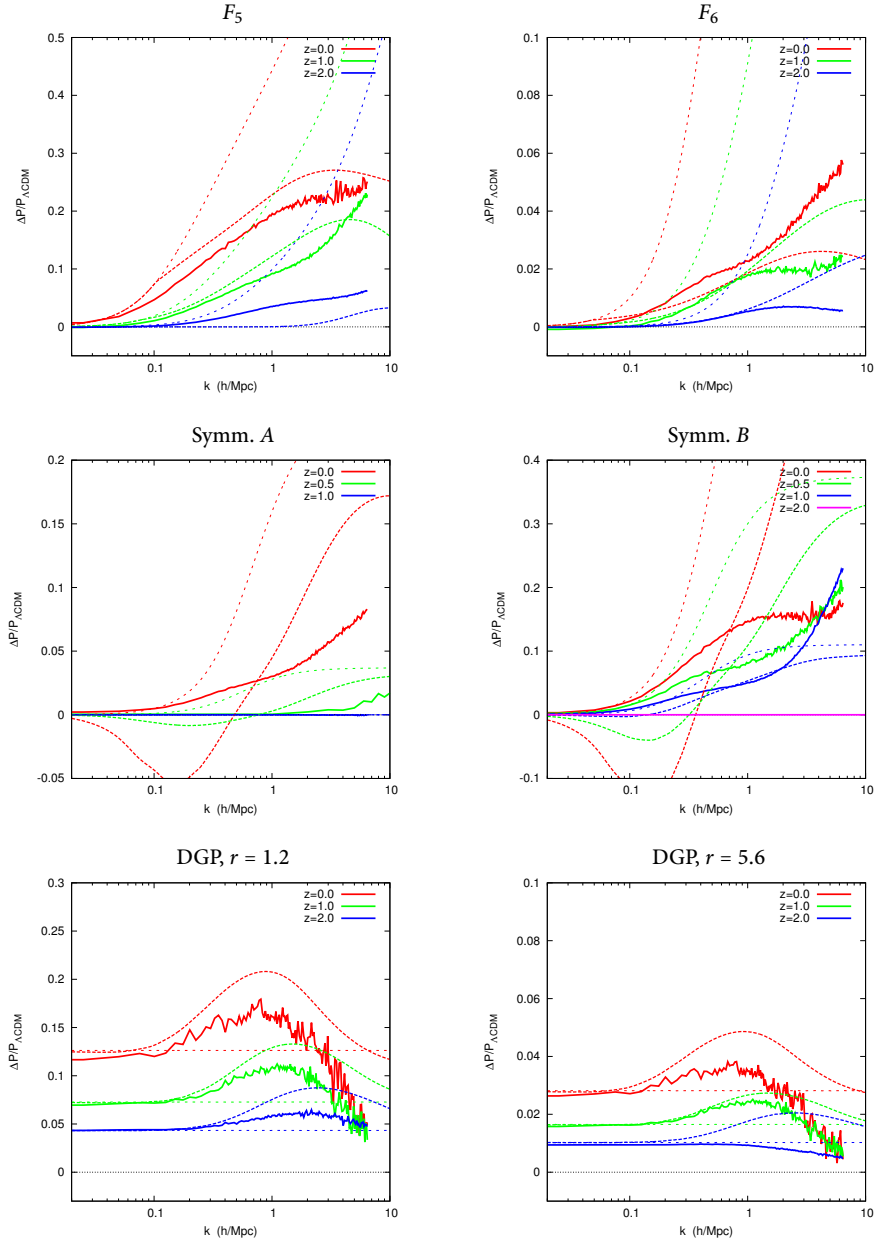


Figure A.3: The fractional difference in the matter power spectrum with respect to  $\Lambda$ CDM for the  $f(R)$ , symmetron, and DGP models. The thin dotted lines shows the linear perturbation theory and the dashed lines shows the HALOFIT predictions (using the HALOFIT fitting function of MGCAMB for  $f(R)$ ).

**$f(R)$**  For this model, modifications to gravity boost structure formation on small scales. Furthermore, one finds that  $P(k) \simeq P(k)_{\Lambda\text{CDM}}$  for scales  $k \lesssim 0.05 h/\text{Mpc}$  and over all times. The effects are stronger in the  $F_5$  model than in the  $F_6$  model and this is due to the larger range (A.22) of the fifth-force in the former simulation. For the  $F_5$  ( $F_6$ ) model it can be seen that the matter power spectrum is enhanced by up to  $\approx 25\%$  ( $\approx 2\text{--}5\%$ ) at  $z = 0$  for non-linear scales  $k \sim 1\text{--}10 h/\text{Mpc}$ . At  $z = 2$  the deviations from  $\Lambda\text{CDM}$  are below 5% and 1% for all scales in the  $F_5$  and  $F_6$  model respectively. At earlier times the modifications are even smaller and thus, for these models, modifications to gravity only have a potentially observable impact on structure formation at late times,  $z \lesssim 2$ . The main reason for this is that the range (A.22) of the scalar field decreases rapidly as one approaches higher redshifts. Comparing the results of linear perturbation theory with the simulated results, it is clear that the amount of clustering is greatly overestimated in linear theory. For example, at  $k = 1 h/\text{Mpc}$  and  $z = 0$ , linear theory predicts a modification of  $\approx 50\%$  in the  $F_5$  model whereas the actual result is closer to  $\approx 20\%$ .

**Symmetron** Modifications of gravity in the symmetron model follow the same pattern as in  $f(R)$  gravity, where structure formation is boosted on small scales. The effects are stronger in the  $B$  model than in the  $A$  model. The reason for this is the smaller value of  $a_{\text{ssb}}$  in the former simulation, which means that the fifth-force has been active for a longer period of cosmic time. The fifth-force is not in operation before the time of symmetry breaking  $a = a_{\text{ssb}}$  and consequently the power spectrum is the same as in  $\Lambda\text{CDM}$  for earlier times  $a < a_{\text{ssb}}$ . For the  $A$  ( $B$ ) model, one sees that the matter power spectrum is enhanced by up to  $\approx 15\%$  ( $\approx 5\%$ ) at  $z = 0$  for non-linear scales  $k \sim 1\text{--}10 h/\text{Mpc}$ . Linear theory is an even worse fit to the simulation results in the symmetron model than in  $f(R)$  gravity. At  $k = 1 h/\text{Mpc}$  at  $z = 0$  one finds an  $\approx 2\%$  modification for the  $B$  model whereas linear theory predicts almost 20%. This larger deviation can be attributed to the stronger screening mechanism in the symmetron model, i.e. the fact that  $\beta \propto \phi$  leads to additional screening on small scales (and high density regions) where  $\phi$  is clustered close to  $\phi = 0$ .

**DGP** Contrary to the two models discussed above, gravity is modified on all scales in the DGP model. At  $z = 0$  one finds that structure formation in the  $r_c H_0 = 1.2$  ( $= 5.6$ ) model is enhanced by  $\approx 12\%$  ( $\approx 3\%$ ). Going to earlier times the modifications become smaller and, at  $z = 2$ , are less than  $\approx 4\%$  and  $\approx 1\%$  in the two models, respectively. Since  $\beta_{\text{DGP}}$  increases with increasing  $r_c$  one expects that a larger  $r_c$  leads to stronger modifications, and this is indeed the case in the results. On highly non-linear scales  $k \gtrsim 5 h/\text{Mpc}$ , deviations in the power spectrum are seen to drop for both simulations and at  $k = 10 h/\text{Mpc}$  they are very close to the  $\Lambda\text{CDM}$  prediction. This is due to the Vainshtein mechanism being in play and reducing the effects of the fifth-force on the small-scale structure formation. It can also be seen that for the two chosen models for the simulation, the

relative difference  $\Delta P/P_{\Lambda\text{CDM}}$  has a similar shape at all three redshifts depicted in Figure A.3, while the amplitude is markedly different.

### Convergence power spectrum

Similar to the power spectrum (A.42), the convergence power spectrum  $C_\ell$  is formally defined by

$$\langle \hat{\kappa}(\boldsymbol{\ell})\hat{\kappa}(\boldsymbol{\ell}') \rangle = (2\pi)^2 \delta^{(2)}(\boldsymbol{\ell} + \boldsymbol{\ell}') C_\ell, \quad (\text{A.43})$$

where  $\ell$  denotes the angular mode. The convergence power spectrum is an important cosmological probe, as it can be related to the evolution history of the universe via Limber's approximation through

$$C_l(z_s) = \frac{9\Omega_m^2 H_0^4}{4} \int_0^{z_s} dz \frac{g^2(z)(1+z)^2}{\chi^2(z)H(z)} P(k=l/r(z), z) \quad (\text{A.44})$$

where  $P(k, z)$  is the matter power spectrum at redshift  $z$  and  $g(z)$  is the lensing weight. For a single source plane at  $z = z_s$  one has  $g(z) = \chi(z)(\chi(z) - \chi(z_s))/\chi(z_s)$  where  $\chi(z)$  is the co-moving distance. This is a powerful combination of many cosmological quantities which can help break degeneracies arising in other probes. The convergence power spectrum is also directly related to all observed quadratic statistics of cosmic shear measurements, and might soon be measured directly [24, 33].

In order to estimate the power spectrum from the simulated convergence maps, one uses

$$C_\ell = \frac{1}{A} \langle |\hat{\kappa}(\boldsymbol{\ell})|^2 \rangle, \quad (\text{A.45})$$

where  $\hat{\kappa}$  is the Fourier transform of the convergence field, and the averaging is done over the angle of vector  $\boldsymbol{\ell}$ . In practice,  $\hat{\kappa}$  is calculated via a Fast Fourier Transform of the convergence maps (after zero-padding to mitigate boundary effects), and performing the averaging in bins of  $\Delta\ell$  with logarithmic spacing. By calculating the convergence power spectrum separately for each simulated light cone, one arrives at a sample of results which further give a handle on the sample variance of the results. The estimated power spectra for the respective  $f(R)$ , symmetron, and DGP models are shown in Figure A.4.

To estimate up to which  $\ell$  the results are trustworthy, the relative contribution to  $C_\ell$  coming from different ranges of co-moving modes of the matter power spectrum is computed. The result can be seen in Figure A.5. The simulations performed here have a particle Nyquist frequency of  $k_{\text{Ny}} \simeq 6.5 h/\text{Mpc}$ . Fixed-grid simulations with different box sizes usually start to deviate from each other for modes larger than  $k \sim k_{\text{Ny}}/4 - k_{\text{Ny}}/2$ , resulting in  $k_{\text{max}} \sim 2-3 h/\text{Mpc}$  and  $\ell_{\text{max}} \sim 2000-3000$ . However, the simulations have adaptive refinements, which means that the effective Nyquist frequency is much larger and a rough estimate

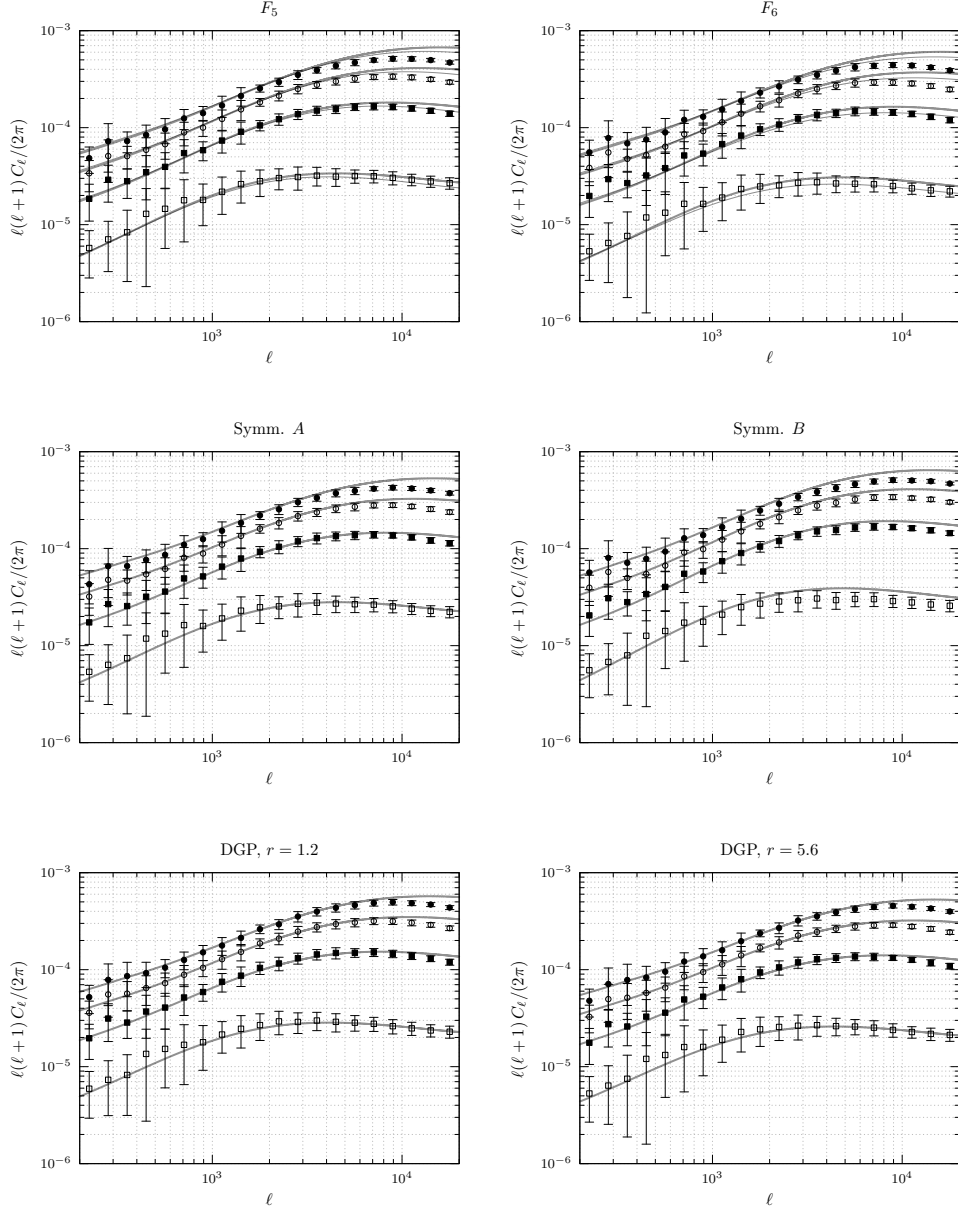


Figure A.4: Dimensionless convergence power spectra  $\ell(\ell+1)C_\ell$  for the  $f(R)$ , symmetron, and DGP simulations at source plane redshifts  $z_S = 0.5, 1.0, 1.5, 2.0$  (bottom to top). Shown are the  $1\sigma$  error bars over the sample of realisations. Also shown are the predictions obtained from HALOFIT (thick) and, in the case of  $f(R)$ , MGHALOFIT (thin).

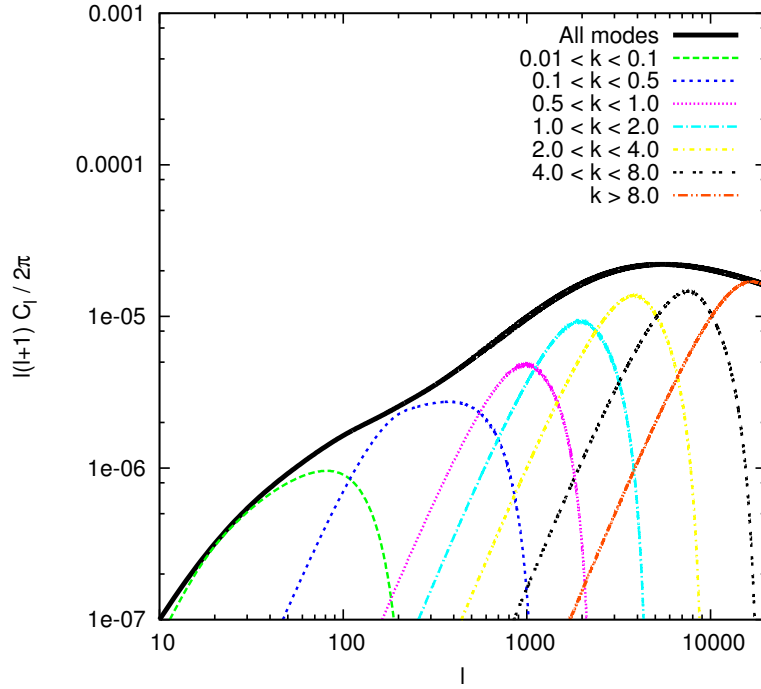


Figure A.5: Shown are the relative contribution to the convergence power spectrum from different ranges of co-moving Fourier modes of the density fluctuations. The plot is made by computing the HALOFIT prediction for  $C_\ell$  and taking  $P(k, z) = 0$  for  $k$  values outside the range indicated in the plot. The source is here at  $z = 1.0$ .

from the refinement structure gives a factor 5–10 at  $z = 0.0$ . From this it follows one can trust the  $C_\ell$  spectra up to  $\ell_{\max} \sim 10^4$ . For the largest source redshift  $z_s = 2.0$  this  $\ell_{\max}$  value is probably too large due to the lack of refinement at early times. The minimum  $\ell$ -value one can study is fixed by the simulation box size  $B_0 = 250 \text{ Mpc}/h$ , corresponding to values of  $k_{\min} = 0.025 \text{ h}/\text{Mpc}$  and  $\ell_{\min} \sim 100$  (Figure A.5).

### Evolution of the convergence power spectrum

At first, the redshift evolution of the non-linear power spectrum will be investigated<sup>4</sup> in the screened models relative to a reference  $\Lambda\text{CDM}$  simulation (Figure A.6). The reason for this is twofold: First, as noted before, one expects a loss of power in the high  $z$ , high  $\ell$  regime due to the lack of refinement of the simulations at early times. However, this loss of power is consistent among the different simulations, which all evolved with the same refinement settings. Although deep

<sup>4</sup>See [54] for a discussion on the effect of modified gravity on the weak lensing convergence power spectrum at linear scales.

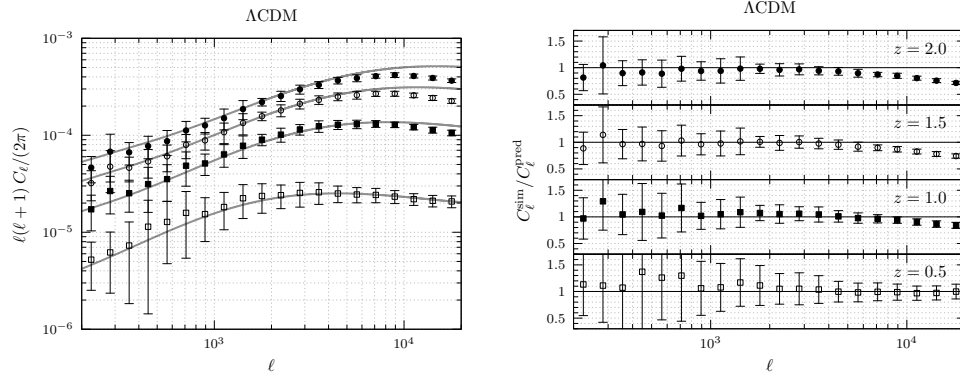


Figure A.6: *Left*: Dimensionless convergence power spectrum  $\ell(\ell + 1) C_\ell$  for the  $\Lambda$ CDM simulation at source plane redshifts  $z_s = 0.5, 1.0, 1.5, 2.0$  (bottom to top). Shown are the  $1\sigma$  error bars over the sample of realisations. Also shown is the prediction obtained from HALOFIT. *Right*: Difference between the  $\Lambda$ CDM simulation and predictions from CAMB.

in the non-linear regime, and the effect of resolution may be different for different models, one still expects that the power ratio  $C_\ell/C_\ell^{\Lambda\text{CDM}}$  with respect to  $\Lambda$ CDM will be close to the true value over the full range up to  $\ell_{\text{max}} \sim 10^4$  and indicative of the differences one might find at higher resolution. Another reason for investigating the power ratio is of a more physical nature. If  $C_\ell/C_\ell^{\Lambda\text{CDM}}$  is constant in both redshift  $z$  and mode  $\ell$ , it is in principle indistinguishable from  $\Lambda$ CDM with a different normalisation of the power spectrum. If  $C_\ell/C_\ell^{\Lambda\text{CDM}}$  only depends on  $z$  (and not  $\ell$ ), it might also be indistinguishable from  $\Lambda$ CDM with a different background history. Thus a robust signature of modified gravity requires an evolution in both redshift and scale.

To robustly estimate  $C_\ell/C_\ell^{\Lambda\text{CDM}}$  at a given redshift, the convergence power spectra  $C_\ell$  and  $C_\ell^{\Lambda\text{CDM}}$  are calculated for the same light cone taken from a screened model and the  $\Lambda$ CDM simulation. Given that all simulations start from the same initial conditions, both power spectra trace the evolution of the same patch of the universe, and the ratio  $C_\ell/C_\ell^{\Lambda\text{CDM}}$  is an estimator with much of the influence of cosmic variance taken out. Only after the individual ratios  $C_\ell/C_\ell^{\Lambda\text{CDM}}$  have been calculated in this way are also the mean and variance over the sample of light cones calculated. The results for the ratio  $C_\ell/C_\ell^{\Lambda\text{CDM}}$  can be seen in Figure A.7 for the respective  $f(R)$ , symmetron, and DGP models. As intended, the sample variance has been greatly reduced, especially in the region of intermediate  $\ell$ . Below the results will be discussed in more details for the three types of models individually.

**$f(R)$**  The convergence power spectrum in  $f(R)$  shows the same qualitative behaviour as the matter power spectrum. On large scales ( $\ell \lesssim \mathcal{O}(100)$ ) the fractional difference w.r.t.  $\Lambda$ CDM is close to zero whereas for small angular scales there are

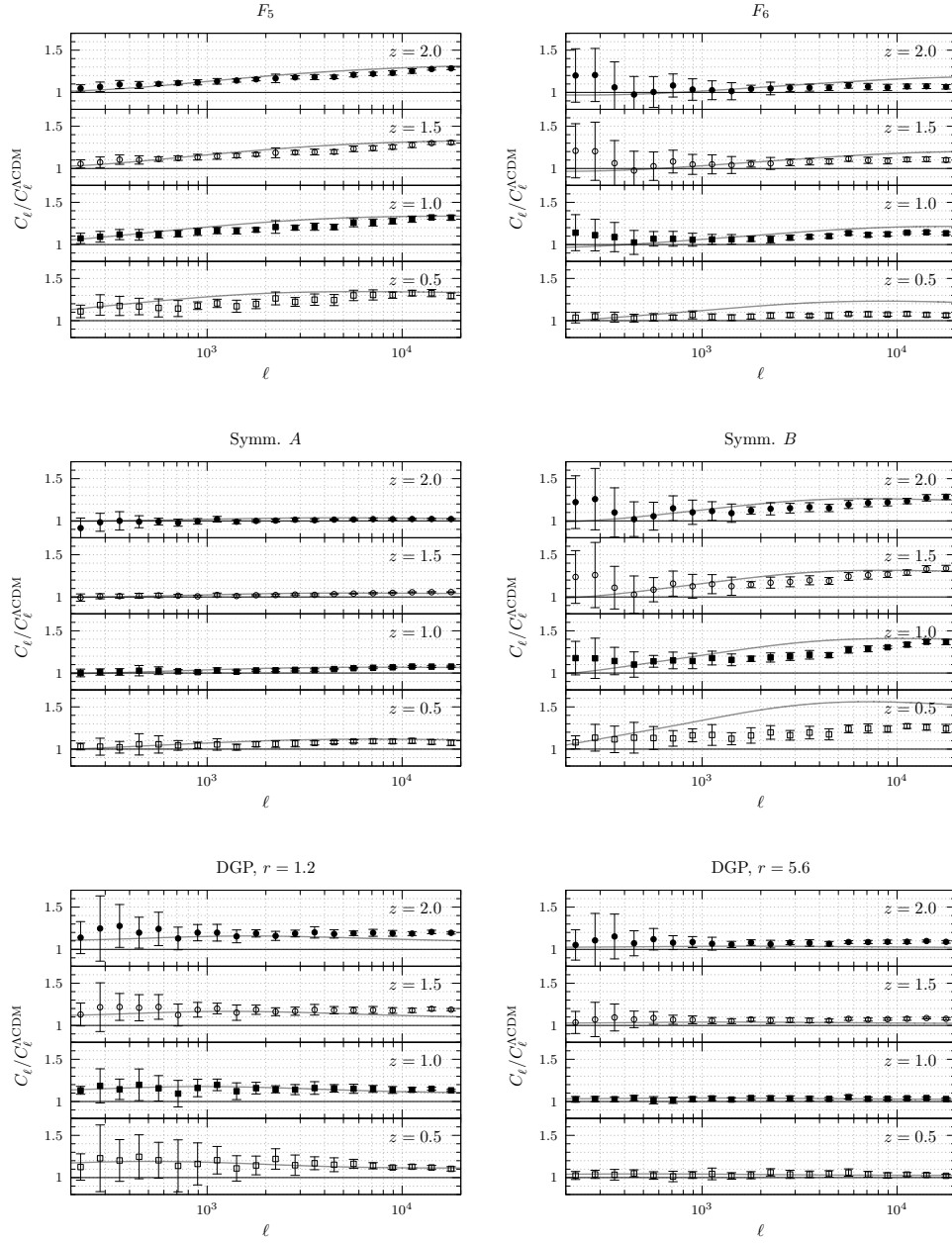


Figure A.7: The fractional difference in the convergence power spectra for the  $f(R)$ , symmetron, and DGP simulations with respect to  $\Lambda\text{CDM}$  for four source redshifts. Also shown are the predictions obtained from HALOFIT.

large deviations. In the  $F_6$  model the deviation from  $\Lambda$ CDM is consistent (ignoring the error bars) with zero for all source redshifts and  $\ell \lesssim 10^3$  whereas for the  $F_5$  model there is a non-zero deviation for all  $\ell \gtrsim 10^2$ . The ratio  $C_\ell/C_\ell^{\Lambda\text{CDM}}$  increases for both models with the angular scale and at  $l \sim 10^4$  there is a  $\approx 20 - 30\%$  ( $\approx 5 - 10\%$ ) signal for the  $F_5$  ( $F_6$ ) model, depending on source redshift.

**Symmetron** For the symmetron simulations, the same trend as for  $f(R)$  is seen in the convergence power spectrum, but with some important differences. The fractional difference w.r.t.  $\Lambda$ CDM grows with  $\ell$  and for  $l \sim 10^4$  there is a  $\approx 2-5\%$  ( $\approx 20-30\%$ ) deviation for the  $A$  ( $B$ ) model depending on source redshift. As opposed to the  $f(R)$  model, the modifications of gravity are completely absent for  $a < a_{\text{ssb}}$  for the symmetron. It is only close to the present time that the fifth-force has had time to produce a significant difference in the matter power spectrum and thus, for the simulation with  $a_{\text{ssb}} = 0.5$ , light from high redshift sources propagates mostly through a  $\Lambda$ CDM universe. Because of this, the  $C_\ell$ 's for the  $A$  model are very close to  $\Lambda$ CDM at  $z = 2.0$ . As the source redshift moves closer to the present, more modifications to large-scale structure appear, and therefore larger deviations in the convergence power spectrum.

**DGP** In the DGP model, gravity is modified even on the largest scales and there is a corresponding deviation at small values of  $\ell$  down to the linear regime. The fractional difference w.r.t.  $\Lambda$ CDM on large scales is found to be of similar order as in the matter power spectrum over the range  $0 < z < 2$ . For the  $r_c H_0 = 1.2$  ( $r_c H_0 = 5.6$ ) model there is a  $\approx 10-15\%$  ( $\approx 5-10\%$ ) deviation depending on source redshift. The deviation is, within the given error bars, fairly  $\ell$ -independent, but there is in fact a slight drop-off of the signal for large  $\ell$  that is consistent with the results found in the matter power spectrum (Figure A.3). Contrary to the symmetron and  $f(R)$  models, there is a redshift-dependency of the signal that is close to a pure scaling of the amplitude.

### Semi-analytical predictions

One can try and approximate the non-linear effects using semi-analytic methods such as e.g. HALOFIT that perform well in the context of  $\Lambda$ CDM. These power spectra, generated through a modified version of HALOFIT, can give better agreement with the  $N$ -body simulations than linear theory, but even here the predictions for some models (and model parameters) can also be very poor. This is to be expected as there is no screening included in the formalism and the HALOFIT prediction is a function of the linear  $P(k, a)$  only. Nevertheless, for *specific* models, it is possible to obtain good approximations. There do exist other approaches for predicting the non-linear matter power spectrum (or equivalently  $\Delta P/P_{\Lambda\text{CDM}}$ ) than HALOFIT which might do better [8], but HALOFIT is the most widely used method to obtain non-linear predictions for the matter power spectrum. Below

the ability of HALOFIT to predict both the matter and convergence power spectra for the three models is discussed.

**$f(R)$**  For  $f(R)$  gravity, Figure A.3 shows that the linear predictions are a poor match to the simulation results for the matter power spectrum and this also holds for the convergence power spectrum. The HALOFIT code<sup>5</sup> is able to improve significantly on this. For the  $F_5$  model, the HALOFIT predictions for the convergence power spectrum (Figure A.4, Figure A.7) are roughly within the error bars for most of the  $\ell$ -range considered here. Much of this good agreement can be attributed to the model-specific fitting formula used in MGCAMB to correct HALOFIT. This fitting formula is a 40 parameter fit to  $f(R)$  simulations, hence the good level of agreement is not surprising. For the  $F_6$  model, which is more strongly screened, there is a larger deviation for the low redshift sources and for  $\ell = 10^3 - 10^4$  HALOFIT predicts a  $\approx 10\%$  signal whereas the simulations shows only  $\approx 5\%$ .

**Symmetron** For the symmetron there does not exist a fitting formula for the non-linear  $P(k)$  to be used in HALOFIT. In the bottom panel of Fig. A.3, it is clear that HALOFIT gives a very poor fit for the matter power spectrum. It underestimates the power for scales  $k \lesssim 0.5 h/\text{Mpc}$  and overestimates the power for  $k \gtrsim 0.5 h/\text{Mpc}$ . However when using these results to compute the convergence power spectrum, see Figure A.4, A.7, there is a good agreement for the  $A$  model whereas the HALOFIT predictions show the largest deviations from the simulation results. This is a coincidence that comes from the process of integrating the matter power spectrum (A.44) to compute  $C_\ell$ , for which the over-/underestimation of the power gets averaged out. For the  $B$  model, there is a larger deviation for the low redshift sources, just as for  $f(R)$  above, and for  $\ell = 10^3 - 10^4$  HALOFIT predicts a  $\approx 50\%$  signal whereas the simulations show only  $\approx 10\%$ .

**DGP** For the DGP model, the HALOFIT predictions are fairly good for both the matter power spectrum and the convergence power spectrum. The main reason for this is that the linear power spectrum is a much better (but far from good enough) approximation to the non-linear power spectrum than it is in the other two models considered here.

In general, the HALOFIT predictions are able to capture the signal, at least qualitatively. However, there is a big difference for the model parameters when screening is largest. This illustrates how hard it is to accurately predict the signal of these models on deep non-linear scales, and more elaborate methods are needed to get the necessary accuracy to constrain these models using data from future weak-lensing surveys in the deep non-linear regime.

<sup>5</sup>HALOFIT in this subsection refers to the modified version provided with MGCAMB [69].

## A.5 Discussion

This chapter investigated the weak lensing signatures of modified gravity theories that have a screening mechanism in the deep non-linear regime. High-resolution  $N$ -body simulations of modified gravity models have been performed which were selected to cover the most common screening mechanisms discussed in the literature. The output of the simulations was then processed by MAPSIM, which extracts randomised light cones from simulation snapshots, collapsing all particles within a given light cone onto a number of planes suitable for lensing. These light cones contain the large-scale structure of the modified gravity theories and, using the GLAMER lensing pipeline, realistic convergence maps as observed by weak lensing were created.

An analysis of the convergence power spectrum in screened theories of modified gravity was performed in two steps: First, the convergence power spectrum  $C_\ell$  was extracted directly from the Fourier transform of the generated convergence maps. The results for  $\Lambda$ CDM are in good agreement with semi-analytical predictions up to  $\ell \gtrsim 10^3$ , as well as previous studies. For higher values of  $\ell$ , there is a loss in power which can be attributed to resolution effects, while the lower values of  $\ell$  have a large uncertainty due to the variance within the limited sample size. To combat these effects, the convergence power spectrum  $C_\ell/C_\ell^{\Lambda\text{CDM}}$  was extracted relative to a  $\Lambda$ CDM reference simulation for each individual light cone before averaging over realisations. Since all simulations start from the same initial conditions, this procedure reduces the influence of randomness by only considering the relative increase in power between theories of gravity. The effects of a loss of power due to limited resolution are then mitigated and the final result is a clear indicator of the signal one can expect when searching for the deviations of screened theories from  $\Lambda$ CDM.

For the particular modified gravity models simulated here —  $f(R)$  gravity, the symmetron and the normal branch DGP model — parameters were selected which are close to the limits that are set by local gravity experiments. For these parameters, deviations of up to  $\approx 50\%$  were found in the convergence power spectrum in the deep non-linear regime  $\ell \sim 10^4$ . The scale ( $\ell$ ) and source redshift dependence of the signal for these models is such that they cannot be mimicked by a  $\Lambda$ CDM model with a different value of  $\Omega_m/\sigma_8$ , which is promising for detecting this signal in future weak lensing surveys. However the deep non-linear regime is also where baryonic effects<sup>6</sup> and the effects of neutrinos on the power spectrum are non-negligible. These effects can be highly degenerate with the modified gravity signal [2], and a more detailed study is required to quantify these degeneracies.

The simulation results for the matter and convergence power spectra were also compared to the predictions of linear perturbation theory and those found from applying the HALOFIT prescription. Performing modified gravity simulations is computationally expensive, so having an accurate prescription for predicting the

<sup>6</sup>See e.g. [63] for a study of baryonic effects on the convergence power spectrum.

modified gravity signal in the non-linear regime is of great value. It was found that linear perturbation theory (meaning the prediction for the ratio  $P_{\text{MG}}/P_{\Lambda\text{CDM}}$  is calculated in linear theory) is a very bad approximation to the simulation results in almost all cases. This is not surprising since linear theory does not take screening into account. The same can be said for HALOFIT, although it is still able to do much better than linear theory. Nevertheless, the HALOFIT predictions are still not good enough for precision cosmology; one can use detailed fitting formulas such as the one found in the MG-HALOFIT code for  $f(R)$  gravity, but even there the predictions can be off by as much as  $\sim 5\text{--}10\%$ . Unfortunately there is no universal fitting formula with this last approach and one needs to proceed on a model by model basis; this is clearly unfeasible if one wishes to explore extensive swathes of parameter space.

This work is a first step in laying down the tools for a thorough analysis of the effects of screening in weak lensing. To proceed, a number of steps can be envisioned. For a start, more efficient methods for generating the realisations of the density field must be developed (one approach has been advocated in [65]). Indeed, multiple realisations will be needed to pin down the fine details that will allow to distinguish between models, and an efficient scan of model parameter space is essential to be able to place reliable constraints on screening parameters themselves.

With such a tool in hand, there will be a need to develop robust analytical methods (in the spirit of a modified HALOFIT) which can be incorporated in a likelihood of up and coming data. In particular, with the tools developed here, it is now possible to calibrate the weak-lensing observables of the 3-D simulations with any analytical model which is chosen. An integral part of this step will be the extension of the pipeline to theories where there is non-trivial gravitational slip (unlike the cases considered here). This will involve modifying the lensing pipeline itself to include the modified integral of the gravitational potentials.

Finally, it will be possible to focus on specific structure and go beyond the basic statistics looked at here. As has been shown in [6, 58, 71], voids are a promising arena; gravity will be unscreened and one expects stronger signatures of modified gravity in such a setting [4, 13, 14, 36, 46].

## References

- [1] T. Baker, P. Ferreira and C. Skordis, *A fast route to modified gravitational growth*, *Phys. Rev. D* **89** (Jan. 2014) 024026, arXiv: [1310.1086](#).
- [2] M. Baldi, F. Villaescusa-Navarro, M. Viel, E. Puchwein, V. Springel and L. Moscardini, *Cosmic degeneracies - I. Joint N-body simulations of modified gravity and massive neutrinos*, *MNRAS* **440** (May 2014) 75, arXiv: [1311.2588](#).
- [3] A. Barreira, B. Li, W. A. Hellwing, C. M. Baugh and S. Pascoli, *Nonlinear structure formation in the cubic Galileon gravity model*, *J. Cosmology Astropart. Phys.* **10** (Oct. 2013) 27, arXiv: [1306.3219](#).
- [4] A. Barreira, M. Cautun, B. Li, C. M. Baugh and S. Pascoli, *Weak lensing by voids in modified lensing potentials*, *J. Cosmology Astropart. Phys.* **8** (Aug. 2015) 28, arXiv: [1505.05809](#).
- [5] E. Berti, E. Barausse, V. Cardoso, L. Gualtieri, P. Pani, U. Sperhake, L. C. Stein, N. Wex, K. Yagi, T. Baker, C. P. Burgess, F. S. Coelho, D. Doneva, A. De Felice, P. G. Ferreira, P. C. C. Freire, J. Healy, C. Herdeiro, M. Horbatsch, B. Kleihaus, A. Klein, K. Kokkotas, J. Kunz, P. Laguna, R. N. Lang, T. G. F. Li, T. Littenberg, A. Matas, S. Mirshekari, H. Okawa, E. Radu, R. O'Shaughnessy, B. S. Sathyaprakash, C. Van Den Broeck, H. A. Winther, H. Witek, M. Emad Aghili, J. Alsing, B. Bolen, L. Bombelli, S. Caudill, L. Chen, J. C. Degollado, R. Fujita, C. Gao, D. Gerosa, S. Kamali, H. O. Silva, J. G. Rosa, L. Sadeghian, M. Sampaio, H. Sotani and M. Zilhao, *Testing General Relativity with Present and Future Astrophysical Observations*, preprint (Jan. 2015), arXiv: [1501.07274](#).
- [6] K. Bolejko, C. Clarkson, R. Maartens, D. Bacon, N. Meures and E. Beynon, *Antilensing: The Bright Side of Voids*, *Phys. Rev. Lett.* **110** (Jan. 2013) 021302, arXiv: [1209.3142](#).
- [7] S. Bose, W. A. Hellwing and B. Li, *Testing the quasi-static approximation in  $f(R)$  gravity simulations*, *J. Cosmology Astropart. Phys.* **2** (Feb. 2015) 34, arXiv: [1411.6128](#).

- [8] P. Brax and P. Valageas, *Impact on the power spectrum of screening in modified gravity scenarios*, *Phys. Rev. D* **88** (July 2013) 023527, arXiv: [1305.5647](#).
- [9] P. Brax, A.-C. Davis, B. Li, H. A. Winther and G.-B. Zhao, *Systematic simulations of modified gravity: chameleon models*, *J. Cosmology Astropart. Phys.* **4** (Apr. 2013) 29, arXiv: [1303.0007](#).
- [10] P. Brax, A.-C. Davis, B. Li, H. A. Winther and G.-B. Zhao, *Systematic simulations of modified gravity: symmetron and dilaton models*, *J. Cosmology Astropart. Phys.* **10** (Oct. 2012) 2, arXiv: [1206.3568](#).
- [11] P. Brax, A.-C. Davis, B. Li and H. A. Winther, *Unified description of screened modified gravity*, *Phys. Rev. D* **86** (Aug. 2012) 044015, arXiv: [1203.4812](#).
- [12] P. Brax, C. van de Bruck, A.-C. Davis and D. J. Shaw,  *$f(R)$  gravity and chameleon theories*, *Phys. Rev. D* **78** (Nov. 2008) 104021, arXiv: [0806.3415](#).
- [13] Y.-C. Cai, N. Padilla and B. Li, *Testing Gravity using Void Profiles*, preprint (Oct. 2014), arXiv: [1410.8355](#).
- [14] Y.-C. Cai, N. Padilla and B. Li, *Testing gravity using cosmic voids*, *MNRAS* **451** (July 2015) 1036, arXiv: [1410.1510](#).
- [15] C. L. Carilli and S. Rawlings, *Motivation, key science projects, standards and assumptions*, *New A Rev.* **48** (Dec. 2004) 979, arXiv: [astro-ph/0409274](#).
- [16] T. Clifton, P. G. Ferreira, A. Padilla and C. Skordis, *Modified gravity and cosmology*, *Physics Reports* **513** (Mar. 2012) 1, arXiv: [1106.2476](#).
- [17] S. Colombi and D. Novikov, *POWMES: Measuring the Power Spectrum in an N-body Simulation*, Astrophysics Source Code Library, Oct. 2011, ascl: [1110.017](#).
- [18] A. Cooray, W. Hu and J. Miralda-Escudé, *Weak Lensing by Large-Scale Structure: A Dark Matter Halo Approach*, *ApJ* **535** (May 2000) L9, arXiv: [astro-ph/0003205](#).
- [19] A.-C. Davis, B. Li, D. F. Mota and H. A. Winther, *Structure Formation in the Symmetron Model*, *ApJ* **748** (Mar. 2012) 61, arXiv: [1108.3081](#).
- [20] S. Dodelson, *Modern cosmology*, Academic Press, 2003.
- [21] G. Dvali, G. Gabadadze and M. Porrati, *4D gravity on a brane in 5D Minkowski space*, *Physics Letters B* **485** (July 2000) 208, eprint: [hep-th/0005016](#).
- [22] B. Falck, K. Koyama, G.-b. Zhao and B. Li, *The Vainshtein mechanism in the cosmic web*, *J. Cosmology Astropart. Phys.* **7** (July 2014) 58, arXiv: [1404.2206](#).
- [23] C. Giocoli, R. B. Metcalf, M. Baldi, M. Meneghetti, L. Moscardini and M. Petkova, *Disentangling dark sector models using weak lensing statistics*, *MNRAS* **452** (Sept. 2015) 2757, arXiv: [1502.03442](#).

- [24] J. Harnois-Déraps, S. Vafaei and L. Van Waerbeke, *Gravitational lensing simulations - I. Covariance matrices and halo catalogues*, *MNRAS* **426** (Oct. 2012) 1262, arXiv: [1202.2332](#).
- [25] K. Hinterbichler and J. Khoury, *Screening Long-Range Forces through Local Symmetry Restoration*, *Phys. Rev. Lett.* **104** (June 2010) 231301, arXiv: [1001.4525](#).
- [26] A. Hojjati, L. Pogosian and G.-B. Zhao, *Testing gravity with CAMB and CosmoMC*, *J. Cosmology Astropart. Phys.* **8** (Aug. 2011) 5, arXiv: [1106.4543](#).
- [27] W. Hu and I. Sawicki, *Models of  $f(R)$  cosmic acceleration that evade solar system tests*, *Phys. Rev. D* **76** (Sept. 2007) 064004, arXiv: [0705.1158](#).
- [28] D. Huterer, *Weak lensing and dark energy*, *Phys. Rev. D* **65** (Mar. 2002) 063001, arXiv: [astro-ph/0106399](#).
- [29] Z. Ivezić et al., *LSST: from Science Drivers to Reference Design and Anticipated Data Products*, preprint (May 2008), arXiv: [0805.2366](#).
- [30] B. Jain, U. Seljak and S. White, *Ray-tracing Simulations of Weak Lensing by Large-Scale Structure*, *ApJ* **530** (Feb. 2000) 547, arXiv: [astro-ph/9901191](#).
- [31] J. Khoury, *Les Houches Lectures on Physics Beyond the Standard Model of Cosmology*, preprint (Dec. 2013), arXiv: [1312.2006](#).
- [32] J. Khoury and A. Weltman, *Chameleon cosmology*, *Phys. Rev. D* **69** (Feb. 2004) 044026, arXiv: [astro-ph/0309411](#).
- [33] M. Kilbinger, *Cosmology with cosmic shear observations: a review*, *Reports on Progress in Physics* **78** (July 2015) 086901, arXiv: [1411.0115](#).
- [34] A. Lewis, A. Challinor and A. Lasenby, *Efficient Computation of Cosmic Microwave Background Anisotropies in Closed Friedmann-Robertson-Walker Models*, *ApJ* **538** (Aug. 2000) 473, arXiv: [astro-ph/9911177](#).
- [35] B. Li, G.-B. Zhao and K. Koyama, *Exploring Vainshtein mechanism on adaptively refined meshes*, *J. Cosmology Astropart. Phys.* **5** (May 2013) 23, arXiv: [1303.0008](#).
- [36] B. Li, G.-B. Zhao and K. Koyama, *Haloes and voids in  $f(R)$  gravity*, *MNRAS* **421** (Apr. 2012) 3481, arXiv: [1111.2602](#).
- [37] B. Li, G.-B. Zhao, R. Teyssier and K. Koyama, *ECOSMOG: an Efficient COde for Simulating MODified Gravity*, *J. Cosmology Astropart. Phys.* **1** (Jan. 2012) 51, arXiv: [1110.1379](#).
- [38] C. Llinares and D. F. Mota, *Cosmological simulations of screened modified gravity out of the static approximation: Effects on matter distribution*, *Phys. Rev. D* **89** (Apr. 2014) 084023, arXiv: [1312.6016](#).
- [39] C. Llinares, D. F. Mota and H. A. Winther, *ISIS: a new  $N$ -body cosmological code with scalar fields based on RAMSES. Code presentation and application to the shapes of clusters*, *A&A* **562** (Feb. 2014) A78, arXiv: [1307.6748](#).

- [40] R. B. Metcalf and M. Petkova, *GLAMER - I. A code for gravitational lensing simulations with adaptive mesh refinement*, *MNRAS* **445** (Dec. 2014) 1942, arXiv: [1312.1128](#).
- [41] D. F. Mota and D. J. Shaw, *Evading equivalence principle violations, cosmological, and other experimental constraints in scalar field theories with a strong coupling to matter*, *Phys. Rev. D* **75** (Mar. 2007) 063501, eprint: [hep-ph/0608078](#).
- [42] A. Nicolis, R. Rattazzi and E. Trincherini, *Galileon as a local modification of gravity*, *Phys. Rev. D* **79** (Mar. 2009) 064036, arXiv: [0811.2197](#).
- [43] J. Noller, F. von Braun-Bates and P. G. Ferreira, *Relativistic scalar fields and the quasistatic approximation in theories of modified gravity*, *Phys. Rev. D* **89** (Jan. 2014) 023521, arXiv: [1310.3266](#).
- [44] K. A. Olive and M. Pospelov, *Environmental dependence of masses and coupling constants*, *Phys. Rev. D* **77** (Feb. 2008) 043524, arXiv: [0709.3825](#).
- [45] H. Oyaizu, M. Lima and W. Hu, *Nonlinear evolution of  $f(R)$  cosmologies. II. Power spectrum*, *Phys. Rev. D* **78** (Dec. 2008) 123524, arXiv: [0807.2462](#).
- [46] N. Padilla, D. Paz, M. Lares, L. Ceccarelli, D. Garcia Lambas, Y.-C. Cai and B. Li, *Void Dynamics*, preprint (Oct. 2014), arXiv: [1410.8186](#).
- [47] M. Petkova, R. B. Metcalf and C. Giocoli, *GLAMER - II. Multiple-plane gravitational lensing*, *MNRAS* **445** (Dec. 2014) 1954, arXiv: [1312.1536](#).
- [48] M. Pietroni, *Dark energy condensation*, *Phys. Rev. D* **72** (Aug. 2005) 043535, arXiv: [astro-ph/0505615](#).
- [49] E. Puchwein, M. Baldi and V. Springel, *Modified-Gravity-GADGET: a new code for cosmological hydrodynamical simulations of modified gravity models*, *MNRAS* **436** (Nov. 2013) 348, arXiv: [1305.2418](#).
- [50] M. Sato, T. Hamana, R. Takahashi, M. Takada, N. Yoshida, T. Matsubara and N. Sugiyama, *Simulations of Wide-Field Weak Lensing Surveys. I. Basic Statistics and Non-Gaussian Effects*, *ApJ* **701** (Aug. 2009) 945, arXiv: [0906.2237](#).
- [51] R. Scaramella, Y. Mellier, J. Amiaux, C. Burigana, C. S. Carvalho, J. C. Cuillandre, A. da Silva, J. Dinis, A. Derosa, E. Maiorano, P. Franzetti, B. Garilli, M. Maris, M. Meneghetti, I. Tereno, S. Wachter, L. Amendola, M. Cropper, V. Cardone, R. Massey, S. Niemi, H. Hoekstra, T. Kitching, L. Miller, T. Schrabback, E. Semboloni, A. Taylor, M. Viola, T. Maciaszek, A. Ealet, L. Guzzo, K. Jahnke, W. Percival, F. Pasian, M. Sauvage and the Euclid Collaboration, *Euclid space mission: a cosmological challenge for the next 15 years*, preprint (Jan. 2015), arXiv: [1501.04908](#).
- [52] F. Schmidt, *Dynamical masses in modified gravity*, *Phys. Rev. D* **81** (May 2010) 103002, arXiv: [1003.0409](#).

- [53] F. Schmidt, *Self-consistent cosmological simulations of DGP braneworld gravity*, [Phys. Rev. D](#) **80** (Aug. 2009) 043001, arXiv: [0905.0858](#).
- [54] F. Schmidt, *Weak lensing probes of modified gravity*, [Phys. Rev. D](#) **78** (Aug. 2008) 043002, arXiv: [0805.4812](#).
- [55] P. Schneider, C. S. Kochanek and J. Wambsganss, *Gravitational Lensing: Strong, Weak and Micro*, ed. by G. Meylan, P. Jetzer and P. North, Saas-Fee Advanced Courses 33, Springer, 2006, arXiv: [astro-ph/0407232](#).
- [56] R. E. Smith, J. A. Peacock, A. Jenkins, S. D. M. White, C. S. Frenk, F. R. Pearce, P. A. Thomas, G. Efstathiou and H. M. P. Couchman, *Stable clustering, the halo model and non-linear cosmological power spectra*, [MNRAS](#) **341** (June 2003) 1311, arXiv: [astro-ph/0207664](#).
- [57] D. Spergel, N. Gehrels, J. Breckinridge, M. Donahue, A. Dressler, B. S. Gaudi, T. Greene, O. Guyon, C. Hirata, J. Kalirai, N. J. Kasdin, W. Moos, S. Perlmutter, M. Postman, B. Rauscher, J. Rhodes, Y. Wang, D. Weinberg, J. Centrella, W. Traub, C. Baltay, J. Colbert, D. Bennett, A. Kiessling, B. Macintosh, J. Merten, M. Mortonson, M. Penny, E. Rozo, D. Savransky, K. Stapelfeldt, Y. Zu, C. Baker, E. Cheng, D. Content, J. Dooley, M. Foote, R. Goullioud, K. Grady, C. Jackson, J. Kruk, M. Levine, M. Melton, C. Peddie, J. Ruffa and S. Shaklan, *Wide-Field InfraRed Survey Telescope-Astrophysics Focused Telescope Assets WFIRST-AFTA Final Report*, preprint (May 2013), arXiv: [1305.5422](#).
- [58] P. M. Sutter, G. Lavaux, B. D. Wandelt, D. H. Weinberg, M. S. Warren and A. Pisani, *Voids in the SDSS DR9: observations, simulations, and the impact of the survey mask*, [MNRAS](#) **442** (Aug. 2014) 3127, arXiv: [1310.7155](#).
- [59] R. Takahashi, M. Sato, T. Nishimichi, A. Taruya and M. Oguri, *Revising the Halofit Model for the Nonlinear Matter Power Spectrum*, [ApJ](#) **761** (Dec. 2012) 152, arXiv: [1208.2701](#).
- [60] N. Tessore, H. A. Winther, R. B. Metcalf, P. G. Ferreira and C. Giocoli, *Weak lensing of large scale structure in the presence of screening*, [J. Cosmology Astropart. Phys.](#) **10** (Oct. 2015) 36, arXiv: [1508.04011](#).
- [61] R. Teyssier, *Cosmological hydrodynamics with adaptive mesh refinement. A new high resolution code called RAMSES*, [A&A](#) **385** (Apr. 2002) 337, arXiv: [astro-ph/0111367](#).
- [62] A. I. Vainshtein, *To the problem of nonvanishing gravitation mass*, [Physics Letters B](#) **39** (May 1972) 393.
- [63] M. White, *Baryons and weak lensing power spectra*, [Astroparticle Physics](#) **22** (Nov. 2004) 211, arXiv: [astro-ph/0405593](#).
- [64] C. M. Will, *The Confrontation between General Relativity and Experiment*, [Living Rev. Relativ.](#) **17** (June 2014) 4, arXiv: [1403.7377](#).

- [65] H. A. Winther and P. G. Ferreira, *Fast route to nonlinear clustering statistics in modified gravity theories*, *Phys. Rev. D* **91** (June 2015) 123507, arXiv: [1403.6492](#).
- [66] H. A. Winther and P. G. Ferreira, *Vainshtein mechanism beyond the quasi-static approximation*, *Phys. Rev. D* **92** (Sept. 2015) 064005, arXiv: [1505.03539](#).
- [67] H. A. Winther, D. F. Mota and B. Li, *Environment Dependence of Dark Matter Halos in Symmetron Modified Gravity*, *ApJ* **756** (Sept. 2012) 166, arXiv: [1110.6438](#).
- [68] H. A. Winther, F. Schmidt, A. Barreira, C. Arnold, S. Bose, C. Llinares, M. Baldi, B. Falck, W. A. Hellwing, K. Koyama, B. Li, D. F. Mota, E. Puchwein, R. Smith and G.-B. Zhao, *Modified Gravity N-body Code Comparison Project*, preprint (June 2015), arXiv: [1506.06384](#).
- [69] G.-B. Zhao, *Modeling the Nonlinear Clustering in Modified Gravity Models. I. A Fitting Formula for the Matter Power Spectrum of  $f(R)$  Gravity*, *ApJS* **211** (Apr. 2014) 23, arXiv: [1312.1291](#).
- [70] G.-B. Zhao, B. Li and K. Koyama, *Testing Gravity Using the Environmental Dependence of Dark Matter Halos*, *Phys. Rev. Lett.* **107** (Aug. 2011) 071303, arXiv: [1105.0922](#).
- [71] P. Zivick, P. M. Sutter, B. D. Wandelt, B. Li and T. Y. Lam, *Using cosmic voids to distinguish  $f(R)$  gravity in future galaxy surveys*, *MNRAS* **451** (Aug. 2015) 4215, arXiv: [1411.5694](#).